# Investigating Sand Transport and Landslides, and Implications for Past and Present Environments on Mars and Earth

Thesis by

Kevin Patrick Roback

In Partial Fulfillment of the Requirements for

the Degree of Doctor of Philosophy


CALIFORNIA INSTITUTE OF TECHNOLOGY

Pasadena, California

2021

Defended May 12, 2021

Kevin Patrick Roback

ORCID: 0000-0001-5209-2873

# Acknowledgements

This thesis would not have been completed without the support of many kind and generous people! My primary advisor, Jean-Philippe Avouac, has been a great mentor and friend to me over the past 5 years. His optimism and ability to see value and utility in my work that I sometimes struggled to see myself have had a great impact along with his accessibility and responsiveness. I have also appreciated the help of my other research advisor, Bethany Ehlmann, who always made time for the project on Martian landslides I brought to her despite her very busy schedule. And I thank my thesis committee members, Andy Ingersoll, Mike Lamb, and Simona Bordoni for the productive meetings and helpful input over the last several years.

But I wouldn't have gotten to the point of even considering this whole doctoral adventure if it weren't for the help of many people. Though I was interested in science from a young age, I had some good teachers at Walled Lake Western High School who helped to further that interest. I'm especially grateful to Scott Terry for being the primary organizer of our school's Science Olympiad club, to Michael Formanek for being a very good calculus teacher who wasn't afraid to challenge us, and to Ted McDonald for making a supportive community through the orchestra program.

I had a lot of great instructors at the University of Michigan as an undergrad; I am grateful to Profs. Aciego and Gleason for allowing me to take Intro Field Geology before my freshman year, and encouraging me to look for research opportunities in the department. I am also grateful to Scott R. Miller, now at the University of Utah, for providing my first real research opportunity as an undergrad.

I never would have wound up where I am, however, were it not for Marin Clark. She took me on to help map the landslides triggered by the Gorkha earthquake in Nepal, and allowed me to take leadership of the project when I put in the time and showed the interest. She also encouraged me to apply to Caltech, which is a place I almost certainly wouldn't have applied to without encouragement; I just didn't see myself getting into a program like this one.

At Caltech, aside from my advisors I've greatly appreciated the support provided by a number of people throughout the Institute. Francois Ayoub provided critical instruction to me on the methods of COSI-Corr and helped me get up to speed on our research group's methods when I arrived. Jay Dickson has helped me with numerous technical problems, and I've learned a lot about scripting and improved my geoprocessing toolkit thanks to him. Julie Lee, Lisa Christiansen, and the rest of the administrative staff in general, have been a great help to all of the GPS Division's grad students. Scott Dungan and Ken Ou have provided great and timely IT help, especially since the pandemic began. And Saif Aati has been a great help both with COSI-Corr and with assisting in the Avouac group's ongoing collaboration with the King Abdulaziz City for Science and Technology. I also must acknowledge everyone in both the Avouac and Ehlmann lab groups for listening and providing good feedback on my research when I've presented it at lab meetings, even though my work is rather deviant from the 'normal' stuff for both groups. And lastly, as I move towards the post-Caltech stage of my life, I've appreciated the help of the Career Center staff, especially James Berk, who has been a great help to me.

Most of all, though, I've been helped through this journey by my family and non-Caltech-affiliated friends. My parents and sister have always been supportive of my path even though it's quite different from what anyone in our family's done before. The support from my

sister’s husband, and their two dogs has been appreciated too! I've also been helped all through life by my very loving grandparents, including Grandma Betty, who saw me off to school every morning through my early high school years even though she didn't have to by that point, and Grandma Wanda who's just one of the most loving people I've ever known. As awful as the pandemic has been, it enabled me to spend a large portion of the past year reconnecting with family and enabled me to provide some help when it was greatly needed, and I'm thankful for that.

Lastly, I want to acknowledge the importance of numerous 'Internet friends' and acquaintances in my life. Especially over the past year, I've appreciated being a part of many great communities that provide entertainment and destressing that have helped me stay balanced through a difficult time and keep bringing my best effort to my work.

# Abstract

Wind-driven movement of sand and landslide activity are among the most important processes driving modern-day change on planetary surfaces. This thesis uses novel techniques and datasets to investigate the forces driving these processes on the surface of Mars, and also considers possible applications of the techniques described to Earth. Chapter 1 introduces past work done to understand these processes, and outstanding questions our work aims to answer. Chapter 2 presents and tests a new technique which aims to improve predictions of sand transport driven by wind on planetary surfaces by correcting coarse-resolution GCM predictions for the short-timescale fluctuations they miss. Chapter 3 presents new multiyear measurements of ripple migration at two dune fields on the surface of Mars, and applies these measurements, in conjunction with the new techniques described in Chapter 2, to investigate the dynamics of the Martian atmosphere, and test the accuracy of predictions made by Martian climate models. In Chapter 4, we study a large-scale natural sand trap in the Meroe Patera dune field on Mars, and estimate its trapped volume of sand in comparison to the volume of "missing" sand in a dune-free shadow zone downwind of the crater. The volume of trapped sand is far less than the missing volume, suggesting past escape of sand from the crater, despite a lack of obvious evidence for such escape in the present day. In Chapter 5, we change focus from sand transport to introduce an analysis of controls on the global distribution of Martian landslides. Chapter 6 discusses the limitations of applying the techniques of satellite image and climate model analysis described in Chapters 2-4 to terrestrial settings, as well as the possible utility of Chapter 5's method on other planets.

# Published Content and Contributions

Chapter 4 is published as: Roback, K. P. et al., 2020. Craters as sand traps: Dynamics, history and morphology of modern sand transport in an active Martian dune field. *Icarus*, *342*, doi:10.1016/j.icarus.2020.113642.

K. Roback and J.-P. Avouac conceived of the study; K. Roback and K. Runyon collected measurements, and K. Roback performed the analysis and wrote the manuscript with advising from coauthors.

Chapter 5 is published as: Roback, K. P. and Ehlmann, B. L., 2021. Controls on the Global Distribution of Martian Landslides. *Journal of Geophysical Research-Planets*, *126*(5), doi:10.1029/2020JE006675.

K. Roback conceived of the study, conducted the analysis, and wrote the manuscript with advising from B. Ehlmann.

**Table of Contents**

# 1. Thesis Introduction

## 1.1. Background on sand transport and dunes on Earth and Mars

In geology, sand grains are solid inorganic particles with a diameter between 62.5 and 2000 microns. Sand grains are small and light enough to be moved by winds on the surface of Earth, but they are too large to remain suspended in the atmosphere for long periods of time. Sand grains generally become organized into bedforms under the action of the wind, such as ripples and dunes.

Any discussion of past studies of sand transport must begin with the critical work of *Bagnold* (1941). Bagnold observed and measured the motion of sand grains in natural and wind-tunnel settings, identifying many principles that still hold up today. Bagnold recognized the existence of different modes of motion of sand grains. The primary mode, referred to as *saltation*, involves grains which are lifted from a sand bed, from either fluid drag forces or the impact of another grain, which then fly up into the fluid and are accelerated by it before falling back to the bed (Fig. 1.1). When saltating grains (saltons) fall back to the bed, they move other grains; some of these may become saltons themselves [e. g., *Andreotti,* 2004], but most will roll or hop short distances without being accelerated by the wind. These low-energy grains are referred to as reptons. Lastly, in high winds, some grains may fly large distances, accelerated upwards by turbulence, without ever contacting the bed; these grains would temporarily be in a state of suspension.

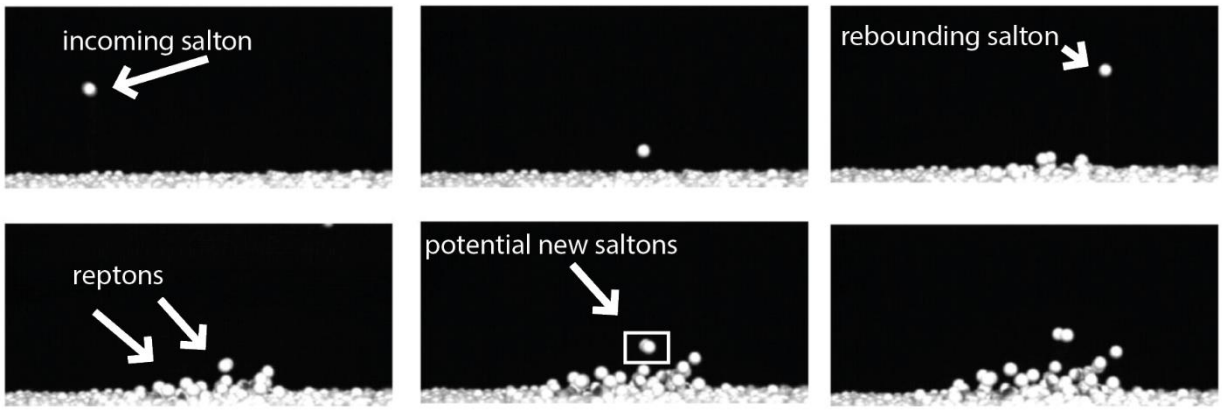


*Fig. 1.1*: Fig 2.5 from *Kok et al.,* 2012, annotated to highlight saltons and reptons.

In general, a wind that encounters a sand covered surface, if strong enough to initiate transport, will pick up grains over some length of the surface in the downwind direction, until the sand flux reaches a constant value referred to as the "saturated" sand flux, which is the maximum amount of sand that can be transported by that wind. Much effort [e. g., *Bagnold,* 1937; *Kawamura*, 1951; *Owen*, 1964; *Hsu,* 1971; *Lettau & Lettau*, 1978; *Werner*, 1990; *Sørensen*, 2004; *Duran et al.,* 2011] has been devoted to the development of predictive models for this sand flux. However, the length over which the sand flux reaches its saturated level (often called the "saturation length"; *Andreotti et al.*, 2010) is also important, as it is a fundamental control on the size of bedforms formed by sand. In particular, as a fluid flows over any bump in a sand bed, it is pushed upwards by the bump's presence; this causes an increase in the shear stress, reaching a maximum upwind of the top of the bump (Fig. 1.2). However, the sand flux does not increase instantaneously in response to this increased shear stress; it takes time for sand to be entrained by an oncoming wind.; There is thus a spatial lag, with the flux

reaching its maximum downwind of the shear stress maximum. If the bump is large enough such that this maximum flux occurs upwind of the highest elevation of the bump, the bump will grow as sand accumulates over the top of the bump. Over the part of the bump upwind of the maximum, erosion occurs because the flux is steadily increasing; while downwind of the maximum, the flux decreases and deposition occurs. This instability leads bumps in sand beds to grow towards being full-fledged dunes, and migrate downwind through time, provided they are larger than the saturation length; a bump smaller than this length will be eroded over its entire area and disappear.

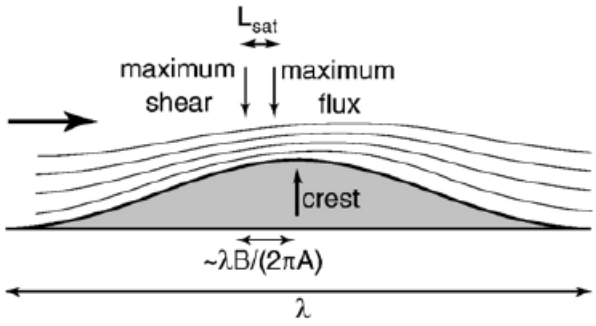


*Fig. 1.2*: Fig. 1 from *Claudin & Andreotti*, 2006, depicting the fluid flow and maxima in shear stress and sand flux over a sand bump.

Dunes vary greatly in size and form; dunes formed in water, such as those found in river beds, can have relatively short wavelengths on the order of 1 m; this is because water, being much denser than air, entrains grains quickly and provides relatively short saturation lengths for sand transport. In Earth's atmosphere, the saturation length forces dunes to be at least tens of meters long, and they can grow much larger. Ultimately, the sizes of dunes are limited by the height of the upper free surface

bounding the fluid in which they form. In flowing water, this surface is the water's surface; in an atmosphere, this is the height of the thermal inversion in the atmosphere [*Andreotti et al.,* 2009], where the atmosphere begins to warm (rather than cool) with increasing height. As dunes grow, the deflection of flow induced by their topography creates waves on this free surface, which perturb more flow down into eroding the downwind side of the dune, stopping further growth.

Dunes exhibit a wide variety of morphologies related to the direction and persistency of the flow in which they form (Fig. 1.3). This thesis will focus heavily on barchan dunes (Fig. 1.3A); these are dunes formed under largely-unidirectional winds when sand supply is limited. Due to the low sand supply, sand is organized into isolated dunes, which migrate in a consistent downwind direction. On the downwind-facing lee side of the dune, accumulating sand steepens the surface until the sand reaches its angle of repose and collapses, causing miniature sand avalanches. This surface tilted at the angle of repose is referred to as a slipface. Sand leaks from the dune around its sides; this continuous leakage of sand forms arms extending downwind from the dune's sides referred to as horns, which give barchan dunes a striking crescent shape.

If sand is more abundant but winds are still unidirectional, barchans will merge into forms referred to as transverse dunes (Fig. 1.3C). These dunes consist of ridges with undulating crests whose slipfaces indicate the dominant direction of transport, as they do for barchans. When winds blow primarily in two particular directions, straight-crested linear dunes form (Fig. 1.3B); the crest of these dunes typically follows the vector sum of the two component wind directions. And lastly, when the wind regime is

complicated and involves winds from many directions, sand may accumulate into large piles with arms extending outwards from their centers; these are called star dunes (Fig. 1.3D). Dunes of different wavelengths can also superimpose one another; some very large barchan-like dunes have developed superimposed transverse dune patterns (Fig. 1.3E). And on Earth, the influence of vegetation can lead to other dune forms, such as the vegetation-stabilized parabolic dunes in Fig. 1.3F.

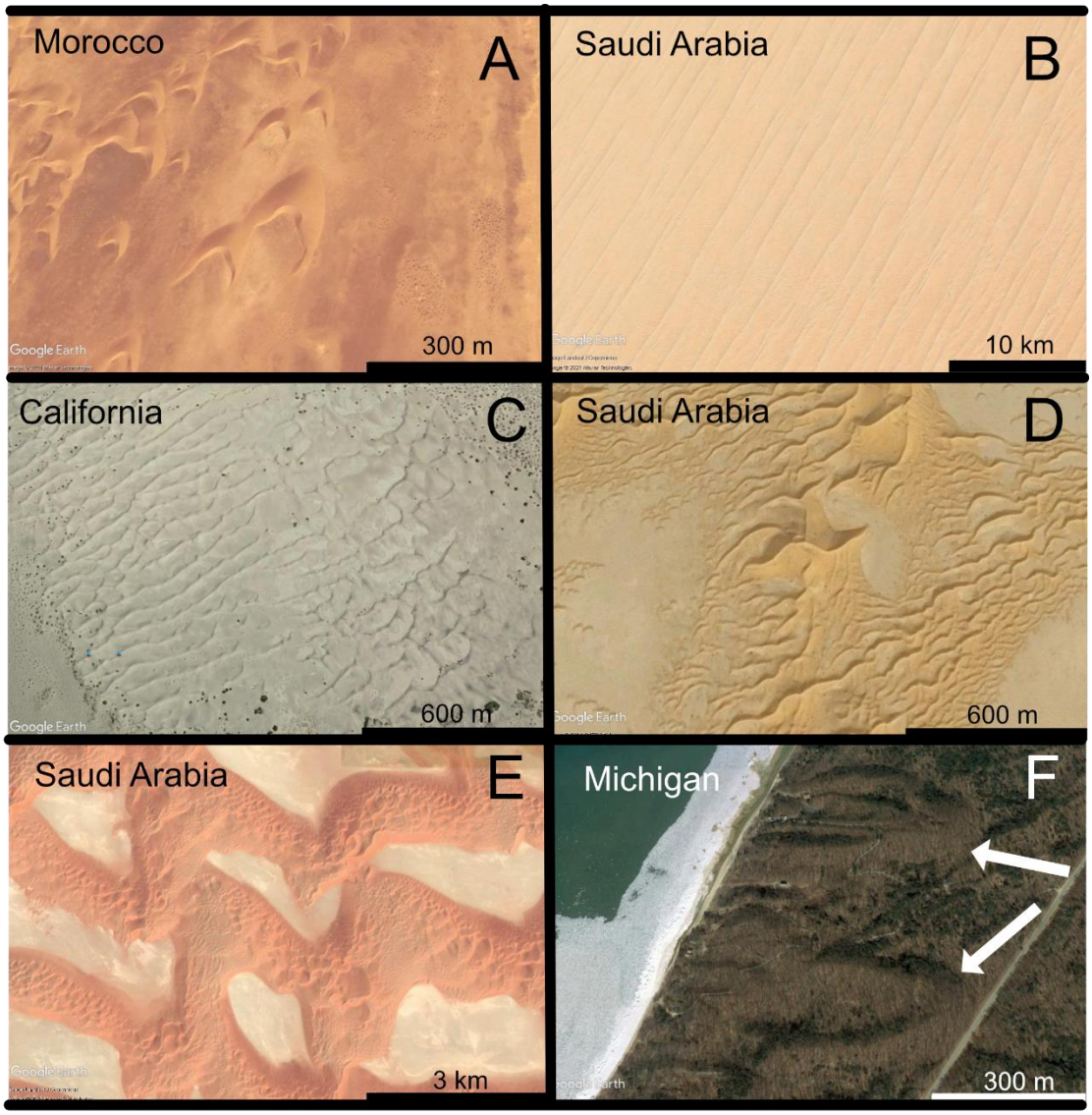

*Fig. 1.3*: A selection of major dune morphologies expressed on Earth; all images from Google Earth (Maxar Technologies). Panel A shows a barchan dune field, panel B shows a linear dune field, panel C shows a transverse dune field, panel D shows a star dune field , panel E shows a compound dune field with large barchan-like dunes overlaid by transverse dunes, and panel F shows a vegetation-covered, inactive pair of parabolic dunes (highlighted by arrows).

Active dunes are mantled by ripples; these are formed from the tiny 'craters' left by saltating sand grains when they collide obliquely with the sand bed's surface. Because the incoming saltons impact at an angle from the upwind direction, the upwind-facing sides of the depressions are more likely to receive another impact than the downwind sides; this encourages them to grow further, and also encourages sand grains to accumulate into the "shadow zones" partially shielded from impacts by the depressions. Over time, the depressions and ridges formed in this manner organize into fairly straight-crested small ripples due to these shielding effects caused by the local aspect of the surface; this model of their growth is called the "impact ripple" model [*Anderson*, 1987].

Martian dunes also have ripples, but intriguingly these can take much different forms than those seen on Earth. Small ripples resembling terrestrial impact ripples have been observed on Mars's dunes by rovers, but unlike Earth, these small ripples coexist with a much larger scale of ripples several meters in wavelength that pervasively mantle Mars's dunes. These large ripples have become a subject of major debate in the aeolian literature. Some authors [*Lapôtre et al.,* 2016; 2018] argue that large Martian ripples

form from wind-drag forces in a way distinct from the impact ripples seen on Earth's dunes, on the basis of their much larger sizes and often complicated, non-straight-crested morphologies which can include slipface formation. However, other authors [*Sullivan et al.*, 2020] argue that large Martian ripples are also impact ripples, which can grow far larger and develop more complicated morphologies than Earthly impact ripples thanks to the low density of Mars's atmosphere. On Earth, increases in wind stress at the crests of impact ripples occur due to the fact that the ripples protrude up into the oncoming flow. In Earth's thick atmosphere, these increases are large and may quickly stunt the growth of these ripples, limiting their size as proposed by *Bagnold*, 1937. However, on Mars the lower density atmosphere reduces the strength of this feedback and may thus enable larger ripple sizes. Recent wind tunnel studies [*Andreotti et al.*, 2021] have, however, found a lack of correlation between ripple size and atmospheric pressure, implying that a different mechanism may set the size of smaller ripples.

Bagnold's work included the development of expressions from which the "fluid threshold", abbreviated here as $u_{*ft}$, or shear stress needed to initiate sand motion from a standstill, and the "impact threshold" $u_{*it}$, the shear stress needed to maintain sand motion that is already occurring, can be calculated. The impact threshold is lower than the fluid threshold, since falling saltons provide an extra source of momentum, beyond that provided by the fluid itself, to eject more grains into the fluid flow which can in turn become saltons. Studies of $u_{*ft}$ were expanded upon by *Phillips* (1980), *Greeley & Iversen* (1985), and *Shao & Lu* (2000), who proposed revised expressions for the fluid threshold.

Calculating a precise fluid threshold for real-world conditions is complicated, due to the complexities of real-world grain size distributions, non-spherical geometries of grains, and on Earth, the presence of moisture and sometimes vegetation. It is even more complicated on other planets, as the effects of different gravity and atmospheric densities are difficult to test via experiment on Earth. Other parameters such as the grain size distribution may not be easily measurable on the surfaces of other planets either. Fluid thresholds can be written in units of stress, or units of velocity; in this thesis, fluid thresholds will generally be expressed as the latter. Shear stresses can be calculated from a wind-velocity measurement taken at a known height above the surface, and the surface roughness.

On Mars, $u_{*ft}$ is generally expected to be much higher than it is on Earth, due to the low density of Mars's atmosphere (0.02 kg/m$^3$ at the surface, versus 1.2 kg/m$^3$ for Earth). On Earth, commonly used models predict fluid threshold shear velocities of ~0.2-1 m/s depending on grain size [*Kok et. al.*, 2012]. On Mars, early wind-tunnel studies suggested fluid thresholds close to 2 m/s [*Iversen & White*, 1982; *Greeley & Iversen*, 1985]; wind speeds observed in situ on the Martian surface [e. g., *Sullivan et al.*, 2000; *Newman et al.*, 2017, *Banfield et al.*, 2020] do not approach these wind speeds. Because of this, for a time it was widely thought that sand transport should rarely happen on modern Mars [e. g., *Parteli & Herrmann*, 2007].

The arrival of the HiRISE camera [*McEwen et al.*, 2007] to orbit on Mars dramatically changed this view, however. HiRISE's 25cm/pixel imagery resolved the meter-scale large Martian ripples from space for the first time; over timespans of weeks, these ripples

could be observed to move [*Silvestro et al.*, 2010]. As HiRISE continued acquiring repeat images at Martian dune fields, the motion of entire dunes became clear as well [*Bridges et al.*, 2012]. The sand fluxes involved approached those at some Earthly cold-climate dune fields, challenging previous assumptions about the physics of Martian sand transport.

Various ideas have been proposed to reconcile the reality of widespread sand transport on Mars with the challenges posed by its thin atmosphere. The larger contrast between the fluid and impact thresholds on Mars may lead to hysteresis. In particular, with a fluid threshold that is high relative to Earth's fluid threshold (this means that sand transport is hard to initiate), but an impact threshold more comparable to Earth's impact threshold (this means that sand transport is not that hard to keep going once started), sand transport may persist for relatively longer once started on Mars than Earth. This would cause more sand transport than anticipated to happen on Mars [*Kok*, 2010a]. Alternatively, a more recent generation of wind-tunnel studies suggests that the fluid threshold may simply be much lower than previously thought for Martian conditions [*Musiolik et al.*, 2018; *Swann et al.*, 2020; *Andreotti et al.*, 2020]. Thus, both the dynamics of bedform formation on Mars and the basic parameters governing Martian sand transport are focuses of debate in the modern aeolian community.

Sand dunes are also of interest due to their potential to be used as checks on the wind predictions made by Martian climate models [*Hayward et al.*, 2009]. The forms and orientations of dunes reveal the directions of the dominant wind at a site, as described earlier in this section (p. 4); this can be compared against wind predictions

made by a climate model to determine whether climate models accurately reproduce the real wind pattern at a site. Additionally, changes in the rates of motion of sand dunes imply changes in the wind driving their motion, so these bedforms may be used to reveal atmospheric dynamics. However, sand dunes move slowly because of their large size, so we can only resolve their motion over long timescales (months to ~1 Martian year on Earth & Mars) even at relatively active sites. The smaller ripples present on dunes are thus ideal for tracking changes in the wind through time, but most ripples on Earth dunes are too small to be resolved in satellite images, limiting their utility. On Mars, however, the meter-scale ripples, which are both large enough to be resolved in satellite images from the HiRISE camera [*McEwen et al.*, 2007], and small enough to move quickly over shorter timescales [e. g., *Silvestro et al.,* 2010; *Bridges et al*., 2012] present an interesting opportunity to study the Martian atmosphere's dynamics; we will take advantage of this opportunity in Chapter 3.

Notably, tracking changes in the motion of bedforms measures a sand flux, known as the *translation flux*, that is not necessarily equal to the total flux at a site. In the case of smaller bedforms, such as ripples, many sand grains may simply fly over the bedform without being trapped by it. Also, dunes are not perfect traps of sand; barchan dunes leak sand through their horns, leading them to be unstable in isolation [e. g., *Hersen et al.*, 2004; *Worman et al.*, 2013]. This missing flux leads to changes in the shapes of bedforms, referred to as a *deformation flux* [*McElroy & Mohrig*, 2009]. The deformation flux is sometimes negligible relative to the translational flux, but has been estimated to include up to ~50% of the total sand flux in some field settings.

## 1.2 Background on landslides, and studies of them on Mars

Landslides are a common focus of geomorphologic studies on Earth, due to the hazards they represent for people, their impact on human infrastructure, and their massive influence on the evolution of landscapes in many mountainous regions. Landslides come in many different sizes and shapes, but most happen suddenly as material on a hillslope passes a critical threshold causing it to abruptly fail; however, some cases of slow-moving earthflows have been documented in Earthly soils.

In general, landslide initiation is governed by a balance of forces on a failure surface along which a landslide moves. This force balance consists primarily of the weight of material above the failure plane, which is a driving force balanced against frictional resistance along the failure plane. Extra forcing can be provided by groundwater, which fills pore spaces in rock; this both adds more weight above a failure plane and reduces frictional resistance provided by the normal stress along the failure plane itself, making landslide movement more likely; heavy rainfall is a common trigger of landslides on Earth. Additionally, shaking from seismic activity can provide an extra push to force motion along failure planes. On Mars, water and seismic shaking may have both contributed to landslide activity in the past, given the widespread evidence of past surface water on Mars, and the presence of many features on the planet's surface likely formed by faulting [*Knapmeyer et. al.*, 2006]. Though the spatial distribution and duration of this activity are unknown, the study of landslides could help to reveal more about it. A difference in landslide abundance between areas of equally unstable

topography would imply either a difference in the prevalence of these triggering factors, or a difference in the subsurface material strength.

The existence of large landslides on Mars's surface, some covering thousands of square kilometers, has been recognized since the Mariner 9 mission [*Lucchitta*, 1978]. These large landslides are heavily concentrated around Valles Marineris, a large system of canyons located near the Martian equator, cut into a large, relatively young volcanic province on Mars known as the Tharsis rise. The massive landslides have inspired a large number of past studies into their mobility [*McEwen*, 1987], their ages [*Quantin et al.*, 2004a], and their mechanisms of formation and motion. The landslides may have been wet [e. g., *Lucchitta,* 1987; *Quantin et al.*, 2004b] or dry [e. g., *McEwen*, 1987; *Lajeunesse et al.*, 2006; *Johnson & Campbell*, 2017]. Hydrated minerals [*Watkins et al.*, 2015; 2020] or ice [*De Blasio et al.*, 2011] may have played important roles in lubricating the bases of landslides in Valles Marineris. Seismicity may have also been an important trigger of landslides in Valles Marineris [*Schultz*, 2002; *Quantin et al.*, 2004a; *Kumar et al.*, 2019]. Age dating of large landslide deposits from crater counting [*Quantin et al.*, 2004a] suggests that landslides in Valles Marineris have happened steadily throughout the planet's history; some deposits are dated to >3 billion years old, while others are dated to as recent as <100 million years. Thus, whatever process(es) cause large landslides in Valles Marineris have likely continued to be present into the planet's recent history.

Recently, landslides on Mars have begun to be studied on a more global scale. *Crosta et al.* (2018a) present the first global mapped inventory of Martian landslides.

Landslides are found across much of Mars's surface; the highest concentrations are located in the vicinity of Valles Marineris, but landslides are found throughout the heavily cratered terrain of the Noachian Highlands as well. Interestingly, no large landslides are found at latitudes higher than 40 S and 46 N. *Crosta et al.* (2018a) suggest that this is due to modification of the surface by glacial processes at higher latitudes, which may have erased traces of past landslides. The much flatter topography at high latitudes (especially in the northern hemisphere) also contributes. *Crosta et al.* (2018b) present a further study of the mobility of Martian landslides; they find that landslides that appear to be associated with meteorite impacts, landslides around the Olympus Mons aureole and landslides with Toreva blocks are more mobile than others. (Toreva blocks are large blocks of material present within some landslide masses that remain largely intact as they rotate along a curved failure surface.) However, a fourth type of highly-mobile landslide includes relatively high-latitude landslides, and *Crosta et al.* (2018b) find that landslide mobility generally increases as a function of elevation. This suggests ice as a possible control on Martian landslide mobility, as efforts to map subsurface ice deposits have found that such ice is likely to be concentrated at higher latitudes [e. g., *Boynton et al.*, 2002], and ice that melts due to friction while a landslide is moving could plausibly lubricate it at its base.

The past studies of landslides on Mars have shown that, on exotic planetary surfaces where in-situ characterization of surface geology and processes is limited or not possible, landslide mapping can provide insight into the materials and active processes on other planetary surfaces. Concentrations of landslides in particular areas can hint at

processes or differences in surface-forming materials in those areas, but since landslides can be triggered via diverse means, interpretations of variations in their distribution are generally non-unique. Thus, landslides are best studied in context with other datasets; this idea will be explored further for Mars in Chapter 5.

# 2. Testing GCM Correction Techniques with Sand Transport and Meteorological Observations in Qatar

Kevin P. Roback[1], Jean-Philippe Avouac[1]

[1] – California Institute of Technology, Division of Geological and Planetary Sciences

*Abstract*

Global climate models (GCMs) provide essential insights into the climate and weather processes driving change on the surfaces of Earth and other planets. One of the many processes that might be predicted by GCM data is aeolian sand transport; however, our ability to predict sand transport from GCMs is hindered by the coarse-resolution view they provide, which neglects short-timescale, small-scale gustiness and turbulence in the wind regime. These gusts are likely to be important for the initiation of sand transport, particularly in thin atmospheres where high wind speeds are needed to initiate transport, such as that of Mars. We test a method to correct GCMs for this variability they miss, by setting each GCM prediction as the mean in an imposed probability distribution of wind predictions.

We compare simulated wind predictions and sand fluxes calculated from these wind predictions to observed sand fluxes and winds at a barchan dune field in Qatar. We find that the Weibull distribution best replicates observed sand fluxes and winds among the tested distributions, though it does somewhat exaggerate the incidence of higher winds. Distributions that are particularly inaccurate are those which maintain significant

probabilities for very high wind speeds beyond those present in observations. We also find that sand transport models, tested using the actual observed wind data from the Qatar site, tend to underpredict the sand fluxes. Our correction technique does improve sand flux predictions relative to uncorrected GCM data, but is limited by the outsized importance of rare, higher-wind events on sand flux prediction. Constraints on the highest winds, even from limited observational data or inference from nearby sites, would improve the accuracy of our technique.

## 2.1 Introduction

The construction and analysis of global climate models (GCMs) is essential to our understanding of the dynamics of planetary climates, and of many weather and climate-driven surface processes. These climate models have limitations, however, due to their coarse resolutions in space and time. At small scales, atmospheric winds are turbulent, exhibiting fluctuations not captured or predicted by planetary-scale climate models. These fluctuations can be impactful for many applications of GCM data.

One such application is the prediction of sand transport. Sand transport can be problematic in arid areas [e. g., *Al-Ghamdi & Hermas*, 2015; *Amin & Sedek Abu Seif*, 2019], due to the impacts of moving sand on human infrastructure. Understanding this activity is important to successful development in such areas. Additionally, in areas where future climate change leads to increased aridity, vegetation-stabilized dune fields may reactivate in some parts of the world [*Thomas et al*., 2005; *Ashkenazy et al*., 2012].

Human activities that deplete vegetation cover, like grazing and wood gathering, may also reactivate dune fields [*Yizhaq et al.*, 2009a] and lead to sand transport that must be managed.

Sand transport is also an important process on other planets. Modern Mars is a cold, dry desert world shaped largely by the action of wind. Sand dunes are prevalent across the planet's surface [*Cutts & Smith*, 1973; *Hayward et al.*, 2013], and they are active in the present day [e. g., *Silvestro et al.*, 2010; *Bridges et al.*, 2012; *Ayoub et al.*, 2014]. However, our ability to predict their activity is limited by disputes on the fundamental physics of Martian sand transport [e. g., *Greeley et al*., 1976; *Greeley et al.*, 1980; *Iversen & White*, 1982; *Swann et al.*, 2020]. Additionally, in-situ measurements of Martian winds are rare, due to the difficulty of landing a spacecraft to measure them on Mars's surface. This leads the sand transport predicted from Martian climate models to be relatively unconstrained. Though we might use sand dune activity driven by winds to test climate model predictions [*Hayward et al.*, 2009], our ability to do this is hindered by both our imperfect understanding of Martian sand transport, as well as the short-timescale fluctuations in wind that are missed by climate models.

To initiate sand transport, the wind stress on a sand-covered surface must exceed a certain threshold, known as the fluid threshold, required to move a small number of sand grains from a standstill. A second threshold, the impact threshold, is the threshold needed to maintain ongoing sand transport; this is generally lower than the fluid threshold, as transfer of momentum to the sand bed from particle impacts is more efficient than transfer via fluid-drag forces [*Kok et al.*, 2012].

In general, global climate models offer coarse resolution in space and time; on Earth, the ERA-Interim model is run on a timestep of 6 hours, while the spatial resolution of the model is 17 km. More recent ERA reanalyses, such as ERA5, still only offer a temporal resolution of 1 hour. On Mars, global scale MarsWRF simulations are run at 100 km spatial resolution and 1-hour timesteps; smaller-scale regional simulations are still run at 13 km spatial resolution and the same 1-hour timestep. These models are thus unable to directly simulate the turbulence that occurs on a planet's atmosphere from eddies which mix higher wind gusts from high elevations in the atmosphere down towards the surface on small spatial scales. This missing turbulence is problematic for sand transport predictions on Mars's surface; the fastest winds associated with this turbulence are not predicted by GCMs, meaning that the frequency at which the fluid threshold is exceeded will be underestimated, even if a GCM gets the mean wind right.

To help alleviate one of these limitations associated with sand transport prediction, we propose a new method to correct GCM predictions for the small-scale turbulence and gustiness they miss with the intention of using it to relate GCM model predictions and sand transport observations on Mars [Ch 3]. This method involves imposing a probability density function of variability, represented for example by a Weibull pdf, on the wind speed distribution. The mean wind speed of the Weibull distribution is set equal to the wind speed predicted by the GCM. We test alternative probability distributions to investigate their relative utility in GCM correction. This

method is presented here and tested at a terrestrial site where actual in-situ wind data is available, at a study site in Qatar.

## 2.2 Methods

### 2.2.1 Study Area and Prior field surveys

Our study area is a barchan dune field located in southeastern Qatar (Fig. 2.1). The region is predominantly affected by a wind blowing out of the NW, known as the Shamal; this wind is stronger in summer and winter [*Edgell*, 2006]. The regional topography of Qatar is flat, with a minor north-south anticline cresting towards the western end of the dune field at ~103 m above sea level. The overall setting of the region is thus quite simple. *Michel et al.* (2018) measured dune motion at 64 dunes in the northwestern portion of this dune field, in an area centered on ~25 N, 51.3 E, and used this to measure the sand flux associated with the dunes' migration, which may be referred to as the translation flux. The translation flux is a minimum estimate of the actual sand flux occurring at a dune, as it neglects sand that escapes from barchan dunes through their horns, as well as flux that may happen due to variability in wind that moves sand backwards relative to the dominant direction of motion.Two SPOT5 images taken ten years apart (Table 2.1), with a ground sampling distance of 2.5m, were used by *Michel et al.* (2018) to measure dune displacement.

| Satellite | Acquisition date | Time (UTC) | Spectral band | Resolution | Incidence angle |
|---|---|---|---|---|---|

| | | | | | |
|---|---|---|---|---|---|
| SPOT5 | 22 May 2003 | 07:23:11.9 | Panchromatic | 2.5 m | 0.8° |
| SPOT5 | 02 April 2013 | 07:11:53.4 | Panchromatic | 2.5 m | 23.3° |

*Table 2.1:* Images used by *Michel et al.* (2018) to measure dune displacements in Qatar; we use their derived sand flux values as references in this study.

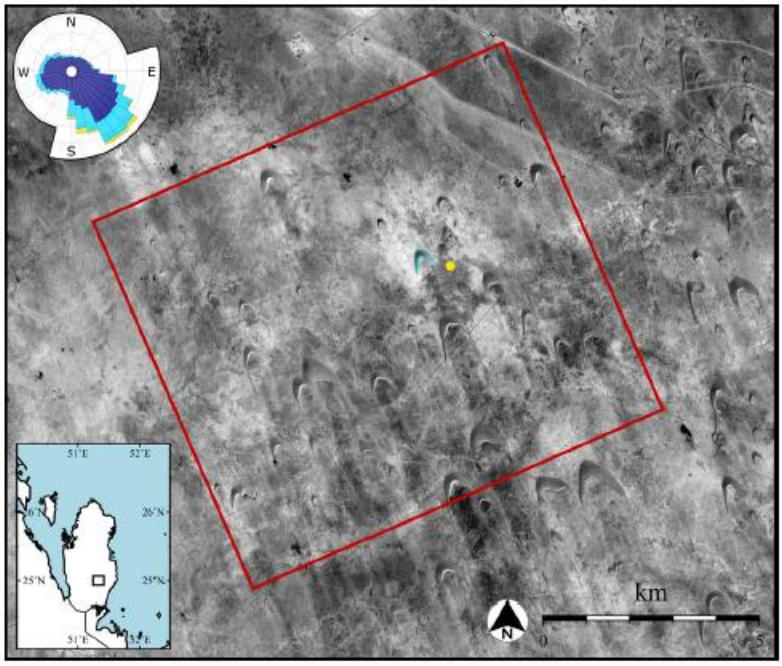


*Fig. 2.1*: Fig. 1 from *Michel et al.* (2018); their study area is shown by the red box, the dune they surveyed in the field is outlined in cyan, and the location of the meteorological station is marked by the yellow dot.

*Michel et al.* (2018) also performed field surveys of a dune located next to a weather station in this dune field. They flew a UAV (Unmanned Airborne Vehicle) over this dune to generate a 0.6m/pixel digital elevation model (DEM) of the dune, and interpolated the flat bedrock surface around the dune under it to generate an estimate

of the dune's volume; they also collected sand samples to determine the distribution of grain sizes in the dune's sand. The samples ranged from well sorted to very well sorted, with a mean grain diameter of 236 microns. The $D_{10}$ (grain size bigger than 10% of sand grains) was 157 microns, while the $D_{90}$ (grain size bigger than 90% of sand grains) was 318 microns. From this data, *Michel et al.* (2018) determined the sand flux at the surveyed dune, and more broadly across the dunes at the dune field by applying their field data in concert with width-volume scaling laws (*Hersen et al.*, 2004; *Durán et al.*, 2010). In particular, the dunes at the Qatar field were assumed to have similar, scale-independent shapes, under this assumption, the volumes $V$ of each dune may be calculated from its width $W$ observed in satellite images using a simple relation $V = K * W^3$. The value of the constant $K$ was determined from the geometry of the dune that was surveyed in detail via drone, and found to be 8.33 * $10^{-3}$. This average value of the flux found by *Michel et al.* (2018) was 24559 +/- 6895 kg/m/yr, given the uncertainty in dune displacement measurements, dune width measurements, and the volume measurement taken of the dune surveyed via drone. The *Michel et al.* flux estimate should additionally be regarded as a minimum estimate, as it is based on solely tracking changes in the position of bedforms, and does not attempt to track exchanges of sand between bedforms which would contribute an additional flux known as the *deformation flux.* This flux may be minor; repeat satellite images taken over ~20 years at the Qatar site show little change in shapes of dunes, but leakage of sand via the horns of barchan dunes is apparent, hinting that exchanges of sand between bedforms help to maintain the stable sizes of most dunes in this field. The magnitudes of this additional sand flux

cannot be constrained via satellite image analysis, and could be similar in magnitude to the translational flux, given past studies into the deformation flux [*McElroy & Mohrig*, 2009].

### 2.2.2 In-situ Meteorological Data, and GCM Data

*Michel et al.* (2018) obtained meteorological data (courtesy of Michel Louge) from a station which included anemometers at 0.94 and 2.54 m above the surface and a weather vane. The data was collected from November 17, 2011 to July 19, 2013. Measurements of the average wind speed were taken every minute, as well as the maximum wind speed in each 1-minute interval, and measurements of direction were taken every 10 minutes, and linearly interpolated by *Michel et al.* to 1-minute intervals between each measurement time. The measured wind speeds range from 0-16 m/s, and are dominated by the Shamal wind blowing NW-SE. We also obtain, as in *Michel et al.* (2018), predictions of weather conditions at the Qatar site from the ERA-Interim global climate model. The ERA-Interim model provides a sampling frequency of one sample every 6 hours; each of these samples is meant to be interpreted as an average over its corresponding time period. ERA-Interim provides wind predictions at a height of 10 m above the surface, and we take only ERA-Interim data from the grid cell located closest to the Qatar meteorological station; this grid cell is centered ~11 km to the station's south.

### 2.2.3 Methodology for GCM Correction

We set each wind prediction from ERA-Interim as the mean wind speed in an imposed probability distribution of wind speeds. The probability distributions we tested were the two-parameter Weibull and inverse Gaussian distributions, as well as the one-parameter Rayleigh distribution. These distributions were chosen as they have each been found to have utility in predicting wind speed distributions at some sites for wind-energy generation (*Carta et al.*, 2009). Additionally, since GCM predictions constrain the mean of a wind speed distribution but not its variance (due to the neglect of short-timescale turbulence), we focus on probability distributions in which one parameter can be constrained by either the mean wind speed alone, or a combination of the mean wind speed and unconstrained parameter. This way, we effectively have only one unconstrained parameter, for which different values can be tested.

The Weibull distribution has the density function

$$f(x|c,k) = \frac{k}{c}(\frac{x}{c})^{k-1}e^{-(\frac{x}{c})^k}.$$

Its parameters consist of a scale parameter *c* and a shape parameter *k*. *k* is not constrained by GCM predictions, so we test a range of values to investigate its impact. We estimate a range of reasonable values for our shape parameter by fitting a Weibull distribution to the observed wind data from Qatar, with averaged wind speeds below 0.5 m/s filtered out; the shape parameter in this best fit distribution is 1.79. Given this best fit value, we try a range of Weibull *k* parameters from 1.2 to 2.5 in our modeling. We filter out low wind speeds as they contribute no sand flux, and add a “spike” to the observed wind distribution (Fig. 2.2) which prevents it from fitting any of the commonly

used probability distributions. So, we filter these winds and fit the remainder of the distribution, and correct the average sand fluxes calculated given this missing null-flux period at the end of our calculations by multiplying our average predicted sand fluxes by 1 minus the fraction of time covered by these very low winds. We calculate the scale parameter *c* from *k* and the mean wind speed *m* predicted from ERA-Interim using

$$c = \frac{m}{\Gamma(1+\frac{1}{k})}$$ (*Carta et al.*, 2009),

where $\Gamma$ represents the gamma function. *Carta et al.* 2009 derived this equation, and all other equations used here to calculate probability distribution parameters, by setting the mean and variance of the probability distribution equal to that of an observed wind speed distribution, and solving for the two unknown parameters in a system of equations.

The inverse Gaussian distribution has the density function

$$f(x|c,k) = \sqrt{\frac{k}{2\pi x^3}} \exp\{-\frac{k}{2c^2 x}(x-c)^2\}.$$

It is also defined by two parameters, a scale parameter *c* and shape parameter *k*. For this distribution, we set *c* equal to the mean wind speed from the GCM, following the method of *Carta et al*. 2009. We then, as was done for the Weibull distribution, try a range of shape parameters *k* about a value provided by the best fit to the observed wind data. This shape parameter best fit to observations is about 6.9; we tried a range of shape parameters from 3 to 10 in our modeling.

Lastly, we also considered a one-parameter Rayleigh distribution. This has a density function of

$$f(x|a) = \frac{x}{a^2} e^{\left(\frac{x^2}{2a^2}\right)}.$$

We again tried a range of parameters for the Rayleigh shape parameter $a$. The best-fit shape parameter for our observed wind data had a value of 3.09; we tried values from 2.5 to 4.5.

From all probability distributions, we extracted 360 random values representing our simulated wind measurements under this imposed variability scheme (corresponding to simulated 1-minute increments, as each sample from ERA-Interim represents an average wind prediction over 6 hours). These simulated winds are both compared directly to the observed wind distribution in the Qatar dune field, and advanced forward into sand flux calculations.

### 2.2.4 Methodology for Sand Flux Calculation

We consider several of the different sand transport relations proposed in the literature. In all following equations, $\rho$ refers to the atmosphere's density (1.2 kg/m$^3$ at Earth's surface), $g$ is gravitational acceleration (9.81 m/s$^2$ for Earth's surface), $u_*$ is the shear velocity, $d$ is the median grain size (236 microns for the Qatar site, measured in the field by *Michel et al.* (2018)), and $D$ is a reference grain size (250 microns) defined by *Bagnold* (1937). Wind predictions from ERA-Interim are converted to shear velocities via application of the "law of the wall":

$$(1)\ u(z) = \frac{u_*}{\kappa}\ln\left(\frac{z}{z_0}\right).$$

Here, $z$ corresponds to a height of 10m for ERA-Interim predictions, and $\kappa$ refers to the Von Karman constant (0.4). $z_0$ is set equal to twice the median grain diameter [*Kok et al.*, 2012].

In this study, we consider results from the sand flux relations proposed by Bagnold (1937), Hsu (1971, 1973), Lettau & Lettau (1979), and White (1979):

$$(2)\ q = C_B\left(\frac{\rho}{g}\right)u_*^3\left(\frac{d}{D}\right)^{1/2}$$ [*Bagnold*, 1937]

$$(3)\ q = C_H\left(\frac{u_*}{(gD)^{1/2}}\right)^3$$ [*Hsu*, 1971; 1973]

$$(4)\ q = C_L\left(\frac{d}{D}\right)^{1/2}\left(\frac{\rho}{g}\right)u_*^2(u_* - u_{*t})$$ [*Lettau & Lettau*, 1979]

$$(5)\ q = C_W\frac{\rho}{g}(u_*^2 - u_{*t}^2)(u_* + u_{*t})$$ [*White*, 1979]

Additionally, for Hsu's relation:

$$(6)\ \ln(C_H * 10^4) = -0.47 + 4.97d$$ [*Hsu,* 1971]

In the above equations, $C_B$ = 1.8 [*Bagnold*, 1941], $C_L$ = 6.7, and $C_W$ = 2.61. Note that all relations only apply to the condition where $u_* > u_{*t}$; otherwise, $q = 0$.

We additionally consider how a sand flux relation proposed by *Kok* (2010b) for Martian conditions compares to our observed sand fluxes in an Earthly site, and to predictions made by alternative sand flux laws. This model computes a revised probability of sand transport, accounting for the hysteresis associated with settings in which the contrast between the impact and fluid thresholds is particularly large, as is

the case on the surface of Mars. This model also assumes that the input winds follow a Weibull distribution. It can be adjusted for Earth conditions as the model parameters that need to be adjusted (atmospheric density and gravity) are explicit. The expression used to compute the probability of transport in the *Kok* (2010b) model is:

$$(7)\ P_{tr} = \exp\left\{-\left[\frac{u_{*ft}\Gamma\left(1+\frac{1}{k}\right)}{\bar{u}^*}\right]^k\right\} + \exp\left\{-\left[\frac{u_{*ft}\Gamma\left(1+\frac{1}{k}\right)}{\bar{u}^*}\right]^k\right\} \times \ldots$$

$$\ldots \frac{\exp\left\{-\left[\frac{u_{*it}\Gamma\left(1+\frac{1}{k}\right)}{\bar{u}^*}\right]^k\right\} - \exp\left\{-\left[\frac{u_{*ft}\Gamma\left(1+\frac{1}{k}\right)}{\bar{u}^*}\right]^k\right\}}{1-\exp\left\{-\left[\frac{u_{*it}\Gamma\left(1+\frac{1}{k}\right)}{\bar{u}^*}\right]^k\right\} + \exp\left\{-\left[\frac{u_{*ft}\Gamma\left(1+\frac{1}{k}\right)}{\bar{u}^*}\right]^k\right\}}$$ (*Kok*, 2010a).

In this expression, $u_{*ft}$ represents the fluid threshold for sand motion (equivalent to $u_{*t}$ in the previous sand transport models), and $u_{*it}$ represents the impact threshold, which is the minimum shear velocity needed to maintain ongoing sand transport. The impact threshold was to be ~0.19 m/s based on modeling and experimental work on the impact threshold presented in *Kok* (2010b). *k* represents the Weibull shape parameter and $\bar{u}^*$ represents the mean wind speed, taken in our modeling as the wind speed predicted by ERA-Interim. *Kok* (2010b) integrates this $P_{tr}$ into the *White* (1979) mass-flux relation:

$$(8)\ q = P_{tr} C_W \frac{\rho}{g}(u_* - u_{*it})(u_* + u_{*it})^2.$$

Notably, our wind speed distributions that are input to our sand flux models only fit the non-null portion of the observed wind regime; as mentioned in the preceding section, a large number of our directly measured wind speeds fall at low wind speeds close to zero (Fig. 2.2). These wind measurements comprise 31% of the total number of

wind measurements, and given their low wind speeds, we assume that sand flux during these periods is negligible. We therefore correct our sand fluxes, which represent the average flux over the 69% of observed winds that are fit to our distributions, by multiplying them by 0.69.

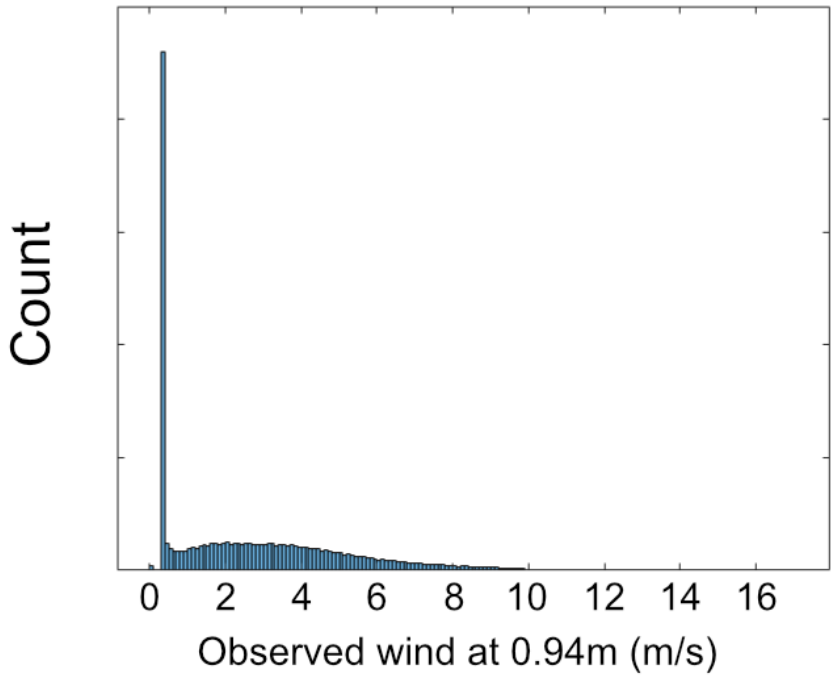


*Fig. 2.2*: Observed distribution of wind speeds, taken at 0.94m height, from the Qatar weather station located in our study area. Data was collected at 10-minute intervals, and extrapolated by *Michel et al.* (2018) to provide a value every minute.

## 2.3 Results

Comparisons of predicted and observed wind distributions from the tested probability distributions are provided in Fig. 2.3 and Table 2.2. For each distribution type shown, the probability distribution is that which represents the best fit to the observed

wind data. In general, the "tail" of higher-velocity wind measurements is slightly overrepresented for the Weibull distribution; the fluid threshold is exceeded 6.87% of the time in the Weibull best-fit pdf, but only 5.69% of the time in the observed wind distribution. Additionally, the highest predicted shear velocities are ~2 m/s, in contrast to the observed maximum of ~0.6 m/s. This problem is worsened for the inverse Gaussian distribution; here 6.93% of wind measurements exceed the fluid threshold, and the range of very high winds is much greater; shear velocities as high as 7 m/s (26 times higher than the fluid threshold) are predicted in the distribution. This effect happens due to the structure of the inverse Gaussian distribution's function; it maintains non-negligible probabilities into much higher wind speeds than the Weibull distribution. Meanwhile, for the Rayleigh distribution higher winds are underpredicted rather than overpredicted; the fluid threshold is exceeded only 1.31% of the time, versus 5.69% in observed data. Additionally, the highest shear velocities extracted from the Rayleigh pdf are only ~0.5 m/s, less than the ~0.6 m/s max in the observed wind distributions.

| Winds | Observed | GCM | Weibull-corrected | Inverse Gaussian-corrected | Rayleigh-corrected |
|---|---|---|---|---|---|
| % of time fluid | 5.69 | 3 | 6.87 | | 1.31 |

| | | | | | |
|---|---|---|---|---|---|
| threshold exceeded | | | | | |
| Max wind (m/s) | 14.9 | 13.9 | 44.8 | 154 | 11 |

*Table 2.2:* A comparison of parameters relevant to sand transport from observed, model-predicted, and probability distribution-corrected wind distributions for the Qatar study site. In particular, we compare the overall prevalence of 'high' winds by comparing the percentage of time that the fluid threshold is exceeded in each distribution, as well as the highest winds predicted from each distribution. For probability distribution-corrected winds, a number of simulated observations equal to the number of observations made over the 2-year timeseries of wind data provided at the Qatar site by Michel Louge is extracted from our probability distributions.

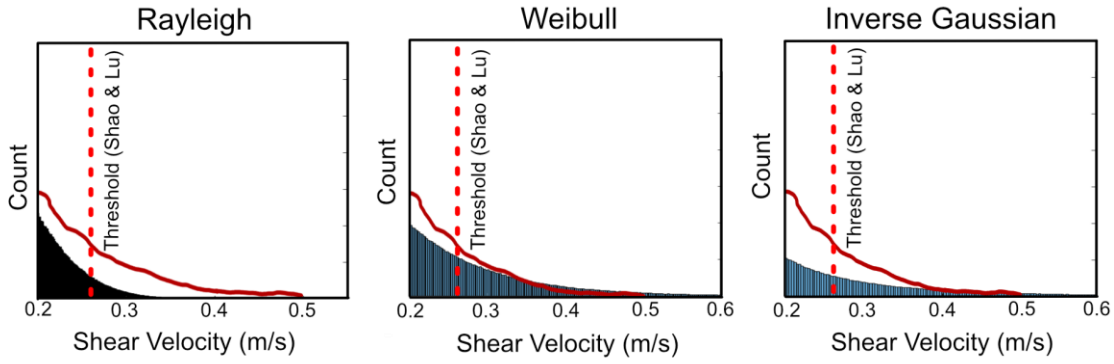


*Fig. 2.3*: The high-velocity portions of wind probability distributions for observed wind data (red line), and the best-fit distribution from 3 unique types of probability distributions. Note that all graphs are truncated at shear velocities of 0.6 m/s, but for

the inverse Gaussian and Weibull distributions, there are extracted shear velocities much higher than 0.6 m/s, though they are relatively infrequent. In particular, the highest shear velocities extracted from the Weibull probability distribution are ~1.8 m/s, while the highest shear velocities extracted from the inverse Gaussian are ~7 m/s.

Sand fluxes calculated from winds corrected using different probability distributions are presented in Fig. 4. In all cases, the sand flux is presented as a function of the shape parameter for the relevant probability distribution, with the best-fit shape parameter to the observed wind data marked; the sand flux calculated for this best-fit distribution of each type is included in Table 2. The predicted sand fluxes from ERA-Interim winds corrected using the Weibull distribution for the tested sand transport models fit the observed sand fluxes from *Michel et al.* (2018) well around the area of the best-fit Weibull variability parameter. However, the inverse Gaussian distribution produces sand fluxes that are too high regardless of the choice of transport model, and the Rayleigh distribution produces sand fluxes that are always too low.

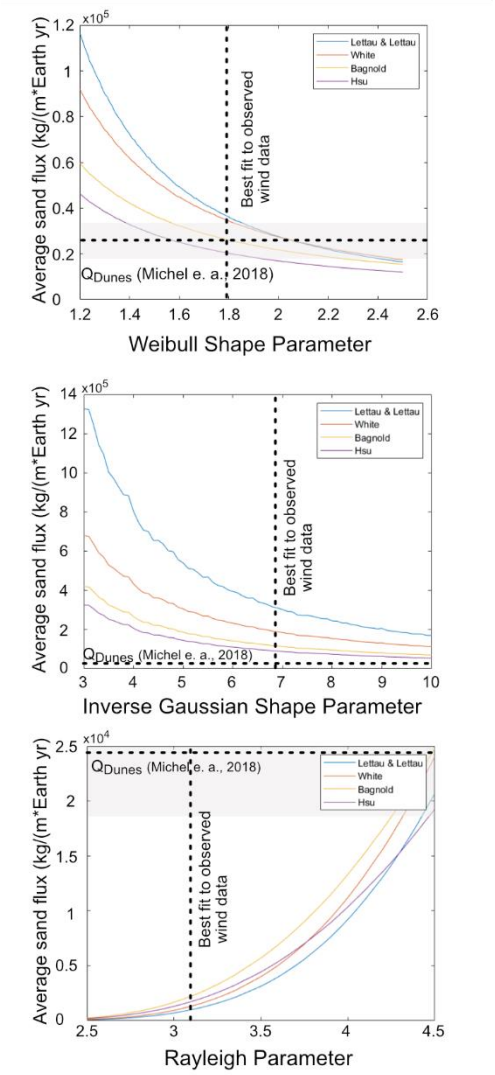


*Fig. 2.4*: Predicted sand fluxes, as a function of probability distribution shape parameter, for the Weibull, inverse Gaussian, and Rayleigh probability distributions. In each graph, the shape parameter that best fits observed wind data is shown by the vertical dashed line. $Q_{Dunes}$, the sand flux measured at the dune field by *Michel et al.* 2018, is indicated by the dashed line and shaded uncertainty.

We also tested our models by investigating the sand fluxes they predicted from both the observed wind data from the meteorological station, and from the ERA-Interim

climate model. The results of these are shown in Table 2.2. In general, from the actual meteorological data, our sand transport models underpredict the flux at the Qatar study site by ~50% relative to the observed 24559 +/- 6895 kg/m*yr flux. The degree of underprediction was greater when only the unaltered 6-hour ERA-Interim predictions were used. Meanwhile, the *Kok* (2010a) sand transport model developed for Mars, which assumes a Weibull variability in the wind, predicts similar results to the other models for Earth conditions; its output flux of 36,200 kg/m*yr is very similar to the predicted flux from the *Lettau & Lettau* (1978) model, and broadly in line with the other models under Weibull variability.

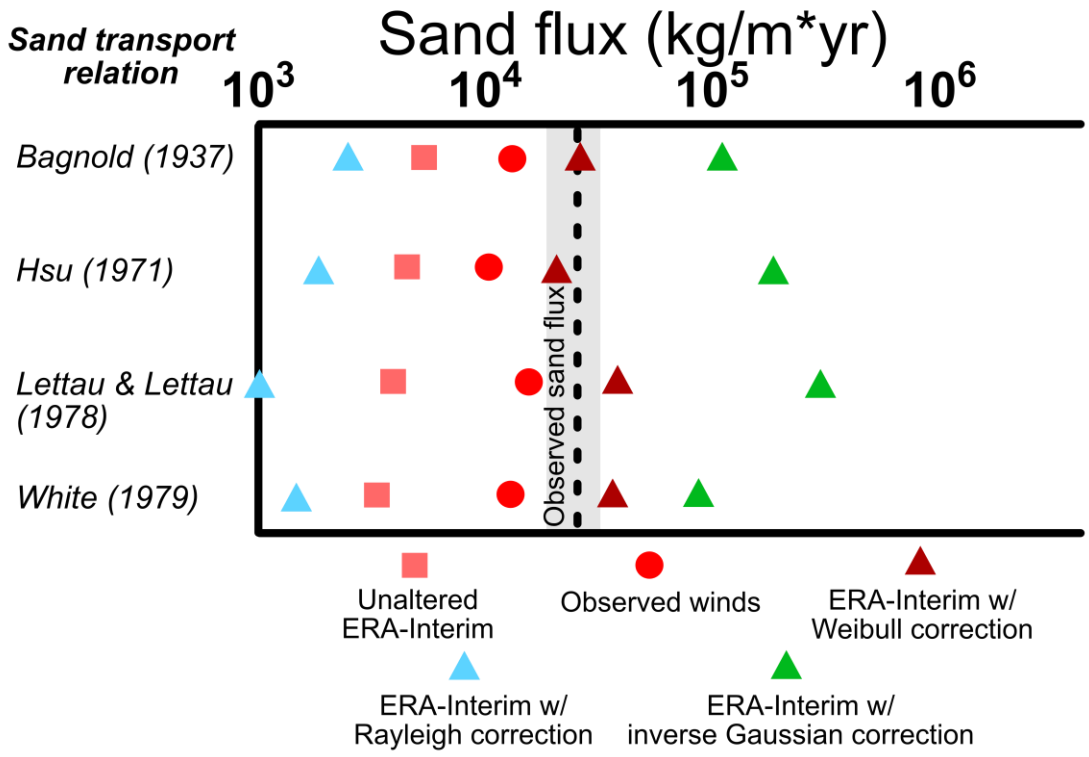


*Fig. 2.5:* Sand fluxes predicted from observed winds, model-predicted winds, and model-predicted winds altered using various probability density function correction schemes.

All fluxes presented in this table are in units of kg/m*yr. The actual flux measured from field studies and dune migration measurements is 24559 +/- 6895 kg/m*yr.

## 2.4 Discussion

A simple comparison of our modeled sand fluxes under each probability distribution suggests that the Weibull distribution is most accurately reproducing the observed wind regime at our Qatar study site. Though it is certainly more accurate than the Rayleigh or inverse Gaussian distributions, which miss the observed fluxes by about an order of magnitude in different directions, the Weibull distribution is still overrepresenting high winds at the Qatar site, as revealed by the fact that the frequency of fluid threshold exceedance and highest overall winds are higher than observations. The good match between Weibull-predicted and observed sand fluxes is thus a case of "two wrongs making a right."

The underprediction of flux by sand transport models is interesting, as many previous studies [e. g., *Sherman et al*., 2013] have found that sand transport models often overpredict, rather than underpredict actual sand fluxes. There are some obvious differences between this study and that of *Sherman et al.* (2013) however. Firstly, our wind data is only measured in 1-minute averages; at this timescale, a significant amount of gustiness and variability in the observed wind regime is likely being missed, including some higher-velocity wind gusts; these missing gusts may contribute significantly to the actual sand flux. Our wind dataset includes maximum wind speed measurements

recorded over each 1-minute increment; these are an average of ~35% higher than the mean wind speed measurements over 1-minute intervals.

We can test the impact of this variability by imposing a wind probability distribution to model the sub-minute-scale variability as we have done for the longer-timescale variability. Our only constraints from observations are a mean wind speed, and a stipulation that the fastest wind gust extracted at 1 Hz over a 1-minute interval not be >35% higher than the mean. We set a normal probability distribution's parameters to model the wind speed under these constraints; for a mean assumed wind speed of 8.75 m/s, corresponding to the wind speed at the shear threshold estimated for the Qatar site conditions, a standard deviation of 1.1 m/s produces a distribution with <1% probabilities of observing winds that deviate by >35% from the average. We use a normal distribution as, on sub-minute timescales, the maximum wind in a 1-minute timescale is relatively closer to the mean than in the hour-plus timescales of a GCM's timesteps. The Weibull scheme, with an asymmetric tail of particularly high wind speeds is thus a poorer fit to the natural distribution in this case.

The relatively lower variability on sub-minute timescales is also indicated by studies into the "power spectrum" of observed wind data. The power spectrum of a wind dataset describes the relative magnitude of variations in the wind on different timescales. Construction of these power spectra for observed wind data have found a double-peaked structure in the power spectrum, with peaks at ~1 minute and ~4 day timescales [*Van der Hoven*, 1957]. The 4-day fluctuations reflect the passage and evolution of large scale weather systems, while the 1-minute peak is from fluctuations

caused by small-scale turbulence. The dropoff in intensity of observed power spectrums below 1 minute suggests that at most sites, fluctuations of wind below this timescale are unlikely to be very large in magnitude, mitigating the error in our sand flux predictions.

However, when the mean wind speed is very near to the fluid threshold, the imposition of this extra variability can greatly alter sand flux predictions nonetheless. In particular, under the Bagnold (1937) and Hsu (1971) sand transport relations mean flux increases by ~50% under the aforementioned sub-minute normally distributed variability scheme. It increases by proportionally more for the Lettau & Lettau (1978) and White (1979) relations, as these predict near-zero fluxes when the wind speed is barely above the fluid threshold. This effect diminishes rapidly, however, as we increase the mean wind beyond the shear threshold. For mean wind speeds of 10.5 m/s, 20% above the fluid threshold, under the Bagnold (1937) and Hsu (1971) transport relations the sand fluxes differ by <1%. For the Lettau & Lettau (1979) relation, the imposed variability increases fluxes by 17%, and for the White (1979) relation, the fluxes increase by 9%.

Thus, the overall impact of this further correction on our sand transport measurements depends on the 1-minute-averaged winds observed at our study site. If more wind measurements are very close to the fluid threshold, the fluid threshold is exceeded more frequently than it is without this assumed sub-minute variability. Sand flux laws that predict the flux to diminish to 0 at the fluid threshold are particularly affected in this case, as the periods of stronger winds greatly increase the sand flux

relative to the minuscule mean when the flux is barely above the threshold.However, at wind speeds significantly above the threshold, the periods of decreased winds partially cancel the impact of the periods of higher winds, causing minimal change in overall predicted sand fluxes. Additionally, when winds are well below the fluid threshold, this imposed variability causes no new exceedance of the fluid threshold, so there is no effect on sand fluxes.

The presence of water often affects sand transport predictions, though it is unlikely to be important at the Qatar study site. Firstly, water leads to increases in interparticle forces, which tends to increase the fluid threshold and decrease sand transport – its neglect thus leads sand transport to often be overpredicted, rather than underpredicted in natural settings. Secondly, there is likely to be relatively little water in the sands at the Qatar study site given Qatar's arid, hot desert environment.

The topography of the dune itself may be a more important factor. High-resolution measurements of sand flux on Martian sand dunes can be acquired thanks to their meter-scale ripples whose motion can be tracked from space [e. g., *Silvestro et al.*, 2010; *Bridges et al*., 2012; *Ayoub et al*., 2014, Chapter 3]. These measurements reveal that ripples on Martian dunes consistently speed up near their crests; this effect is predicted by fluid dynamical models of airflow over sand dunes [*Jackson et al.*, 2015; *Smith et al*., 2017], and is not accounted for in sand transport models which usually assume a flat sand bed; this could lead to additional underestimation of the sand flux. Future work relating whole-dune measured sand fluxes to in situ meteorological data may better constrain the dune topography's impact on sand fluxes.

A major hindrance to the accuracy of the use of Weibull distributions, and other probability distributions, to correct GCM predictions is the nonzero probability of very high wind speeds, beyond those that are actually observed, in many probability distributions. Though infrequent, these winds have an outsized impact on the predicted sand flux since flux models predict higher fluxes under higher winds. If these maximum winds can be constrained, we can significantly increase the accuracy of the Weibull and other distributions that we might use to correct climate models.

Though GCMs do not explicitly simulate short timescale turbulence and gustiness, the intensity of turbulence and gustiness may be related to the mean wind speed; in particular, measurements at offshore platforms [*Türk & Emeis*, 2010] have found that the turbulence intensity correlates with the strength of the mean wind measured at 90m above the surface; however, this forcing is thought to happen due in part to the increasing surface roughness of the ocean at high wind speeds, caused by increasing wave heights in higher wind speeds; it has not been verified for land settings. The turbulence intensity may also be related to the rate of increase in the wind speed with height in the atmospheric boundary layer; a greater rate of increase will lead to relatively stronger wind gusts which may mix down to the surface through the action of turbulent eddies. However, more work remains to be done in the prediction of turbulence intensity. In this area, in situ measurements will always be indispensable for optimal prediction of sand fluxes.

An improvement to our Weibull correction scheme can be made if the maximum wind observed at a site can be determined or estimated. For the Qatar site, if we cut off the

Weibull distributions we generate to eliminate all winds greater than the maximum observed wind of 15 m/s, the degree of overprediction of the sand flux, relative to that calculated from the observed wind distribution, is greatly reduced (*Fig. 2.6*). Calculating this maximum wind without observed in situ data may be challenging, however.

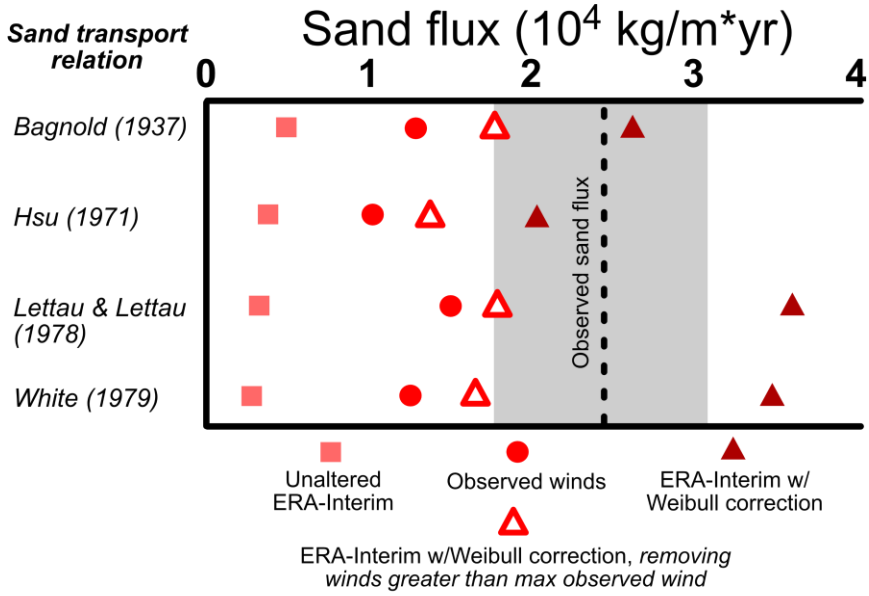


*Fig. 2.6:* Comparison of sand fluxes predicted from GCM-predicted and observed winds (squares and circles, respectively), with Weibull-corrected GCM winds in which all simulated wind speeds predicted from the Weibull function are included (dark, filled triangles), and Weibull-corrected GCM winds in which simulated wind speeds greater than the observed maximum wind of 15 m/s are excluded from the calculation (light, open triangles).

Despite its limitations, the Weibull correction scheme does nonetheless reproduce observed winds more accurately than GCM predictions alone (Fig. 2.3), and also outcompetes other tested probability distributions. GCM-predicted winds exceed

the fluid threshold at the Qatar site only 3% of the time; this is further off from the real observed winds (5.69% exceedance) than the Weibull correction (6.87% exceedance).

## 2.5 Conclusions

We test a novel method to correct wind predictions made by the ERA-Interim climate model, using sand transport measurements and in situ wind data collected at a dune field in Qatar. We find that the Weibull distribution reproduces observed sand fluxes more closely than other usable distributions, as it reproduces the high-velocity tail of observed winds more accurately than an uncorrected GCM prediction, or other probability distributions such as the inverse Gaussian or Rayleigh. However, the Weibull distribution nonetheless exaggerates the occurrence of high-velocity winds in our distribution relative to observations. Sand transport models underpredict the observed fluxes at our Qatar site, though they may be thrown off by the 1-minute resolution of our in-situ wind data and the lack of accounting of dune topography in the sand flux calculation. We conclude that assuming a Weibull distribution is probably the best approach to allow comparison of observations of the sand flux made from remote sensing with predictions based on GCMs whether on Earth or Mars. The accuracy of our technique can be improved if the maximum wind at a site can be constrained.

# 3. Multi-year Measurements of Ripple and Dune Migration on Mars: Implications for the Wind Regime and Sand Transport

Kevin P. Roback[1], Kirby Runyon[2], Claire Newman[3], Jean-Philippe Avouac[1],

[1] – California Institute of Technology, Division of Geological and Planetary Sciences, Pasadena, CA, USA

[2] – The Johns Hopkins University Applied Physics Laboratory, Laurel, MD, USA

[3] – Aeolis Research, Tucson, AZ, USA

**Abstract**

Aeolian sand dunes are observed across the Martian surface. The arrival of the HiRISE camera on Mars Reconnaissance Orbiter at Mars in 2006 enabled detection of modern-day movement of dunes and ripples from orbit for the first time. Since 2006, HiRISE collected a long timeseries of repeat imagery at a few Martian dune fields. We analyze this timeseries of imagery at two of these dune fields, using COSI-Corr for image registration and correlation, to study the movement and dynamics of dunes and meter-scale ripples at the Nili Patera and Meroe Patera barchan dune fields. We present measurements of whole-dune translational sand fluxes extracted at both dune fields via manual tracking of dune crestlines and slipfaces in HiRISE images. We also present a multi-Mars year timeseries of ripple migrationmeasurements. Ripple migration shows a

consistent pattern of seasonal variation, with maxima in flux during northern-hemisphere autumn and winter at both dune fields. Ripple migration is also observed to decrease away from the upwind margins of dune fields. We compare our observations with predicted sand transport using winds output from the MarsWRF atmospheric circulation model and theories of sand motion. The model predicts half-hourly, mesoscale winds, from which we estimate the 1Hz, local-scale winds by assuming a Weibull distribution of wind speed, with parameters chosen based on landed wind data. This approach uses remote sensing observations of bedform migration, and comparisons with model output, to place constraints on the wind regime. Our measurements of the seasonal pattern of sand flux variation agree, to first order, with predictions based on modeled wind speeds. Comparison of the magnitudes of predicted and observed sand fluxes is not feasible due to the high uncertainties in our calculated sand fluxes caused by uncertainties in input parameters, most importantly the assumed fluid threshold for sand transport. However, we note that model predictions fit our observed sand fluxes best when relatively low values of the fluid threshold shear velocity of ~0.6-0.8 m/s (or shear stresses of $O(10^{-3})$ Pa) are assumed.

### 3.1 Introduction

Aeolian dune fields are abundant across the Martian surface, as revealed in images from as early as the Mariner 9 orbiter in 1971 [*McCauley et al.,* 1972; *Sagan et al*., 1972]. Dunes appear from the circumpolar ergs to crater interiors to the cratered highlands [*Hayward et al.*, 2013; *Banks et al.,* 2018]. Martian dunes were commonly assumed to be inactive [*Parteli & Hermann*, 2007; *Merrison et al.,* 2007] due to the

apparent lack of movement in early, low resolution orbital images, and the presumed difficulty of initiating sand transport in the thin Martian atmosphere [*Greeley et al.*, 1976; 1980].

In situ observations by the Mars Exploration Rovers hinted at active sand transport on modern Mars [e. g., *Sullivan et al.*, 2008]. The arrival of the High Resolution Imaging Experiment (HiRISE) camera aboard the Mars Reconnaissance Orbiter [*McEwen et al.,* 2007] provided more evidence of widespread sand transport on modern Mars. HiRISE's extremely high-resolution (25 cm/pix) imagery resolves the meter-scale ripples that mantle the dunes in active Martian dune fields. These ripples move over timescales of just a few Earth weeks to months [*Silvestro et al.,* 2010*; Bridges et al*., 2012; *Ayoub et al.,* 2014]. Over somewhat longer timescales, the movement of entire dunes is evident [*Bridges et al.,* 2012]. Further work revealed widespread active aeolian transport across the Martian surface [e.g., *Runyon et al.,* 2017a, b; *Baker et al.*, 2018; *Chojnacki et al.,* 2019].

Estimates of sand fluxes associated with the movement of meter-scale ripples and much larger dunes revealed that the two differ widely by a factor of ~5-91 [*Bridges et al.,* 2012*; Runyon et al.,* 2017b]; this difference was assumed to represent the difference between the flux of low-energy reptating grains and the total flux [Saltation + reptation + creep; *Anderson*, 1987; *Andreotti,* 2004], under the assumption that the meter-scale Martian ripples represent bedforms dynamically similar to ~decimeter-scale terrestrial impact ripples [*Anderson,* 1987], which have been scaled up due to the different transport conditions on Mars's surface [*Duran et al.*, 2014]. Though it is widely

agreed that large Martian ripples move primarily by reptation, the ripple height limiting mechanism for small and large Martian ripples is still debated [*Sullivan et al.*, 2020; *Lapôtre et al.,* 2021]. Regardless of the ripple height limiting mechanism, however, ripples only trap a small fraction of the fluxes of sand grains moving in different transport modes over sand dunes, due to their small sizes relative to large saltation path lengths on Mars [*Almeida et al.*, 2009]. Thus, we do not attempt to inform discussion about the origins of large Martian ripples in this work. However, it is still true, regardless of the dynamical origins of ripples, that ripples will migrate more under higher winds and higher overall sand transport. This work thus focuses on using ripple motion to inform our understanding of the dynamics of Mars's atmosphere, and test predictions made by Martian climate models.

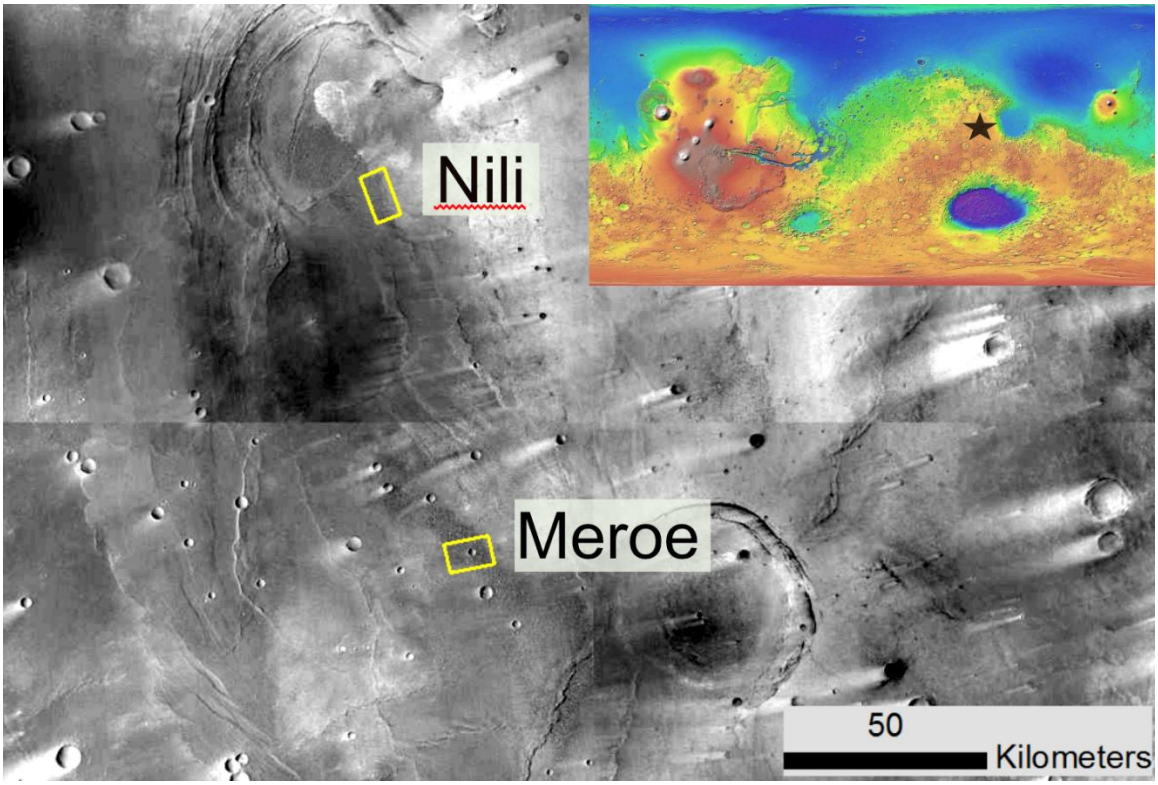

*Fig. 3.1:* CTX imagery of the Syrtis Major region, with Nili and Meroe Patera marked. Location of Syrtis Major is marked by the star in inset global topographic map of Mars.

Monitoring of active Martian dune fields using HiRISE continues to the present day. At the barchan-dominated Nili Patera dune field, located in an extinct volcanic caldera in equatorial Mars (Fig. 3.1), the available timeseries of imagery stretches from 2007 to 2020. We use 5 Mars years (where 1 Mars year = 1.883 Earth years) of this timeseries, from 2007 to 2017, to study bedform motion at Nili Patera. We additionally use a more limited timeseries (1.5 Mars years, from Mars Year 32 to Mars Year 34, due to fewer images having been taken relative to Nili) for a dune field in the neighboring Meroe Patera caldera. On Earth, satellite images such as Landsat can be used to measure the motion of whole dunes [e. g., *Vermeesch et al.*, 2008; *Baird et al.*, 2019]. On Mars, due to the two scales of bedforms (large ripples and dunes) visible from orbit and the very high resolution (25 cm/pixel) of HiRISE imagery, we can apply these timeseries of HiRISE images at Nili and Meroe Paterae to measure both ripple and whole-dune motion. The multi-Mars year timespan of imagery for Nili Patera builds off previous work [*Ayoub et al.,* 2014] by enabling assessment of the interannual variations of the seasonal ripple flux pattern over a longer time period. Furthermore, the long time span of imagery better resolves the motion of slower-moving dunes. We use these measurements to assess Martian winds predicted from general circulation models (GCMs) [*Ayoub et al*., 2014; *Fenton et al*., 2014a, 2014b; *Newman et al.*, 2017].

Previous work [*Ayoub et al.*, 2014] used measurements of seasonal variation in ripple flux to investigate the accuracy of Martian atmospheric model predictions. Since the higher velocity wind gusts thought to be important for initiating sand transport were not predicted by atmospheric models, this work used an "effective threshold" shear velocity to initiate sand transport, which was adjusted so as to fit the observations. This approach prevents inference of the real wind regime from ripple migration measurements as it incorrectly assumes a single threshold for sand transport and doesn't rely on any experimentally calibrated transport law. Actual sand transport is governed by two thresholds; these are the fluid threshold, which governs the initiation of sand transport, and the impact threshold, which governs its continuation. It is, however, possible to reconcile sand flux measurements with wind predictions from atmospheric models by accounting for wind gustiness not resolved by such models using some parameterized distribution function of high wind speeds [*Michel et al.,* 2018]. Building on that idea, we propose a new method to correct Martian GCMs and re-introduce the turbulence they miss, on the basis of wind distributions observed in situ by the few anemometers to have returned data from Mars.

## 3.2 Methods

### 3.2.1 Whole-Dune Motion and Sand Flux

We estimate whole-dune sand fluxes using a subset of images from each respective dune field (Table 1), spaced far apart in time to best resolve whole-dune motion between images. We coregister images using bedrock tiepoints and orthorectify them using the Coregistration of Optically Sensed Images and Correlation (COSI-Corr)

software package [*Leprince et al.,* 2007]. In each set of images, we manually map and track the positions of dune crestlines and slipfaces (Fig. 3.2). We measure dune motion at 107 dunes in Nili Patera and 50 in Meroe Patera. All measured dunes have barchan or barchanoid morphologies, implying a largely unidirectional wind regime, so we take the straight-line difference in crestline positions as representative of the overall displacement of the dunes.

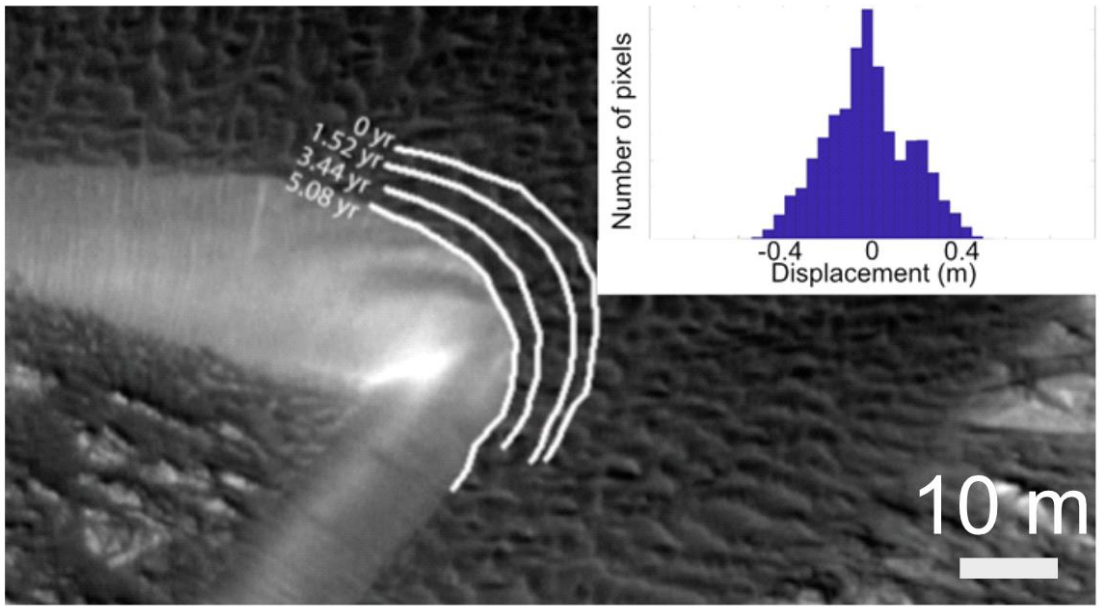


*Fig. 3.2*: Sample measurement of changing crestline positions of a sand dune at Nili Patera. Inset shows a histogram of bedrock misregistration at Nili Patera; the standard deviation of misregistrations is 18 cm (0.72 pixels on the map-projected image). Bedrock misregistration is measured from COSI-Corr correlation results over non-sand-covered parts of the dune field, after ICA (independent component analysis) techniques have been applied to minimize misregistration.

We quantify and include various sources of uncertainty in our displacement measurement. Among these is bedrock misregistration, which we measure using automated COSI-Corr correlation of bedrock in our orthorectified HiRISE images; the standard deviation of bedrock misregistration measurements is 18 cm (< 1 HiRISE pixel). A Digital Elevation Map (DEM) is needed to orthorectify the images, but the dunes themselves form part of the topography, and thus the map changes over time as the dunes move. We use a single DEM, hence some error is introduced. We attempted to generate additional DEMs from HiRISE image pairs over the Nili Patera dune field with SOCET SET DEM-production software, but the DEM production process broke down over the dunes due to the movement of ripples on the dunes, generating "holes" in the elevation profiles over dunes which must be manually fixed. Due to the large time commitment involved in this process, we opted to use a single DEM and estimate the error associated with this limitation, rather than attempt to manually reconstruct multiple DEMs. Additionally, we quantify uncertainty arising from the differing viewing geometries of HiRISE images used in this study.

We convert our whole-dune displacement measurements into measurements of crest and whole-dune translation fluxes via incorporation of measurements of the crest heights, the sand thicknesses averaged over the areas of individual dunes, and the time between successive images. We use heights from HiRISE DEMs generated from stereo images ESP_017762_1890 and ESP_018039_1890 (for Nili Patera) and ESP_050939_1875 and ESP_051084_1875 (for Meroe Patera). We map sand-free areas manually using optical HiRISE images, extract elevation values over these areas, and

interpolate the partial bedrock surface under the dunes, using a thin-plate spline algorithm in ArcMap, to generate a continuous bedrock surface. We then subtract this bedrock elevation dataset from the HiRISE DEM to generate an estimate of dune height for every point in the dune field (Fig. 3.3).

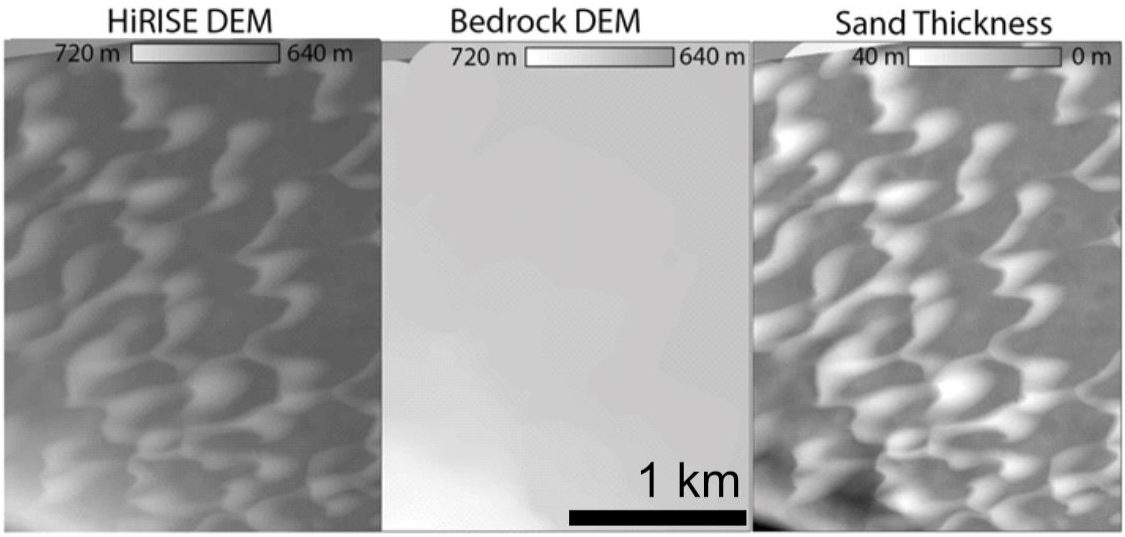


*Fig. 3.3:* Method for calculation of dune heights at Nili and Meroe Patera; the interpolated bedrock DEM is portrayed in the center panel, and resulting sand thickness raster is in the right panel.

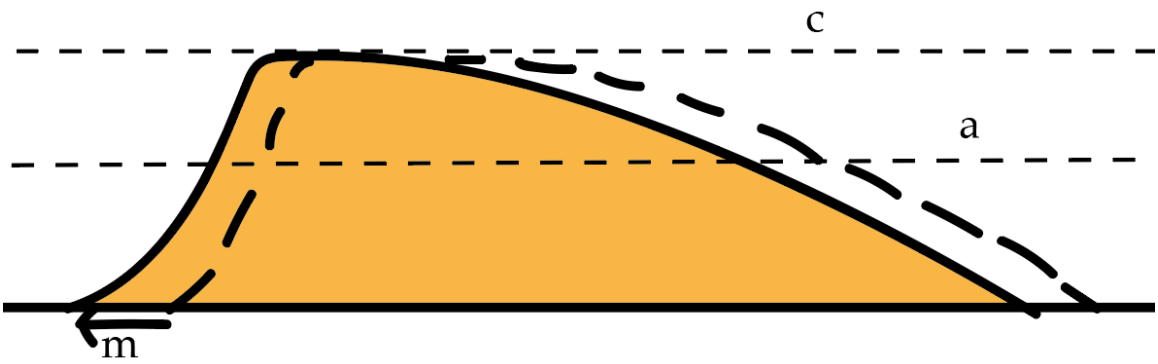

*Fig. 3.4:* Schematic to illustrate difference between crest height **c** and average height **a** of dunes.

Over individual dunes, we extract both crest heights (given by the maximum sand thickness observed at the measured dune) and single dune-averaged heights (given by the average sand thickness observed over the entire spatial extent of a given dune) (Fig. 3.3). We multiply these heights with the dunes' migration rates to generate estimates of the crest flux (from the crest height) and the whole-dune-averaged flux (from the single-dune average height) (Fig. 3.4). Notably, this flux measured from the displacement of bedforms, sometimes referred to as the "translation flux", is a minimal estimate of the actual sand flux at dune fields, as it neglects changes in the shapes and sizes of bedforms, which contribute an additional flux known as the "deformation flux" [*McElroy & Mohrig*, 2009].

The deformation flux is difficult to quantify for our Martian study sites, as measuring shape changes requires estimating the volumes of dunes at different times. Though one HiRISE digital elevation model (DEM) exists at both Nili and Meroe Patera, producing further DEMs at active dune fields generally requires work beyond the standard routine used to generate DEMs from stereo pairs of satellite images. In particular, the movement of the faster-moving ripples between the two images in a stereo pair leads to major errors in generated DEMs which often manifest as "holes" in the DEM which must be filled via extrapolation of the surrounding dune topography. We attempted to produce a DEM from a later stereo pair of images at the Nili Patera dune field (ESP_050438_1890 & ESP_051071_1890) but were stymied by these problems.

Future work into the deformation flux at these Martian dune fields will require confident measurement of the dune topography at different times, ideally widely separated. Though we do not see obvious changes in dune shapes in our studied timeseries of images, the "turnover times" for dunes at the Nili and Meroe study sites are 170 to several thousand Earth years [*Bridges et al.*, 2012], so our timeseries of <10 years of dune displacement measurements is small relative to the timescales over which dunes evolve at these sites. The deformation flux is still thus largely unconstrained; given past experimental studies into other environments, the flux could range from being negligible (~1% of the total), to being larger than the translation flux (~50% of the total or higher). Inference might also be drawn from Earthly sites; past investigation of the interdune flux as it relates to the total dune flux [*Ould Ahmedou et al.*, 2007] has found the interdune flux at a terrestrial dune field to be 1/3 of the crest flux; it is uncertain, however, whether these relations would hold for a Martian dune field given differences in the physics of Martian sand transport.

We estimate the uncertainty on these translation-flux measurements by 1) comparing our crest-height results at dune slipfaces to estimates of their height based on trigonometric considerations using the horizontal slipface length and angle of repose [*Atwood-Stone & McEwen*, 2013], and 2) masking out sections of sand-free topography equivalent in size and shape to individual dunes and performing test interpolations across these areas which could be compared to the actual topography.

### 3.2.2 Methods – Ripple Motion and Sand Fluxes

At Nili Patera, we measure ripple motion with a timeseries including 40 pairs of images acquired over a total interval of ~3.8 Mars years. At Meroe Patera, the timeseries includes 11 pairs of images acquired over ~1.5 Mars years. We correlate input HiRISE images using the automated subpixel image correlation techniques incorporated in the COSI-Corr software package [*Leprince et al.,* 2007]. For ripples, the favored technique involves using the Pearson statistical correlation coefficient to match a patch of an image with its most similar candidate patch in the second image. The relative similarity of different patches of an image is defined via the use of the Fourier transform to characterize patterns of spatial variation in an image patch.

From each pair of optical images, we produce two correlation maps (Fig. 3.5), which indicate the magnitude and direction of apparent displacement of surface features at each position in the image. Two correlation maps are produced per pair to express displacements in the E-W and N-S axes. Study of our correlation maps reveals various patterns of apparent displacement; as an example, in Fig. 3.5 the dark tone of dunes in the correlation map indicates apparent displacements of the surface features on these dunes (the ripples) towards the west. Given the geological context of a barchan dune field with westward-facing slipfaces, these apparent displacements are an expected signal which reflects real displacement of the surface.

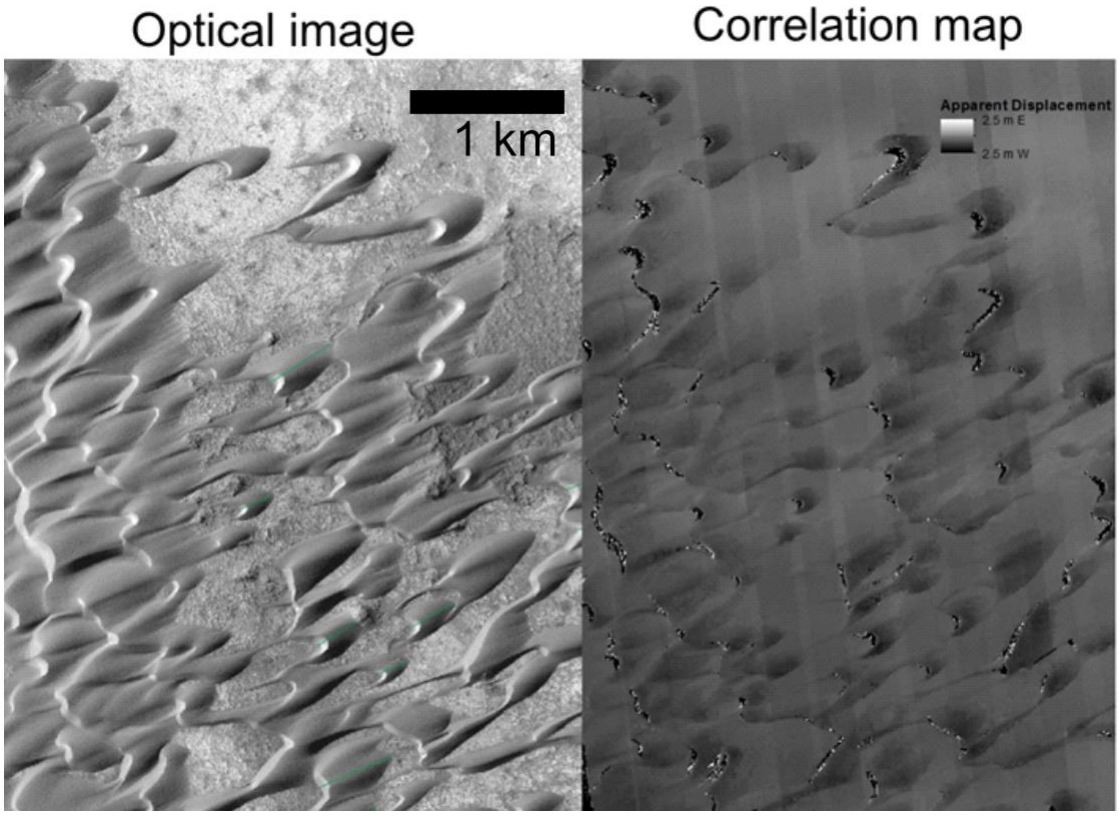


*Fig. 3.5:* Side by side comparison of an example HiRISE optical image and correlation map, generated from a pair of HiRISE optical images in COSI-Corr, of the Nili Patera dune field.

However, the correlation results show discontinuities forming stripes perpendicular to the satellite track and undulations along track. These artifacts are particularly visible in the interdune areas where there should be no motion. Such artifacts are common in images acquired via push-broom systems and are caused by satellite jitter and CCD misalignments [*Leprince et al*., 2008]. To minimize the impact of these artifacts, we test the PCA (Principal Component Analysis) and FastICA (Independent Component Analysis) [*Hyvärinen & Oja*, 1997] algorithms available in the ENVI software package. First, we use a PCA-based method [*Kositsky & Avouac*, 2010] to

fill in missing "no data" pixels output in our correlation maps. A timeseries of *n* spatially coincident correlation maps is projected into an *n*-dimensional space as a point cloud, with each pixel at a particular spatial position represented as a point in the cloud, with its value in each spatial dimension set by the pixel's scalar value in each correlation map. In both the PCA and the ICA decomposition, the data matrix X is expressed as $X = \sum_i U_i S_i V_i$ , where $U_i$ represents the spatial pattern associated to component *i*, $V_i$ is a vector representing the temporal variations of the contribution of this component to the measurements, and $S_i$ quantifies the contribution of component *i* to the data variance.

A set of component vectors is fit to each *n*-dimensional point cloud; in the case of a PCA, all components are mutually orthogonal and are ranked, with the first component being that which explains the largest amount of data variance, the second having the second largest variance, and so on. In the case of an ICA, the components are determined so as to maximize their independence. They are therefore not forced to be orthogonal. For our analyses, we aim to merely separate out the signal of surface displacements associated with ripple motion, which in many image pairs is the largest source of variance. Thus, a PCA is often sufficient to separate the ripple displacement from artifacts [*Ayoub et al.*, 2014]. In that case, the first few components show mostly the ripple migration signals and the higher components show mostly the artifacts. If ripple displacement is not the dominant source of data variance in the time series, then even the first components in a PCA are contaminated with artifacts. The ICA technique is then more appropriate. The artifacts and the bedform migration signal show up in

different components (Fig. 3.6), as the signal from bedform migration is not correlated with the jitter and CCD artifacts.

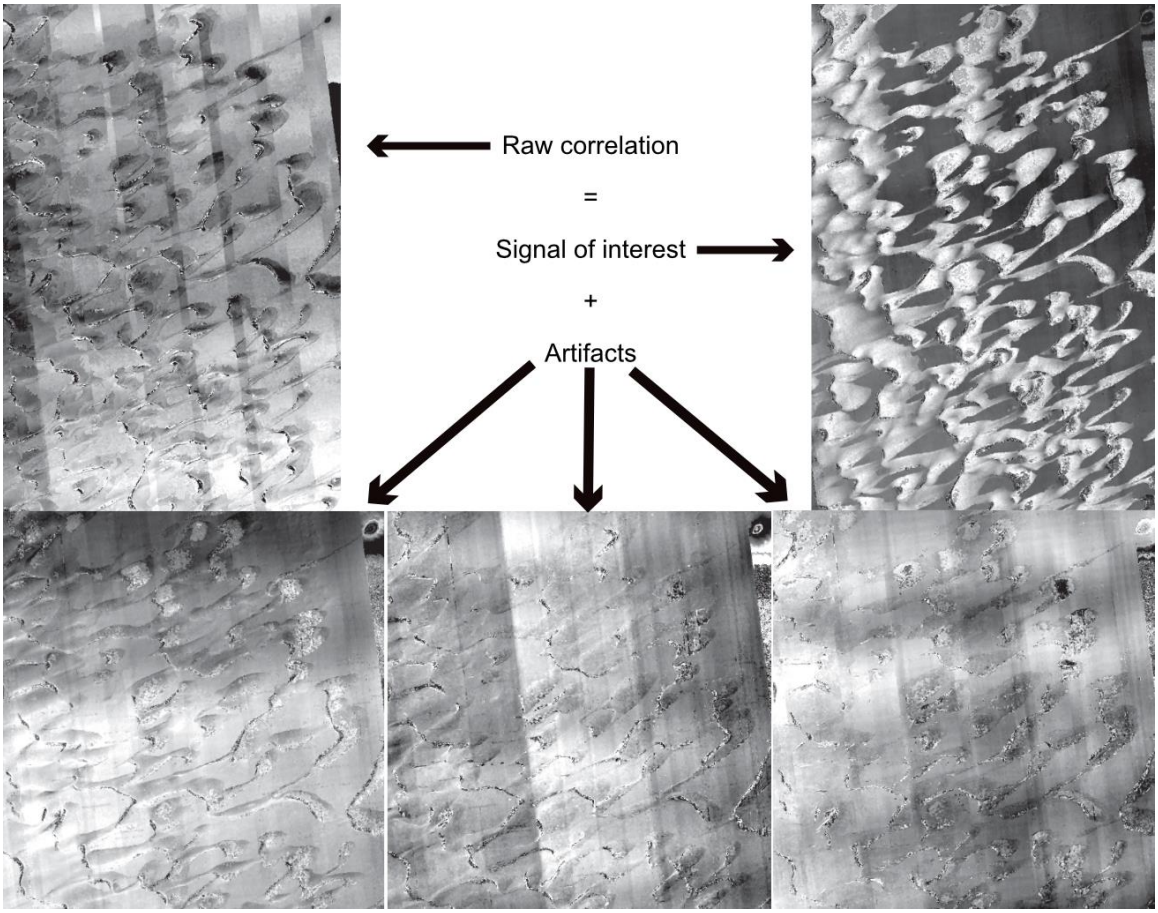


*Fig. 3.6:* Separation of ripple migration signal and artifacts in correlation maps using a PCA (principal component analysis). The top left image is an example of a correlation map. The other panels show the dominant components obtained from PCA applied to the complete time series. The ripple migration signal is clearly dominant in PC1 while the other components include artifacts arising from spacecraft jitter and CCD camera misalignment (broad "parabolic" residual displacement in left panel; vertical striping in middle panel; along-track jitter and finer vertical striping in right panel).

We extract the components identified from PCA/ICA that contain clear signals of ripple motion over dunes, and generate reconstructed correlation maps using only these components. We then put these reconstructed maps through a final processing step, consisting of quantification of remaining apparent displacements over bedrock areas (which must be artifacts as the bedrock will not have moved); lastly, we extrapolate this displacement over the dune areas and subtract it from the correlation map, yielding the final "cleaned" displacement results.

We repeat the ICA analysis individually for correlation maps representing the N-S and E-W components of motion at each dune field. We sum the "cleaned" resulting displacement vectors to determine magnitudes and directions of apparent displacements at the end. We quantify uncertainty on measurements of ripple displacement as was done for whole-dune displacement measurements. We measure remaining apparent displacements of bedrock, and also calculate possible errors resulting from the use of a single DEM to define dune heights, and from the differing viewing geometries of subsequent images.

Maps of ripple speed can be converted to ripple sand fluxes by multiplying by the estimated half-height of the ripples, but this process is fraught with uncertainty due to the uncertain small-scale geometry of the ripples. Previous work [*Bridges et al.*, 2012] assumed that the ripples should have morphologies analogous to terrestrial impact ripples, and assumed a consistent wavelength, and a height to wavelength ratio of 1:10; this corresponds to a "ripple index" (ripple wavelength divided by crest height) of 10, an average ripple crest height of ~40 cm, and an average half height of ~20 cm. The half-

height, representing the average thickness of sand associated with the ripples, can be multiplied by its migration rate to derive a sand flux associated with the ripples. However, Earthly impact ripples show variations in ripple index from 10-25, with even higher values of the ripple index sometimes observed in very well sorted sands [e. g., *Bagnold,* 1937; 1941; *Sharp*, 1963]. In situ measurements [e. g., *Lapôtre et al.*, 2018], though still limited in extent, show variability in ripple morphology, including in ripple index and half-height. We therefore present assumed ripple fluxes, and ripple-to-dune flux ratios, corresponding to low- and high-end estimates of the ripple index corresponding to the range of ripple indexes found in Earthly ripples studied in field settings. We have, however, verified the consistent average ripple wavelength of 4.6 m found by *Bridges et al.* (2012) via mapping in HiRISE images; this wavelength implies possible ripple half-heights varying from 8 to 20 cm.

For perfectly straight-crested ripples, our method would not allow detection of any sand flux parallel to the crest lines. The technique we use should, in principle, fail in that case. However, we observe that even where the ripples are relatively straight-crested they have along strike irregularities, such as junctions between ripple crests, that allow for confident tracking of their migration. We additionally note that the azimuth and magnitude of migration is consistent between relatively linear ripples and over nearby more irregular ripples (typically found closer to the crests of the dunes) (Fig. 3.7). Thus, we believe that along-crest transport is likely to be minimal. Declines in ripple flux near the edges of dunes are likely to be related to the lower elevations of these

areas relative to the central areas of dunes, which protrude more into the oncoming wind.

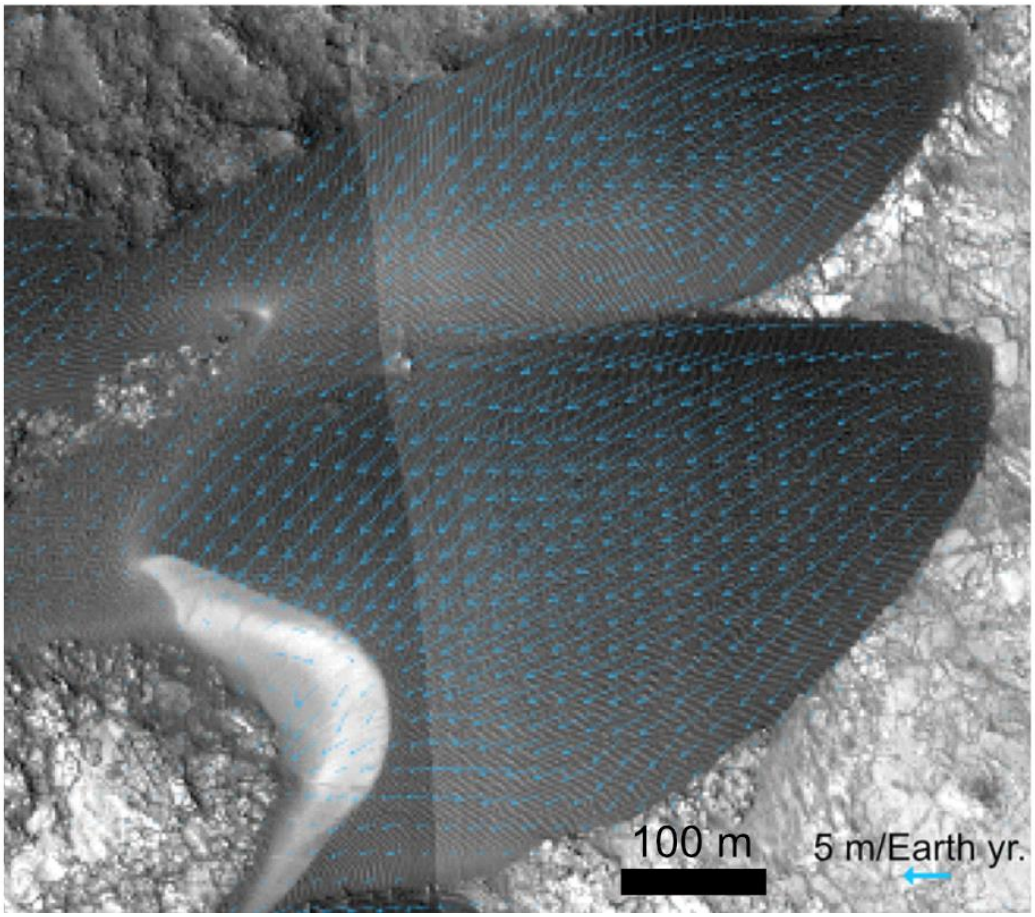


*Fig. 3.7:* Example vector-field map of ripple displacement directions and magnitudes over a sand dune at Nili Patera.

For all bedforms, the migration of the bedform multiplied by its average height yields the volume of sand, traveling through a unit length of a line oriented perpendicular to the sand transport direction, in a unit length of time. So, the sand flux unit is $m^3/m/Earth\ yr$, simplified to $m^2/Earth\ yr$.

### 3.2.3 Predicted wind stresses and directions from an atmospheric model

We compare our measured sand fluxes to fluxes derived from results from the MarsWRF atmospheric model, a multiscale, nonhydrostatic Martian implementation of the planetWRF model [*Richardson et al.*, 2007, *Toigo et al*., 2012] based on the NCAR Weather Research and Forecasting (WRF) model developed for Earth. The setup of MarsWRF for multiscale modeling is described in detail in *Newman et al.* [2017, 2019, 2021], so we provide only a summary of the main features here. MarsWRF includes parameterizations of processes including boundary layer and free atmosphere horizontal and vertical mixing, radiative transfer through a dusty $CO_2$ atmosphere, transport and exchange of heat between the subsurface, surface, and atmosphere, and the $CO_2$, dust, and water cycles, although the water cycle and dust / water-ice coupling are not included in these simulations. While MarsWRF may be run with interactive dust (dust lifting, transport, and sedimentation), in the simulations shown here we instead prescribe the time-evolving 3-D dust distribution based on Mars Global Surveyor Thermal Emission Spectrometer nadir and limb data [as described in *Newman et al.,* 2021] to ensure that the dust distribution and hence dust forcing is realistic. MarsWRF also parameterizes the exchange of momentum between the surface and atmosphere, which includes the diagnostic calculation of drag velocity, $u_*$, from the wind speed at the surface given estimates of surface roughness. MarsWRF also outputs pressure at the surface and atmospheric temperature at 1.5m, which may be used to determine near-surface air density (hence wind stress in combination with $u^*$), as well as zonal and meridional wind speed at 1.5m, providing near-surface wind direction.

We ran a global MarsWRF simulation at 2° horizontal resolution and also a multiscale simulation in which two additional domains were 'nested' inside the global domain, with a three-fold increase in horizontal resolution in each domain compared to its parent and with two-way exchange of information between child and parent domains. In these multiscale simulations, the innermost domain (domain 3) therefore had a horizontal resolution of ~13-km, allowing the effects of local scale topography and other surface properties on wind stress to be captured, as well as global and regional scale flows. Both the global and multi-scale simulations were set up as described in *Newman et al.,* 2021, which shows MarsWRF predictions for the Mars 2020 landing site in nearby Jezero crater; domain 3 of the Mars 2020 simulations covers Nili and Meroe Patera, thus results from the same simulations could be used for both studies. While global MarsWRF is typically run with its top layer centered well above 80km, to capture the full extent of the vigorous overturning circulation at the solstices, in these simulations a vertical grid with 43 layers and with the top layer centered at ~50km altitude was needed to maintain stability of the nested high-resolution domains. This may have impacted results, as discussed later in the manuscript.

### 3.2.4 Calculating predicted sand fluxes using MarsWRF output

For global simulations, the model was run continuously over a Mars year, with an output frequency of 1 Mars hr., which was sufficient to capture the variability in wind simulated at this spatial resolution. For domain 3, the model was run for seven representative sols at intervals of 30 degrees of areocentric solar longitude (Ls), with 12 runs performed to sample the full Mars year. The model was output every 1 Mars hour,

which was again sufficient to capture wind variability at this higher spatial resolution. Note that a Mars hr. is 1/24$^{th}$ of a Mars day (sol). Average sand flux was calculated for each of the 12 Mars year increments (covering intervals of 30 degrees Ls each) by applying the measured ripple speed between each individual image pair as a constant flux through its respective time period. The portion of each 30 Ls increment covered by a particular image pair was calculated, and a weighted-average ripple speed was calculated for each increment. The fluxes in the same increment from each Mars year covered by our timeseries were averaged to generate a multiyear-averaged observed flux. We then multiplied the measured ripple speeds by a constant to scale them into fluxes with a yearlong average equal to our observed average whole-dune fluxes at Nili and Meroe. This generates a predicted seasonal pattern in whole-dune flux variation from our observed ripple migration pattern.

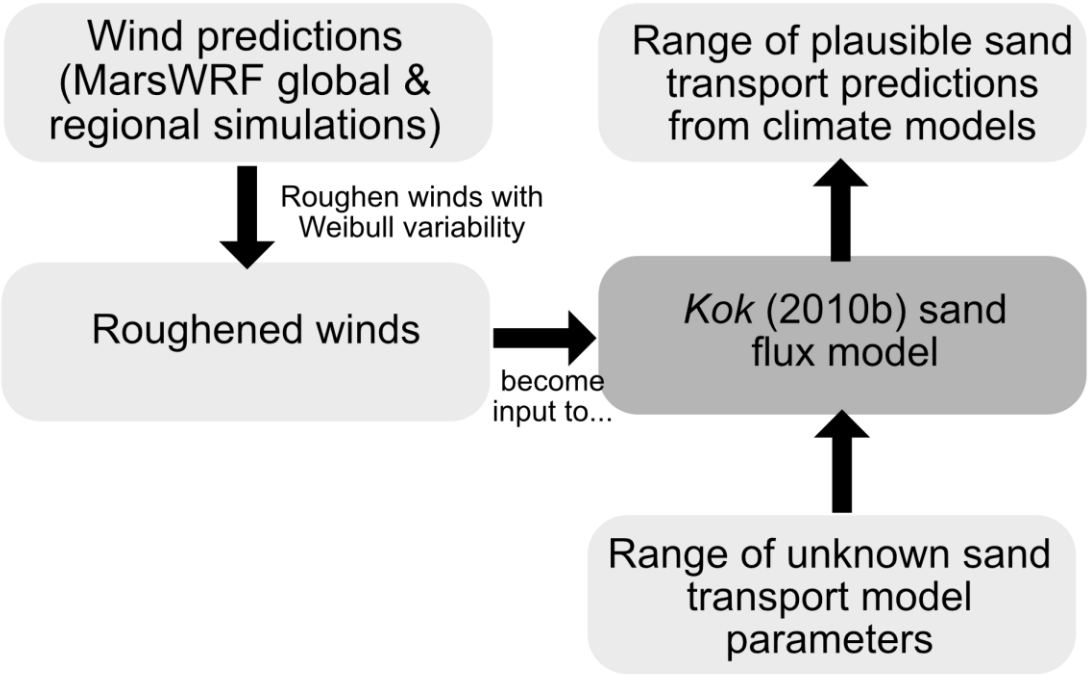

*Fig. 3.8:* Flowchart depicting the basics of our sand transport modeling scheme.

Our overall sand-flux modeling scheme is summarized by the above flowchart (Fig. 3.8). The sand flux associated with model-predicted winds is calculated from relationships derived in *Kok* (2010b). These assume that sand motion is first triggered when wind stress exceeds a fluid threshold, $u_{ft}^*$, but that once initiated sand motion will continue provided the wind stress exceeds a lower threshold: the impact threshold, $u_{it}^*$. This is due to the impact of saltating sand grains on the surface increasing the total stress, thus requiring less stress to be contributed by the wind. From *Kok* (2010b), the probability of sand transport occurring at a given time is defined as

$$P_{tr} = \exp\left\{-\left[\frac{u_{ft}^*\Gamma\left(1+\frac{1}{k}\right)}{\bar{u}^*}\right]^k\right\} + \exp\left\{-\left[\frac{u_{ft}^*\Gamma\left(1+\frac{1}{k}\right)}{\bar{u}^*}\right]^k\right\} \times \ldots$$

$$\ldots \frac{\exp\left\{-\left[\frac{u_{it}^*\Gamma\left(1+\frac{1}{k}\right)}{\bar{u}^*}\right]^k\right\} - \exp\left\{-\left[\frac{u_{ft}^*\Gamma\left(1+\frac{1}{k}\right)}{\bar{u}^*}\right]^k\right\}}{1-\exp\left\{-\left[\frac{u_{it}^*\Gamma\left(1+\frac{1}{k}\right)}{\bar{u}^*}\right]^k\right\} + \exp\left\{-\left[\frac{u_{ft}^*\Gamma\left(1+\frac{1}{k}\right)}{\bar{u}^*}\right]^k\right\}}, \quad (1)$$

where $u_{it}^*$ is the impact threshold, $u_{ft}^*$ is the fluid threshold, $\bar{u}^*$is the average shear velocity, $\Gamma$ is the gamma function, and *k* is the shape parameter of the Weibull distribution assumed to fit observed winds. The sand flux is then defined as $Q = P_{tr} C_Q \frac{\rho_a}{g}(u^* - u_{it}^*)(u^* + u_{it}^*)^2$, where $C_Q$ is a proportionality constant equal to 2.61 [*White,* 1979], $\rho_a$is the air density, and *g* is Mars's surface gravity. These relations derived by *Kok* (2010b) are used because they account for hysteresis caused by the discrepancy between the fluid and impact thresholds for sand transport, which is

believed to be much larger on Mars than it is on Earth, although studies (both laboratory and theoretical/modeling) show a wide spread in the expected ratio between the two thresholds, due largely to uncertainty in the calculations proposed for the fluid threshold, which may vary from ~$10^{-3}$ [*Swann e. a.,* 2020] to $10^{-1}$ Pa [*Greeley et al*., 1980]. Neither the fluid nor impact threshold has been measured on Mars, thus we must rely on relationships obtained from theory/modeling and from laboratory studies under partial Mars conditions to estimate their values. In this paper, we primarily use the expressions for the impact threshold from *Kok*, 2010a (eq. 25) and for the fluid threshold from *Swann et al.*, 2020 (eqs. 4, 6, 7). The estimated shear velocity at the impact threshold, calculated independently for each time step from the atmospheric pressure and temperature predicted by MarsWRF, varies from 0.0055 to 0.0066 m/s, corresponding to a shear stress of 3 - 6 * $10^{-7}$ Pa; for the fluid threshold, predicted values range from 1.26 – 1.44 * $10^{-3}$ Pa, or 0.6-0.76 m/s in terms of shear velocities. We also consider the impacts of much higher or lower assumed fluid threshold values on our model.

Because of the relatively coarse spatial and temporal scale of the model, even in domain 3, small-scale turbulence leading to variability in wind speeds is not represented well in the model simulations. We therefore design a scheme to reintroduce this variability. We assume that the distribution of wind speed is a Weibull distribution, with $f(v) = (\frac{k}{c})\left(\frac{v-\mu}{c}\right)^{k-1}(\exp\left[-\left(\frac{v-\mu}{c}\right)^{k}\right])$, where *v* is the wind speed, *c* is a scale parameter, $\mu$ is a location parameter, and *k* is a shape parameter.

This distribution of wind speed is commonly observed on Earth [*Justus et al.*, 1978], and is consistent with the data available from Mars [*Viúdez-Moreiras et al.*, 2019]. Each model wind prediction (the probability distribution of these is given in Fig. 3.9) is set as the average wind speed for a Weibull distribution of winds with a shape parameter $k = 3$. $k = 3$ is set as a typical representative $k$ value given the fact that Weibull parameters observed at the InSight landing site (Fig. 3.10) generally vary between $k = 2$ and $k = 4$, though we also consider the impact of higher and lower assumed $k$ values on sand transport later. In particular, we also consider assumed $k$ parameters of 2 and 8 as low- and high-end cases, as these values represent the extremes of the distribution observed at the InSight site. We compare the magnitude and direction of model-predicted sand transport to our observations.

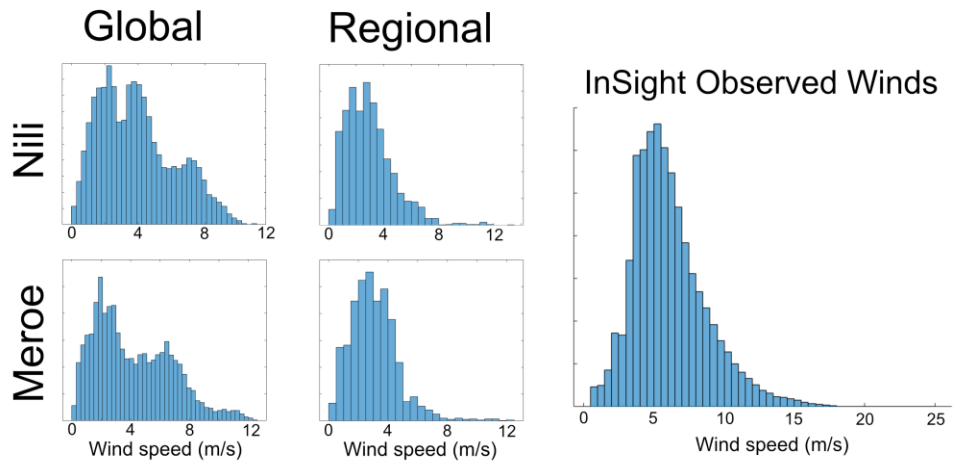

*Fig. 3.9:* Distribution of wind speeds predicted by MarsWRF forecasting model at Nili and Meroe Paterae, from global and regional MarsWRF models. Right – Distribution of wind speeds observed at Elysium Planitia by the InSight lander.

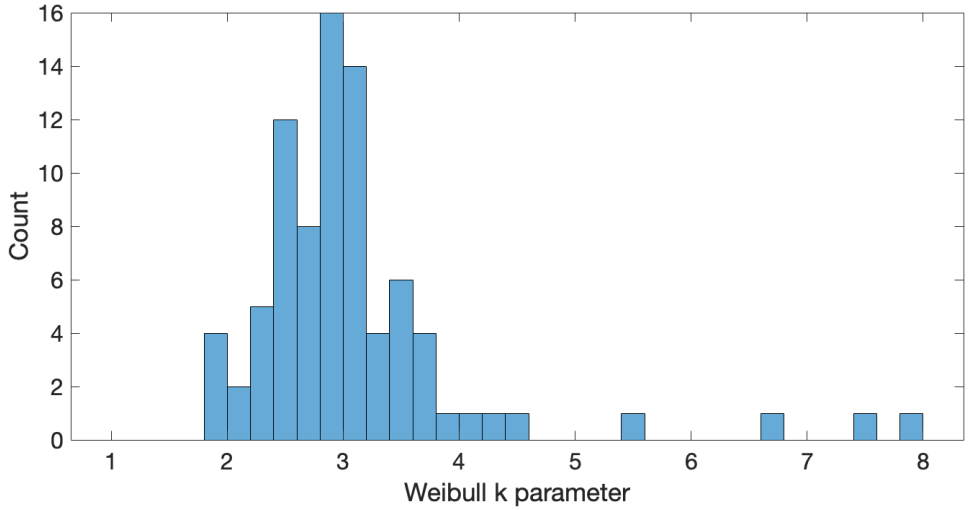


*Fig. 3.10:* Histogram of Weibull *k* parameters fit to 1-day compilations of wind data from InSight.The 'count' number corresponding to each bar is the number of days whose wind data is best fit by a *k*-parameter in the range indicated by the bar.

Though we assume relatively low values of the fluid threshold, other past wind-tunnel studies [e. g., *Greeley et al.*, 1980; *Iversen & White*, 1982; *Musiolik et al.*, 2018] have suggested different calculations of the fluid threshold for Mars, producing values as high as ~2.2 m/s. If we apply these values to our modeling, we predict magnitudes of sand transport an order of magnitude lower than those we predict with *Swann et al.* 2020 thresholds. Combining this uncertainty with uncertainty in other parameters, including the sand grain size distribution present at Nili and Meroe, the impact threshold, the *White* 1979 constant $C_Q$, and others, produces massive uncertainty in our

sand flux predictions. Thus, we focus less on trying to fit magnitudes of observed sand fluxes to observations, and more on trying to fit the timing of seasonal variations in the flux.

We also consider a more simplified sand-flux parameterization directly following the method of *Ayoub et al.* (2014), to see how the fit from the new GCM implementation compares to the old fit presented in that study. This approach introduces no imposed variability to the wind regime; fluxes are calculated directly from the threshold for motion and the shear velocities and atmospheric densities output by the climate model. This approach also assumes only a single "effective threshold" shear stress for sand motion, which we set equal to the threshold of 0.01 Pa found to be the best fit to early observations by *Ayoub et al.* (2014). For the sand flux law, we use the *Lettau & Lettau* (1979) relation: $Q = \rho u^{*2}(u^* - u_t^*)$, where $\rho$ is the atmospheric density, $u^*$ is the model-predicted shear stress, and $u_t^*$ is the effective threshold for sand motion.

## 3.3 Results

### 3.3.1 Whole-Dune Motion and Sand Flux

Spatial views of our whole-dune displacement and flux measurements can be found in Fig. 3.11 (Nili Patera) and Fig. 3.12 (Meroe Patera). Speeds of dunes vary from ~0.2 to 1.5 m/Earth yr; dune speeds are generally anti-correlated with dune height, with larger dunes moving more slowly as commonly observed on Earth [*Hersen et al.,* 2004; *Bridges et al*., 2012] (Fig. 3.13). These migration rates are comparable to the ~1.5

m/Earth yr migration rates observed at dunes in Antarctica [*Bourke et al*., 2009]. The data points tend to follow the trend expected for a consistent sand flux (the dune migration rate increases as the dune height decreases, since the motion of smaller dunes involves smaller volumes of sand, such that the product of these two quantities is constant), as is typically observed on Earth. Typical whole-dune translational sand fluxes for Nili and Meroe Patera are ~7 $m^2$/Earth yr (Fig. 3.13), with a range from ~3 to 13 $m^2$/Earth yr. Maximum fluxes, as measured at dune crestlines, are ~8 to 32 $m^2$/Earth yr, with an average of ~16 $m^2$/Earth yr. There is no clear trend in the spatial variation of dune flux, although at Meroe, there is a tendency towards lower sand fluxes in dunes further away from the upwind margin of the dune field.

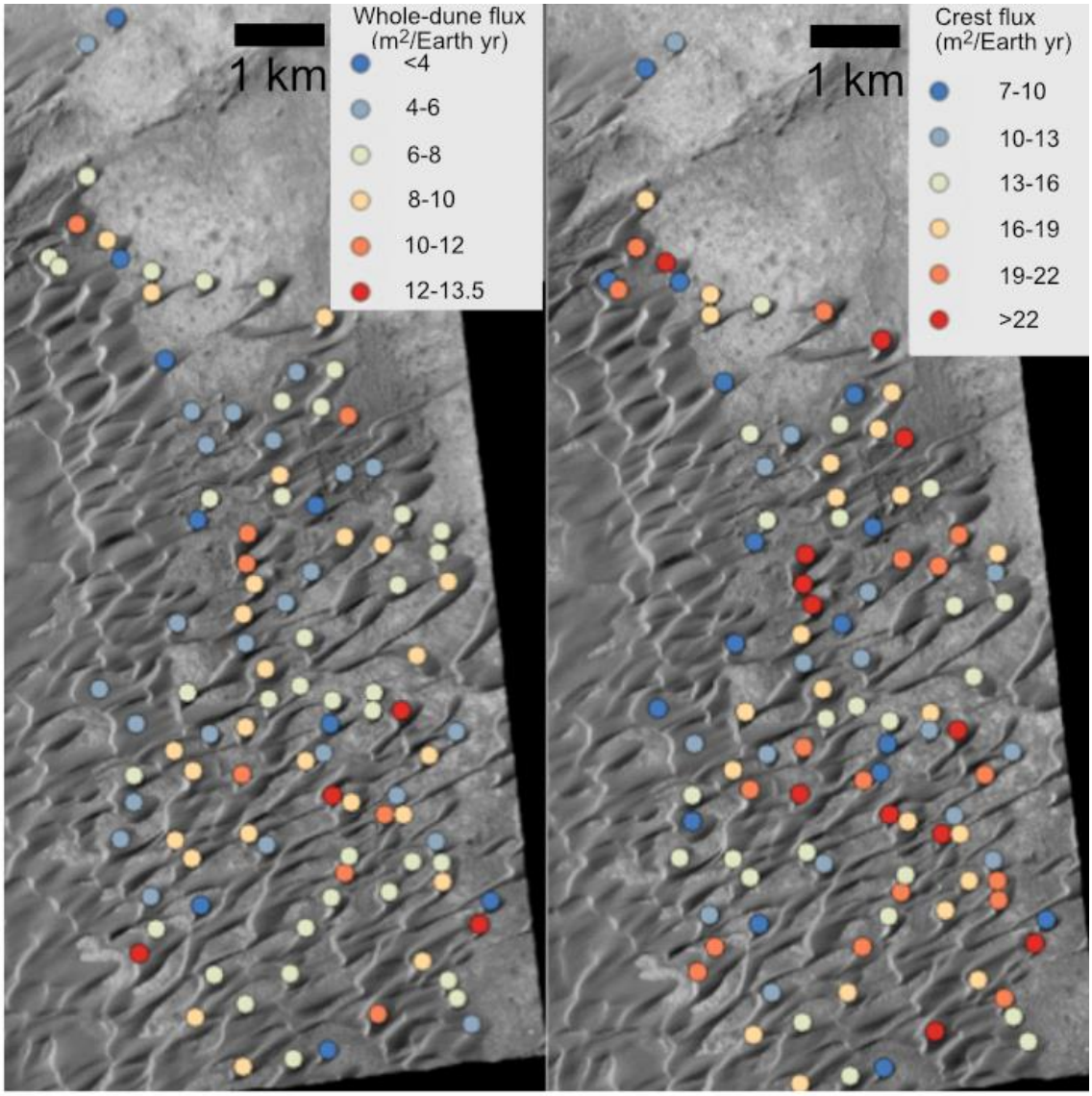


*Fig. 3.11:* View of spatial positions of whole-dune flux and crest flux measurements for Nili Patera, with colored points to indicate magnitude of flux.

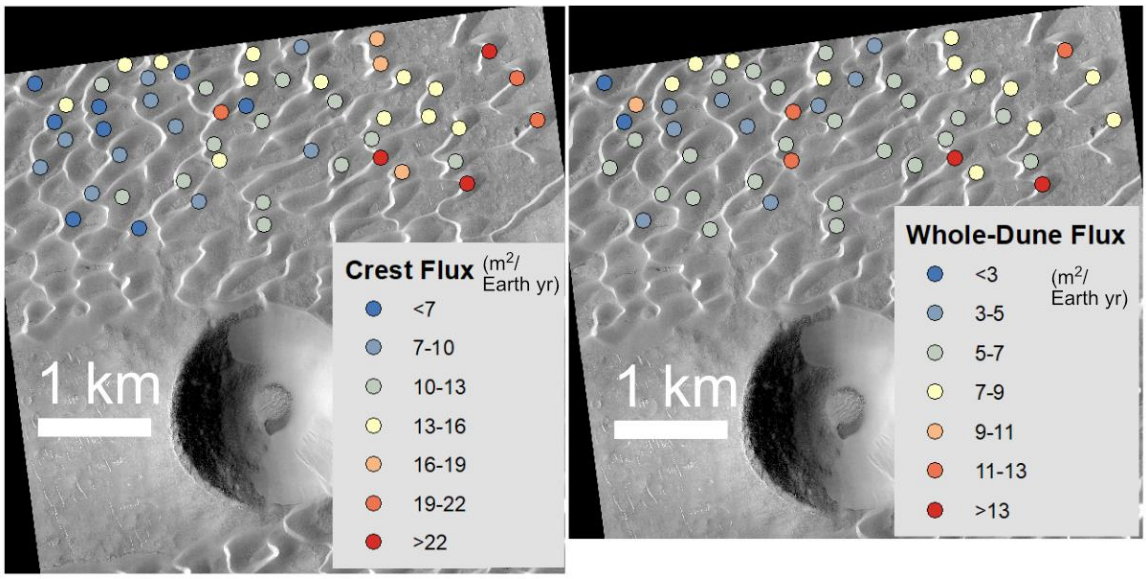


*Fig. 3.12:* View of spatial positions of whole-dune and crest flux measurements for Meroe Patera, with colored points to indicate magnitude of flux.

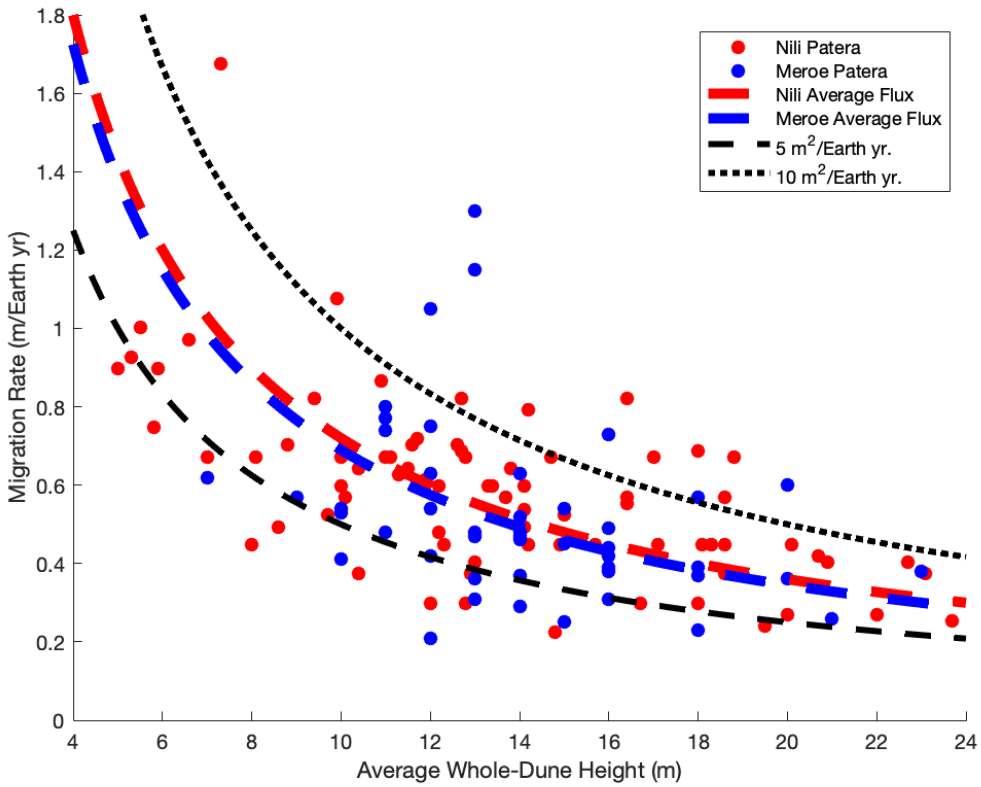

*Fig. 3.13:* Dune height vs. migration rate at Nili and Meroe Patera, with curves corresponding to the average flux at each site, and sample sand-flux values overlaid. The migration rate, multiplied by the dune height, is the translation flux associated with dune motion.

### 3.3.2 Ripple Speed and Sand Flux

Ripple speeds observed at Nili and Meroe vary from ~1-10 m/Earth yr, with typical long-term average speeds of ~4 m/Earth yr. On the scale of individual dunes, ripples typically move faster at higher elevations and at positions closer to the crestline positions. Vector maps of ripple motion (Fig. 3.7) show that ripples tend to wrap around the sides of dunes, converging on the dune crestlines. The averaged vector displacements of ripples over a particular dune are generally very similar to the transport direction implied by the barchan dune geometry.

Measurements of ripple speed show a pattern of consistent maxima around northern hemisphere autumn and winter (~Ls 240-360) (Fig. 3.14). Some image pairs, particularly around the high-flux part of year in Mars Years 31, 32, and 33, show decorrelation of the ripple pattern (i.e., losing track of the ripples) preventing ripple displacement measurement as shown by gray bars in Fig. 3.14. The decorrelation of the ripple pattern indicates large displacement and possible rearrangement of the ripple pattern; however, the loss of the correlation prevents measurement of ripple displacement. The large displacements in decorrelated image pairs are due to some combination of high sand flux and long times in between image acquisitions. However,

the images used in the Mars Year 31 & 32 decorrelated pairs are not separated exceptionally far apart in time (95 and 73 Earth days, respectively; there are four image pairs spaced further apart in time which did not decorrelate). Thus, exceptionally high sand flux or variable transport direction are the likely causes of these decorrelations. The decorrelated image pair in Mars Year 33 involves two images taken further apart in time (123 Earth days), so there is less of a need to invoke particularly high fluxes as an explanation. Long-term averaged ripple sand flux estimates vary from ~0.8 $m^2$/Earth yr., under an assumed ripple index (RI; ripple wavelength divided by height) of 10 (relatively steep/tall ripples) to ~0.3 $m^2$/Earth yr. under an assumed ripple index of 25 (relatively shallower/short ripples).

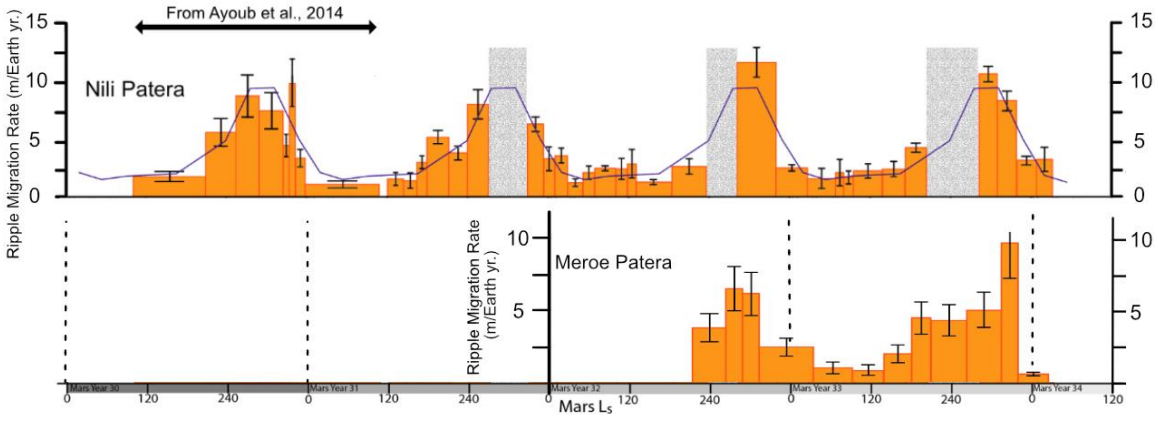


*Fig. 3.14:* Ripple migration rate measurements at Nili and Meroe Patera. Vertical red lines indicate dates of image acquisition. The ripple speed between two successive acquisitions is represented by the orange bars with error bars showing the 67% confidence uncertainty; the width of the bar indicates the length of time represented by its associated image pair. A multi-annually averaged curve of ripple migration through a

Martian year (dark line) is overlaid on the Nili Patera timeseries. Gray bars indicate unrecoverable ripple displacement data in which the ripple pattern was rearranged or excessively displaced; sand flux was high during these periods, but cannot be quantified.

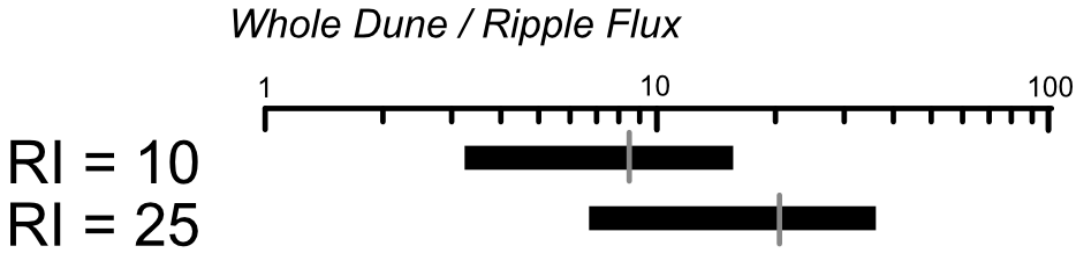


*Fig. 3.15:* Ratio between ripple and whole-dune fluxes for all dunes at which both were acquired at Nili Patera, for two different assumed values of the ripple index (RI), which is the ripple wavelength divided by the ripple height. Lower RIs indicate relatively taller, steeper ripples.

Given these uncertainties, the average dune:ripple flux ratio, averaged over all the studied dunes at Nili Patera, may vary from ~8.4:1 to ~21:1 (Fig. 3.15). We have calculated the dune-to-ripple flux ratio for individual dunes at Nili Patera, and the range of these ratios is provided by the boundaries of the bars in Fig. 3.15. In the RI = 10 case, dune-to-ripple flux ratios vary from 3:1 to 15:1 at individual dunes. If a high RI of 25 is assumed, the ratio would vary from 7.5:1 to 37:1 at individual dunes. The ripple flux shows clear patterns of spatial variation at Nili and Meroe Paterae, in somewhat of a contrast to the dune flux (Fig. 3.16, Fig. 3.17). Ripple fluxes are consistently elevated in more upwind parts of the dune fields at Nili and Meroe, based on these results; this

finding is also in agreement with previous studies of dune-field-scale changes in ripple flux [*Runyon et al*, 2017b].

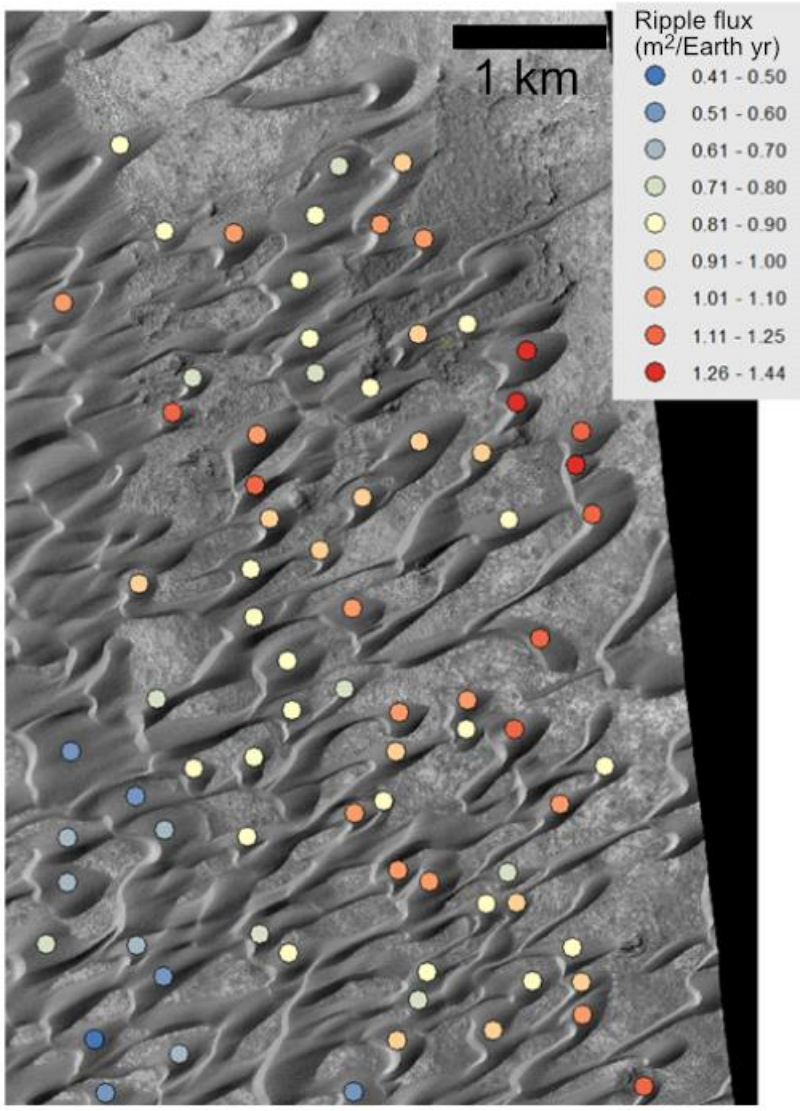


*Fig. 3.16:* View of spatial positions of ripple flux measurements at Nili Patera, with magnitudes of flux indicated by color of measurement points. Note that upwind dunes tend to have higher fluxes than downwind dunes.

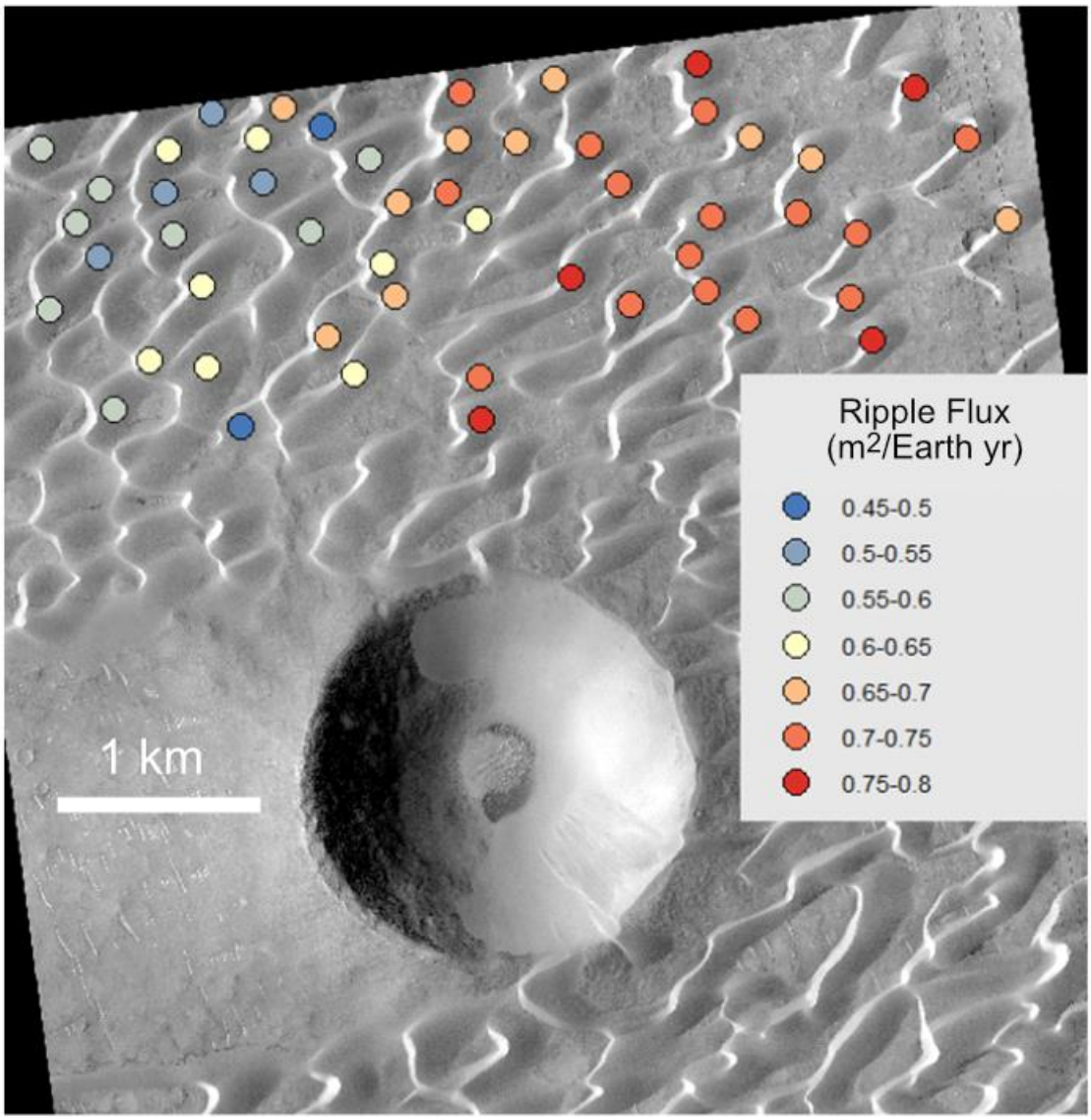


*Fig. 3.17:* View of spatial positions of ripple flux measurements at Meroe Patera, with magnitudes of flux indicated by color of measurement points. Note that upwind dunes tend to have higher fluxes than downwind dunes.

### 3.3.3 Comparison between observed and predicted sand fluxes

Atmospheric models predict the directions of observed highest winds, and sand transport accurately at Nili and Meroe Patera (Fig. 3.19). During high-flux periods the

sand transport direction is consistently predicted to be towards ~20 to 30 degrees south of due west; this corresponds well with observed ripple motion, and with the axes of symmetry of the barchan dunes at Nili and Meroe Paterae. The atmospheric models' fit to the seasonal pattern of high/low sand fluxes is reasonably good at Meroe but poor at Nili using the global MarsWRF output. The increase in sand flux around Ls = 240 is replicated in model predictions, though winds decrease too early in northern-hemisphere fall in the model (Fig. 3.18, left panels). Additionally, at Nili there is a secondary increase in model wind predictions early in the year, around Ls = 30, which is not reflected in observations. In domain-3 (high-resolution) simulations, the problem of premature decrease in wind and sand flux becomes more pronounced (Fig. 3.18, right panels), but there is now a clear peak at Nili at Ls~240° only, which is in better agreement with observations. Additionally, if we assume fluid thresholds following the *Swann et al*. (2020) calculations, the magnitudes of observed sand flux correspond well with observations at both Nili and Meroe Patera.

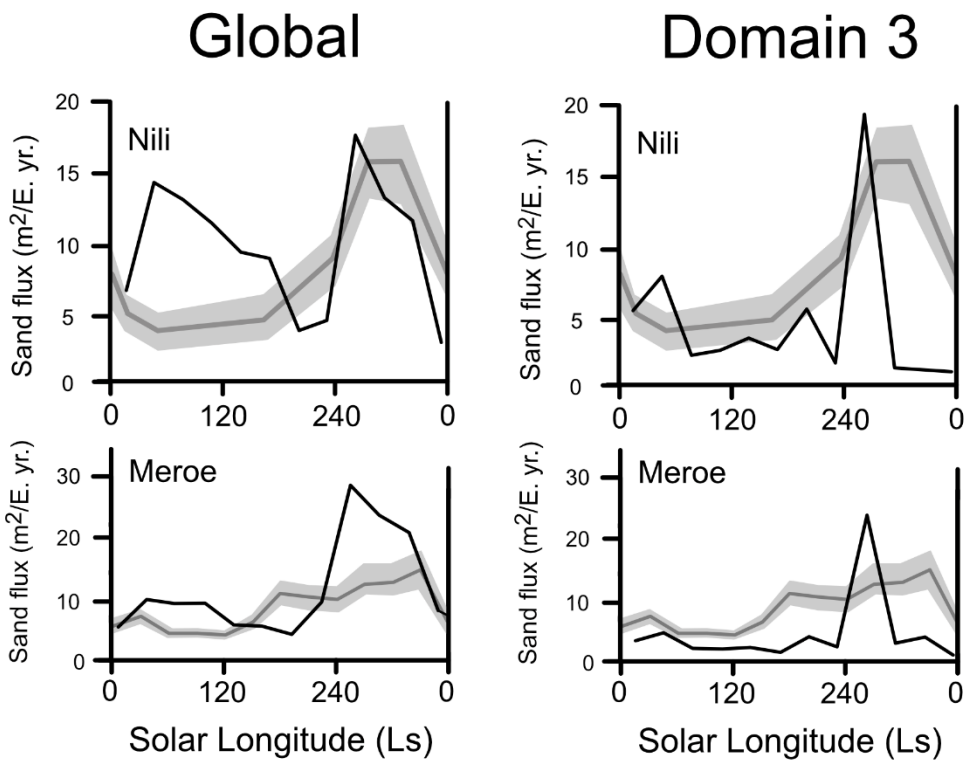


*Fig. 3.18:* Comparison of observed (gray line, with uncertainty shaded) and predicted sand fluxes (black line) at Nili and Meroe Paterae from global and domain-3 MarsWRF models.


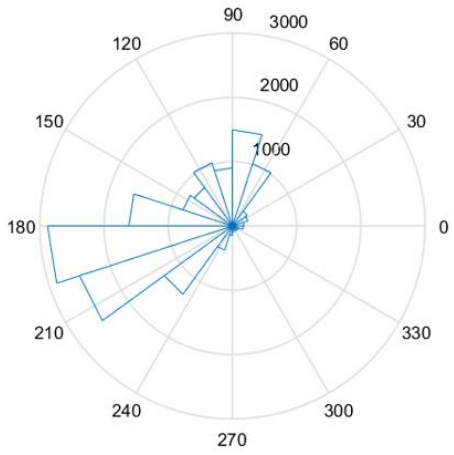

*Fig. 3.19:* Comparison of dune orientations at Nili Patera to directions of predicted sand flux at Nili Patera.

Under the simplified *Ayoub et al.* (2014) parameterization of sand transport as a function of input, uncorrected winds from MarsWRF predictions, the model fit to observations at Nili is worse, as the early-season peak in sand flux exceeds the late-season peak in magnitude (Fig. 3.20). This differs from the finding of *Ayoub et al*. (2014) in that earlier MarsWRF results matched well to the observed seasonal sand flux, for reasons we discuss below. The overall magnitudes of predicted sand flux are also lower, with a yearly average of ~1.5 $m^2$/Earth yr., which is less than ¼ of the average whole-dune sand fluxes measured at Nili and Meroe Patera.

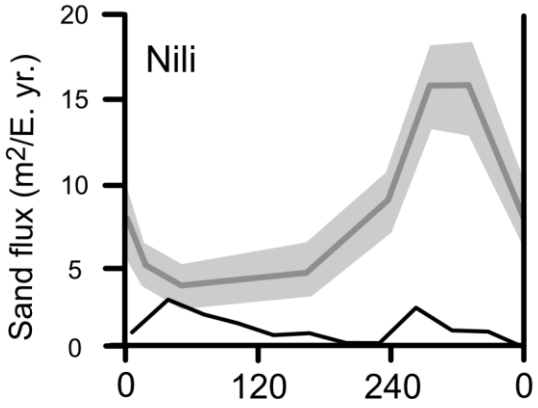


*Fig. 3.20:* Sand flux predicted from the MarsWRF global simulation at Nili Patera, following the method of *Ayoub et al.* (2014), with one effective transport threshold (set equal to the threshold found to best fit observed sand fluxes at Nili Patera by *Ayoub et*

*al.* (2014), and no imposed variability on wind predictions from MarsWRF. The observed pattern of seasonal change in the sand flux is indicated by the gray line with shading; it is rescaled to match the average translation flux observed in association with whole-dune motion.

## 3.4 Discussion

### 3.4.1 Whole dune and ripple sand-flux comparison - implication for ripple interpretation

Comparison of ripple to whole-dune sand flux (Fig. 3.15) reveals variability in the ratio between the two. Regardless of our choice of a low or high RI, most sites show a dune-to-ripple flux ratio in excess of the 5:1 ratio for ripple and dune fluxes as measured at crestlines. The observed trend towards relatively higher dune-to-ripple flux ratios may reflect greater along-crest transport in ripples further from dune crestlines; in particular, the long linear ripples observed on the sloped sides of Martian dunes with crests oriented parallel to the downslope direction may be experiencing some downslope sand transport [*Liu & Zimbelman*, 2015]; this component of movement is convolved with aeolian versus gravity driven mobility and we do not attempt to deconvolve them. However, as stated previously in the Methods section, these missing fluxes are likely minimal.

### 3.4.2 Long term evolution of the dune field

Our observations of spatial variation in whole-dune sand flux at Nili and Meroe Paterae show clear patterns of variation in flux for ripples but not for dunes (Figs. 3.16, 3.17). In particular, the decrease in ripple flux towards more downwind portions of Martian dune fields is much less clear in whole-dune flux measurements. A decrease in flux away from the upwind margin of the dune field suggests disruption of the wind field due to the topography of the dunes; it is not clear, however, why this disruption might preferentially affect the ripple flux over the whole-dune flux.

One possibility is that the individual dunes are not migrating across the surface in steady state, but are instead growing, shrinking, and/or changing in shape due to transfers of sand between individual dunes. These interactions might include leakage of sand from the horns of barchan dunes to dunes further downwind, or transfer of sand between colliding dunes. We might generally expect this sand transfer, if present, to lead to an additional sand flux that is lost from the dunes on the upwind margin of the dune field and added to the dunes further downwind. This flux, if it generally decreases strongly in the downwind direction, might bring the observed mismatch between the patterns of spatial variation in the ripple and dune fluxes into agreement; the most-upwind dunes would have the highest sand fluxes, better following the pattern of spatial variation in ripple flux.

This pattern of interior flux decrease would also have implications for the long-term evolution of the dune field; if the dune field is assumed to migrate westward en masse through time, its rate of migration could be faster than that calculated for individual dunes, given the gradual decay of dunes at the field's upwind edge. This

scenario is not implausible given the lack of any observable protodunes at the upwind margins of Nili and Meroe Patera; the barchans at the edge of these dune fields may be mature dunes because they were once in the dune field's interior, and have been exposed to the upwind edge by decay of the dunes upwind of them.

An alternative view could be considered if this pattern of westward flux decrease occurs over a regional scale beyond that of the dune field itself. Mesoscale model simulations suggest this possibility; in particular, east of Nili and Meroe strong daytime slope flows associated with the broad east-to-west increase in elevation across Syrtis Major are expected to dominate the wind regime. These winds are enhanced in northern winter, when the regional Hadley-cell circulation comes approximately from the north, but are suppressed by a southerly Hadley circulation in northern summer.

However, near the sites of the Nili and Meroe Patera dune fields, winds and sand fluxes are predicted to decrease; this may reflect the topography associated with the volcanic calderas at Nili and Meroe acting as a local windbreak. This spatial pattern of wind variation could be the critical factor responsible for the Nili and Meroe Patera dune fields' existence; the dune fields may form at the location where these slope winds decay enough to permit sand to accumulate into bedforms. In this scenario, the dune field would not migrate en masse through time.

### 3.4.3 On the use of ripple migration measurements to constrain the wind regime and validate GCM simulations

To first order, our measurements suggest that MarsWRF simulations of the Martian atmosphere in the Nili/Meroe region are reasonably realistic, given their reproduction of the increase in sand flux after Ls = 240 degrees. Dynamically, these changes in sand flux are largely produced by three interacting circulation components: the global-scale overturning circulation (Hadley cell or cells), which varies seasonally; slope winds associated with both regional-scale topography in the broader Syrtis Major region and the local-scale topography of the caldera; and tidally-driven flows. As shown in Fig 3.21, panels (a) and (c), which show mass streamfunctions in the global MarsWRF domain at both equinoxes and solstices, around equinox Mars has two Hadley cells with rising motion near the equator and descending motion at mid-latitudes in both hemispheres. This results in a near-surface 'return flow' towards the equator in both hemispheres: northerlies (winds from the north) in the north and southerlies in the south (although the equinoctial circulation is asymmetric, with the northern hemisphere cell being stronger and its upwelling branch slightly south of the equator, meaning that northerlies also extend to southern low latitudes). At the latitude of the Nili and Meroe Patera dunes, northerly winds associated with the global overturning circulation would therefore be expected at both equinoxes. As shown in Figure S1, panels (b) and (d), however, Mars has a single Hadley cell around solstice, with rising motion in the summer hemisphere and descending motion in the winter hemisphere. During northern summer, this results in a return flow from south to north across the equator, hence southerlies at the latitude of the dune fields (Figure S1 b), whereas in southern summer, when the Hadley circulation is also at its strongest by far [*Richardson & Wilson*, 2001],

the return flow is from north to south across the equator hence producing northerlies at the latitude of the dunes (Figure S1 d). We note here that the Hadley cells, especially at solstice, are narrower in their latitudinal extent than typically shown elsewhere [e.g. *Toigo et al*., 2012]; this is due to the relatively low model top used in these MarsWRF simulations to ensure numerical stability in the high-resolution domains, which results in the top of the Hadley cells and some tidally-generated waves being cut off by the model top (especially in southern summer), which in turn prevents the cells from expanding to higher latitudes [e.g. *Wilson & Hamilton*, 1996]. This may be addressed in future work by running MarsWRF as a standalone mesoscale model (with a relatively low top layer height) forced by output from a separate global model with the top layer centered above 80km.

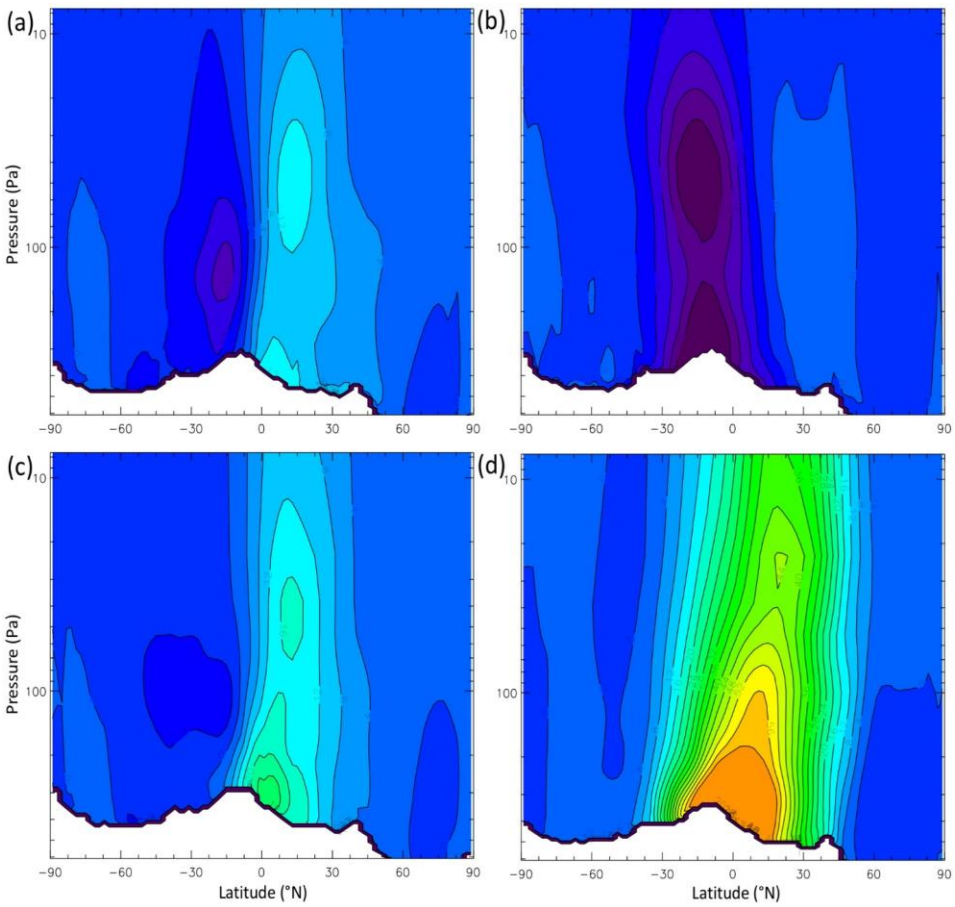

*Fig. 3.21:* Mass streamfunctions from the MarsWRF global forecasting model, Contours are in units of $10^8$ kg/s, with positive values indicating clockwise circulation and negative values indicating anticlockwise circulation. Panels: a) Ls=0°, b) Ls=90°, c) Ls=180°, d) Ls=270°.

On top of these background global-scale flows are complex regional and local flows associated with thermal tides and topography. These are best demonstrated by animations of modeled near-surface winds at the equinoxes and solstices in domain 2 of the MarsWRF nested simulation (Supplementary Material Movies S2-S5). While Nili and Meroe Patera are depressions, they sit an on elevated terrain that rises up from the western slopes of the huge Isidis impact basin along the hemispheric topography dichotomy boundary. Daytime upslope flows associated with these large-scale slopes result in a strong daytime easterly (or east-northeasterly) wind component to the east of the caldera (see e.g. 14:30 in all movies), although this flow is turned more to the north by the Hadley cell return flow at Ls=90° (Movie S3) and further to the south by the Hadley cell return flow at Ls=270° (Movie S5). However, there are also strong daytime upslope flows inside the Nili and Meroe caldera, which tend to oppose the large-scale slope flows on their eastern slopes. Hence overall, the large-scale regional flows only reach the dune fields in some seasons and for some times of the day. An example of this can be seen in the late afternoon (e.g. 16:30 and 17:30) at Ls=270° (Movie S5), when strong regional easterly slope winds and the very strong northerly Hadley cell return flow combine to produce strong north-easterlies that do flow over both dune fields. This explains the model prediction of peak sand fluxes in this season and the match to the observed sand transport direction and may seem rather obvious at first glance.

However, if we examine the flows over the dune fields in more detail, in animations of near-surface winds from domain 3 of these simulations (Supplementary Material Movies S6-S9), we can see that this result is actually quite marginal. Considering the afternoon and evening at Ls=270° (Movie S9), we see that strong winds associated with the local caldera topography oppose the incoming north-easterly winds, preventing them from reaching the dune fields (marked with crosses) at some times. At 16:30, for example, upslope winds inside Nili Patera's caldera prevent the incoming regional flows from reaching the dunes (marked with an orange cross).

Finally, we note that nighttime downslope flows on the large-scale slopes are restricted,at least in the simulations,to closer to Isidis basin. Thus at night, winds at the dune fields are controlled more by the local-scale topography, with downslope winds into the caldera dominating. The wind patterns at these dune fields are thus a complex combination of these global, regional, and local-scale flows, making the results very sensitive to small differences in model setup that impact the strength of each circulation component and hence detailed predictions in regions such as Nili and Meroe Patera.

It is important for us to consider the possibility that the parameters we use to predict sand fluxes from Martian GCMs affect not only the magnitudes of predicted flux, but also the pattern of seasonal variation in the model. We have performed sensitivity tests to evaluate the impact of varying these model parameters on the pattern of seasonal variation; the degree of variation that can be generated is far less than that in the absolute magnitudes of sand flux, but is nonetheless significant. The most important parameter for our model is the fluid threshold, which is the shear velocity needed to

initiate sand transport. In general, increasing the fluid threshold primarily decreases our predicted sand fluxes, but it also makes our sand flux predictions more dependent on the few highest wind predictions made by the GCM, rather than the overall distribution of wind speeds.

We can see this effect by examining the early-season peak in sand flux predicted from global domain outputs by our model at Nili (Fig. 3.22, upper panel). Quadrupling assumed fluid threshold shear stresses greatly decreases sand flux predictions overall, but increases the magnitude of the early-season peak relative to that of the late-season peak. This is because the early-season peak in sand flux is driven largely by a relatively brief period of higher velocity winds (Fig. 3.22). These winds have outsized importance in our sand flux model, particularly when we set a high fluid threshold. When our fluid thresholds are high (shear velocities >1 m/s, shear stresses >0.01 Pa), the shear velocities predicted by the GCM never exceed the fluid threshold, so sand transport is only predicted to happen thanks to our imposed Weibull wind-variability scheme. The few wind predictions closest to the threshold largely determine the predicted sand flux in this case, since the fluid threshold is exceeded much more frequently as mean winds approach the fluid threshold.

A similar effect can be generated by adjusting the value of the Weibull shape parameter, *k* (Fig. 3.22, lower panel). Lower values of *k* (closer to 1) correspond to a more variable predicted wind regime, while higher values of *k* correspond to a more Gaussian probability distribution of winds, with a reduced “tail” of higher velocity wind speeds. When the fluid threshold is high, such that the modeled winds never actually

reach the fluid threshold, lowering the *k* parameter increases the predicted sand transport, since higher variability causes more frequent occurrences of higher winds which exceed the fluid threshold. However, when the model-predicted winds are already in excess of the fluid threshold, higher variability actually *reduces* the predicted sand fluxes, as winds are predicted to fluctuate to lower speeds below the fluid threshold more frequently. At Nili and Meroe, the latter scenario predominates; higher *k* is associated with higher overall sand fluxes, although the effect of *k* on the predicted flux is minor.

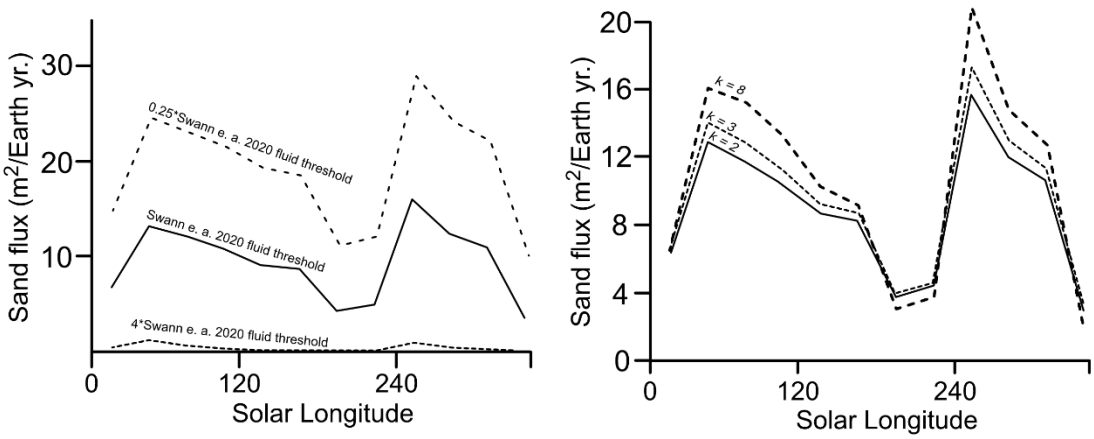


*Fig. 3.22:* Comparison of modeled sand fluxes for various choices of the fluid threshold (left panel) and various choices of the Weibull shape parameter (right panel). Left panel: Bottom (solid) line – Fluid threshold calculated using expressions in *Swann et al.*, 2020. Middle dashed line – Fluid threshold calculated using expressions in *Swann et al.*, 2020, and then divided by 4. Top dashed line – As for the middle dashed line, except that the fluid threshold is multiplied by 4 instead. Right panel: Bottom (solid) line – Sand fluxes calculated assuming a wind distribution with a Weibull shape parameter of 2 (relatively

higher variability in wind). Middle (dashed) line – Uses a Weibull shape parameter of 3 (medium variability in wind). Upper (dashed) line – Uses a Weibull shape parameter of 4 (low variability in wind).

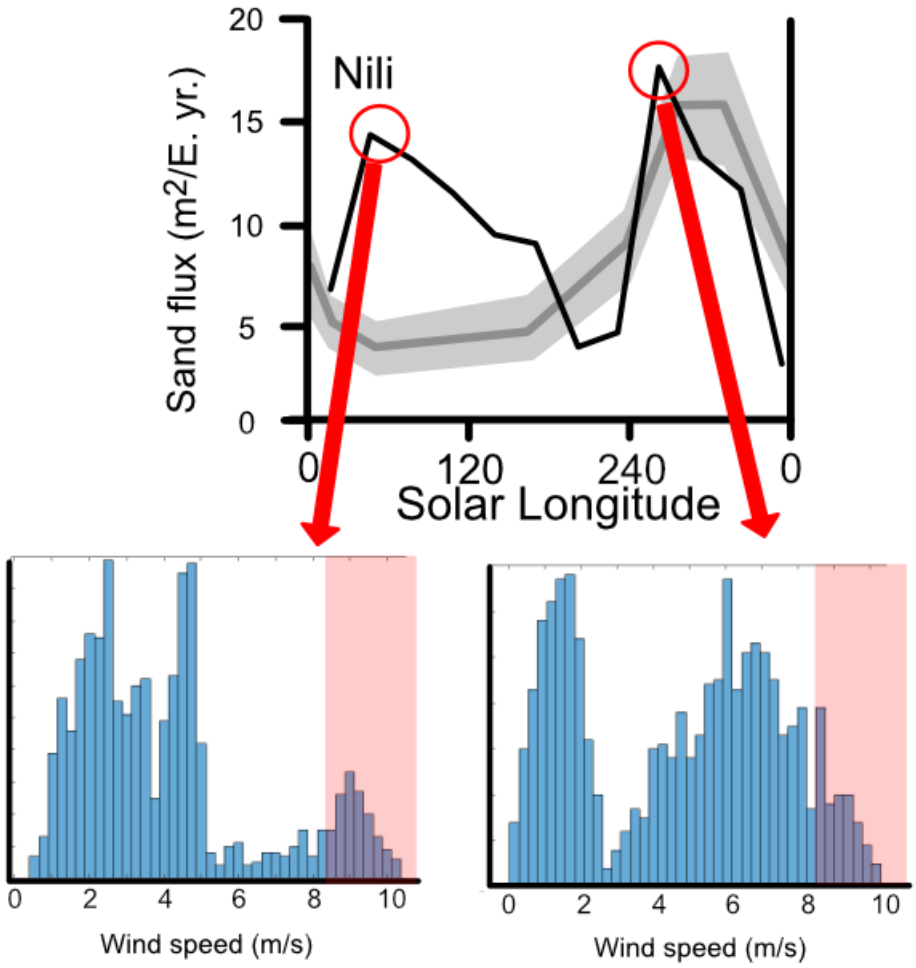


*Fig. 3.23:* Top panel – Comparison of sand fluxes predicted from MarsWRF winds and our sand transport model to observations. Times of peak sand flux are highlighted, and the distribution of wind speeds predicted by MarsWRF at each of these times is shown in the histograms in the bottom panels. The right side of each histogram is highlighted to emphasize the higher-velocity wind predictions that are the primary control on our

predicted sand flux; these are similarly frequent at both peaks, even though the overall wind distribution is shifted towards higher winds in the late season peak.

We emphasize that we cannot ultimately eliminate either the early or late season peaks entirely by varying values for these parameters – changing the fluid threshold does not change the fact that atmospheric models predict more strong winds at the times corresponding to both peaks in the sand flux. Playing with these parameters can make some peaks higher or lower relative to others, however. Ultimately, creating an optimal modeling scheme which weights the contributions to sand flux from winds of differing magnitudes appropriately will almost certainly require coupled observations of wind speed and sand flux on the Martian surface, given the conflicting results from past terrestrial wind-tunnel studies.

For our analysis, we consider only the *Kok* (2010b) impact threshold estimation and sand flux laws (the other threshold, the fluid threshold to initiate sand motion, is varied as in Fig. 3.22), and the simpler *Ayoub et al.* (2014) method to calculate sand fluxes, and do not consider any alternative sand transport laws. Using other sand transport laws would likely change the magnitudes of our predicted fluxes, but would change the seasonal pattern little, as all sand transport laws predict higher fluxes as winds increase. There is already great uncertainty in the magnitudes of our predicted sand fluxes anyways, due to the aforementioned uncertainty in the fluid threshold and other parameters input to the models. Some transport laws might also weight the contributions from the rarest, highest-velocity predicted wind events more heavily relative to other transport laws, but we can alter these weightings anyways by

modifying the assumed Weibull *k* parameter and fluid threshold, among other parameters.

Our results support the existence of relatively low (shear stresses on the order of ~$10^{-3}$ Pa, implying shear velocities of ~0.6-0.8 m/s) fluid thresholds for sand motion on Mars, similar to those supported in recent studies [e g., *Musiolik et al.,* 2018; *Swann et al.*, 2020] over the higher fluid thresholds predicted by earlier studies [e. g., *Greeley et al.*, 1980; *Iversen & White*, 1982; *Shao & Lu*, 2000]. Plugging the higher threshold shear velocities (of ~2 m/s, equivalent to shear stresses of ~$10^{-2}$ - $10^{-1}$ Pa) into our models leads to sand flux estimates that are orders of magnitude lower than our observations; in this case, we would need to assume a systematic underprediction of winds by global forecasting models and/or massive errors in the sand flux parameterization. The winds at Nili and Meroe would also need to be much higher than those observed in situ by the TWINS instrument on the InSight lander [*Banfield et* al., 2019] and the REMS instrument on the Curiosity rover [*Gómez-Elvira,* 2012].

The results of the current MarsWRF model fit our measured sand transports a bit less well than previous iterations of the model presented in the literature [e g., *Ayoub et al.*, 2014]. That earlier publication used output from a version of MarsWRF that had a small error in its radiative transfer scheme that, when corrected, resulted in slightly modified surface wind patterns in this region. In addition, MarsWRF has been improved since that publication to use more realistic prescribed atmospheric dust distributions, which for these simulations was based on Mars Global Surveyor Thermal Emission Spectrometer (TES) limb and nadir dust measurements [*Smith et al.*, 2000].These

changes have had complicated effects on the model behavior in this region, which are still being studied; however, the basic picture of interplay between the Martian Hadley cell and regional slope winds remains unchanged.

## 3.5 Conclusions

Analysis of a long timeseries of imagery from the HiRISE camera reveals a pattern of seasonal variation in sand flux at Nili Patera that is consistent from year to year with higher fluxes in northern hemisphere fall and winter and lower fluxes in northern hemisphere spring and summer. At Meroe Patera, a similar pattern of seasonal variation in flux is apparent, implying that the local sand transport is driven by a regional wind coming from the northeast of the Nili and Meroe study sites, which is strongest in northern hemisphere autumn and winter. Our results are compatible with the model of meter-scale Martian ripples as enlarged impact ripples driven by reptating sand grains.

Our observations agree to first order with predictions of seasonal changes in the wind regime made by MarsWRF atmospheric model simulations. Output from a global-scale model produces a secondary peak in sand flux early in the Martian year which does not match observations. Finer (domain 3) scale simulations eliminate the early-season flux peaks, but also cut off increased sand fluxes too early in Martian autumn and winter. Detailed examination of model predictions shows that the flow over Nili and Meroe is controlled by a complex combination of global, regional, and local-scale flows, thus predictions of sand fluxes are very sensitive to small changes in model set-up or physics that impact the relative strength of these circulation. Due to uncertainties in the values of various input parameters for our sand flux calculations, the absolute

magnitudes of sand fluxes expected from atmospheric model simulations on Mars are highly uncertain, though lower values of the fluid threshold permit a better fit to observations than higher values. The pattern of seasonal variation in the sand flux is less sensitive to alteration of these model parameters, providing a constraint which models can be evaluated against. The utility of our technique could be improved by a better understanding of conditions and parameters governing Martian sand transport, most importantly the fluid threshold. Ground-based, short-timescale observations of Martian sand transport events coupled with real-time wind measurements could greatly improve our understanding of these parameters, and enable remotely acquired sand motion measurements to be used as a tighter constraint on atmospheric models.

# 4. Craters as sand traps: Dynamics, History, and Morphology of Modern Sand Transport in an Active Martian Dune Field

Roback, K. P.[1], Runyon, K. D.[2], and Avouac, J. P.[1]

[1] – California Institute of Technology, Division of Geological and Planetary Sciences

[2] – Johns Hopkins University Applied Physics Laboratory

**Abstract**

Aeolian transport of sand is abundant on modern-day Mars, as revealed by remote sensing measurements of the motion of dunes, and of the meter-scale ripples that mantle them. We study a large-scale natural sand trap within the Meroe Patera dune field: a 1.8-km diameter crater which features a dune-free "shadow" in its lee. We compare the volume of sand trapped within this crater to the sand volume that would be expected to cover the area of the crater and its dune-free shadow behind it if the crater were not present. We find that the crater holds less sand than this "missing" volume would predict, implying that sand escapes from the crater over time. Modern day imagery shows an apparent lack of sand escaping from the Meroe crater, however, suggesting that changes in the wind regime at the site may have allowed sand to escape in the past. The persistence of an altered dune morphology all the way to the far downwind edge of the dune field suggests consistent wind conditions over the time of the crater-dune field interaction.

## 4.1 Introduction

Dune fields are common features on Mars [e.g., *Hayward et al.,* 2014], and active sand transport has been observed at many different locations [*Banks et al*., 2018; *Chojnacki et al.,* 2019; *Silvestro et al.,* 2010*, Bridges et al.,* 2012*, Ayoub et al.,* 2014*, Runyon et al.,* 2017a,b]. Cycles of aeolian erosion and deposition appear to be a dominant mechanism driving landscape evolution on modern-day Mars [e.g., *Runyon et al*., 2017b].

Windblown sand moves in varying modes [e.g., *Anderson*, 1987]; while saltation on Mars is energetic with long hop lengths, other grains move via the slower and less-energetic processes of reptation and creep [*Andreotti,* 2004; *Almeida et al.,* 2008; *Sullivan & Kok*, 2017]. As a result of these varying energy levels, bedforms of different scales express different fluxes of sand grains; an example of this appears in the comparison of sand fluxes measured at ripples to the sand fluxes measured from motion of whole dunes; the much lower ripple fluxes largely represent only the portion of sand grains moving in reptation and creep [*Bridges et al.,* 2012*, Ayoub et al.,* 2014; *Lapotre et al*., 2018].

Accurate estimates of total sand flux are crucial for understanding the depositional and erosional geologic histories of various parts of the planet, yet no direct flux measurement on Mars using in situ sand traps has ever occurred. For the first time, we use an intra-dune field impact crater as a natural sand trap to further explore the dynamics of sand transport on the Martian surface.

## 4.2 Study site

### 4.2.1 Setting and morphology of the Meroe dune field

We focus on the Meroe Patera dune field, an actively migrating barchan dune field and downwind sand sheet located north of the Martian equator in the Syrtis Major region at 7.16 N, 67.75 E (Fig. 4.1). The field is located in the midst of a largely flat plain 36 km from the Meroe Patera caldera. The region has been mapped as an early Hesperian volcanic unit densely crossed by tectonic lobate scarps [*Tanaka et al.,* 2014].

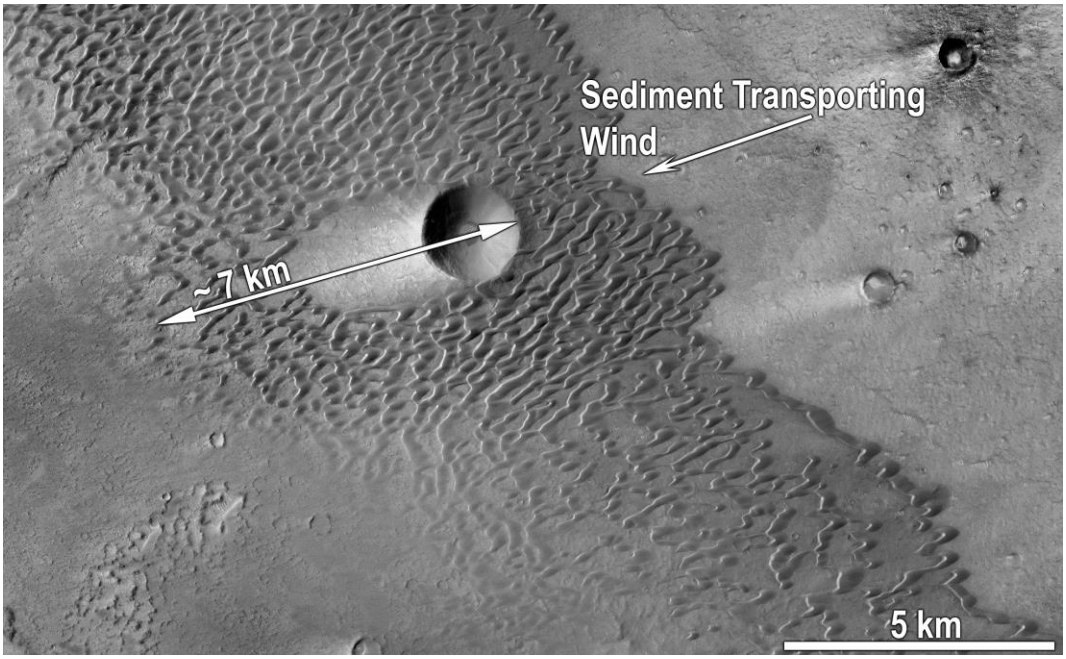


*Fig. 4.1:* CTX imagery of the Meroe Patera barchan dune field, annotated to indicate the dominant wind direction implied by the barchans' morphology. Image Credit: NASA/JPL/MSSS.

The dune field is dominated morphologically by barchan dunes, and barchanoid ridges formed by merging barchan dunes. The primary slipface orientation is towards

the west-southwest. The southerly horns of the barchans are consistently extended relative to the northern horns, suggesting the influence of a secondary wind regime oriented in a more southerly direction than the net sand transport direction indicated by the barchans' overall geometry; the dunes are in the "fingering mode" of *Courrech du Pont et al.,* 2014.

### 4.2.2 Crater-Dune Field Relationship

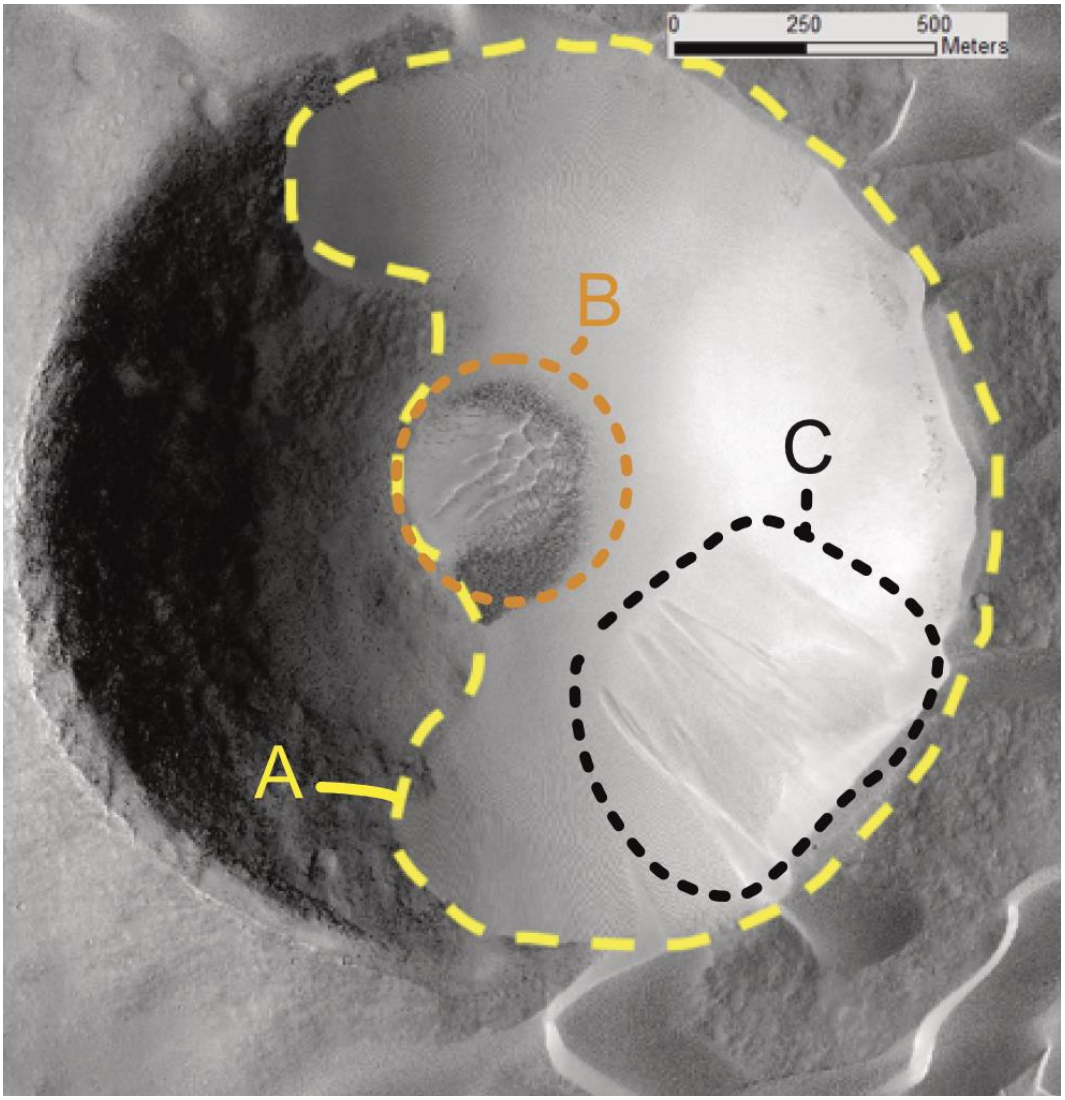

*Fig. 4.2:* HiRISE image ESP_050939_1875 of Nathan's Crater, annotated to highlight relevant features. A) Outline of the sand-covered portion of Nathan's Crater. B) Area of transverse aeolian ridges on the sand-covered floor of Nathan's Crater. C) Visible grainfalls illustrating modern infill of aeolian sand to Nathan's Crater. HiRISE image credit: NASA/JPL/University of Arizona.

Within the Meroe Patera dune field, a 1.8 km-diameter, 350 m deep impact crater serves as our natural sand trap (Fig. 4.2). We have unofficially nicknamed it Nathan's Crater, after our late collaborator Nathan Bridges who inspired much of the present work. A dune-free shadow stretches ~2.6 km downwind of the crater's rim (Fig. 4.1). HiRISE imagery of the crater itself reveals a large quantity of sand trapped within the crater, with more actively entering over the crater's upwind, eastern rim (Fig. 4.2). No surficial crater ejecta is observed anywhere around the crater, and on the downwind (western) side of the crater, only exposed bedrock is apparent. No large sand sheets or dunes appear to be exiting from the crater. The crater thus appears to act as a sand trap.

The shape and the length (~2.6 km) of the dune-free shadow could suggest that the crater postdates the dune field. In other words, the impact could have punched into the dune field; in this model the dune-free shadow would open and lengthen over time as the dunes which survived the impact on its downwind side migrated away from the crater. We do not favor this interpretation, given the apparent absence of a fresh ejecta facies surrounding the crater, the presence of many superimposed meter-scale craters

near and within Nathan's Crater (Fig. 4.3), and the very low likelihood that the dune field would have survived the creation of a ~2-km diameter crater.

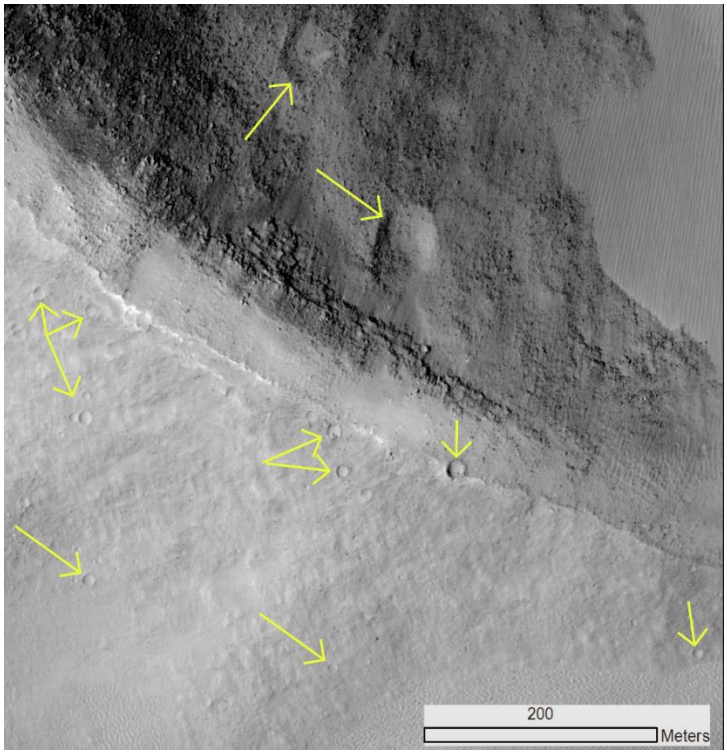


*Fig. 4.3:* HiRISE imagery of the southwest part of the crater rim, with some superposed younger craters indicated by arrows. There is also a general lack of ejecta around this crater, indicating its relatively old age. HiRISE image credit: NASA/JPL/University of Arizona.

Some basic crater statistics performed <500 m from the crater rim finds densities of ≥20 m diameter craters on the order of 100/km$^2$; this supports a surface age, given current Martian isochrons [*Hartmann*, 2017] on the order of 100 Ma or greater (Fig. 4.4), far too old to postdate the dune field's likely arrival. We therefore conclude that the crater was already present when the leading (downwind) edge of the dune field

arrived at its location, assuming the dune field is migrating *en masse* (Fig. 4.5). The downwind edge of the dune field is ~7 km downwind of Nathan's Crater, but a sand sheet extends beyond the dunes to ~13 km downwind.

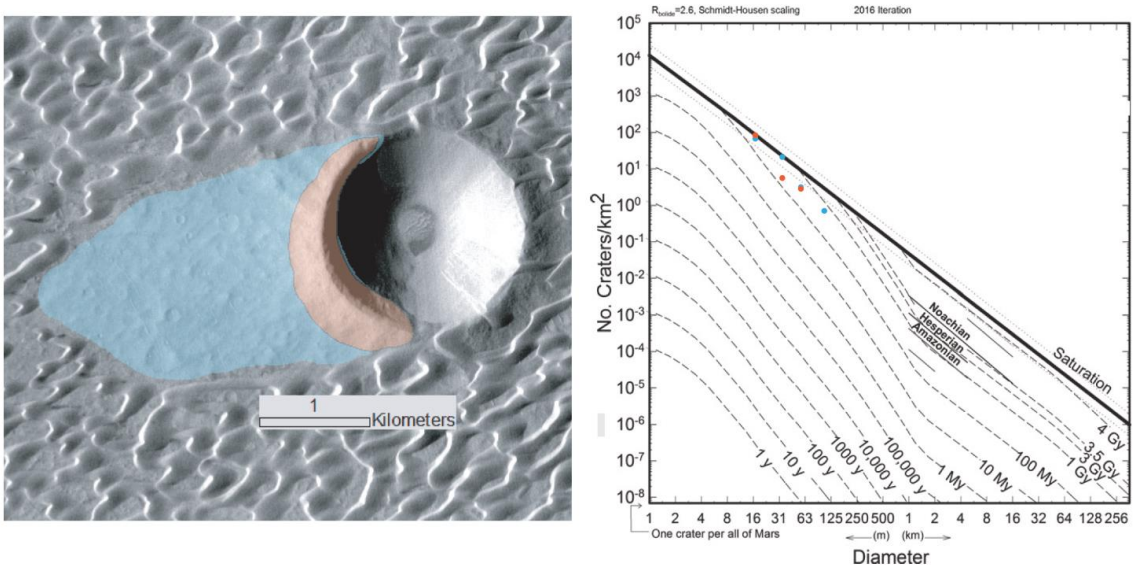


*Fig. 4.4:* Left – Indication of large (light blue shading) and small (orange shading) crater-counting areas. Right - actual crater counts associated with both overlaid on Mars isochrons [from *Hartmann & Daubar*, 2017] Given the small area, the point here is not to determine a precise age for the surface, but to show that a young age on the order of <1 Ma is implausible. CTX base image credit: NASA/JPL/MSSS.

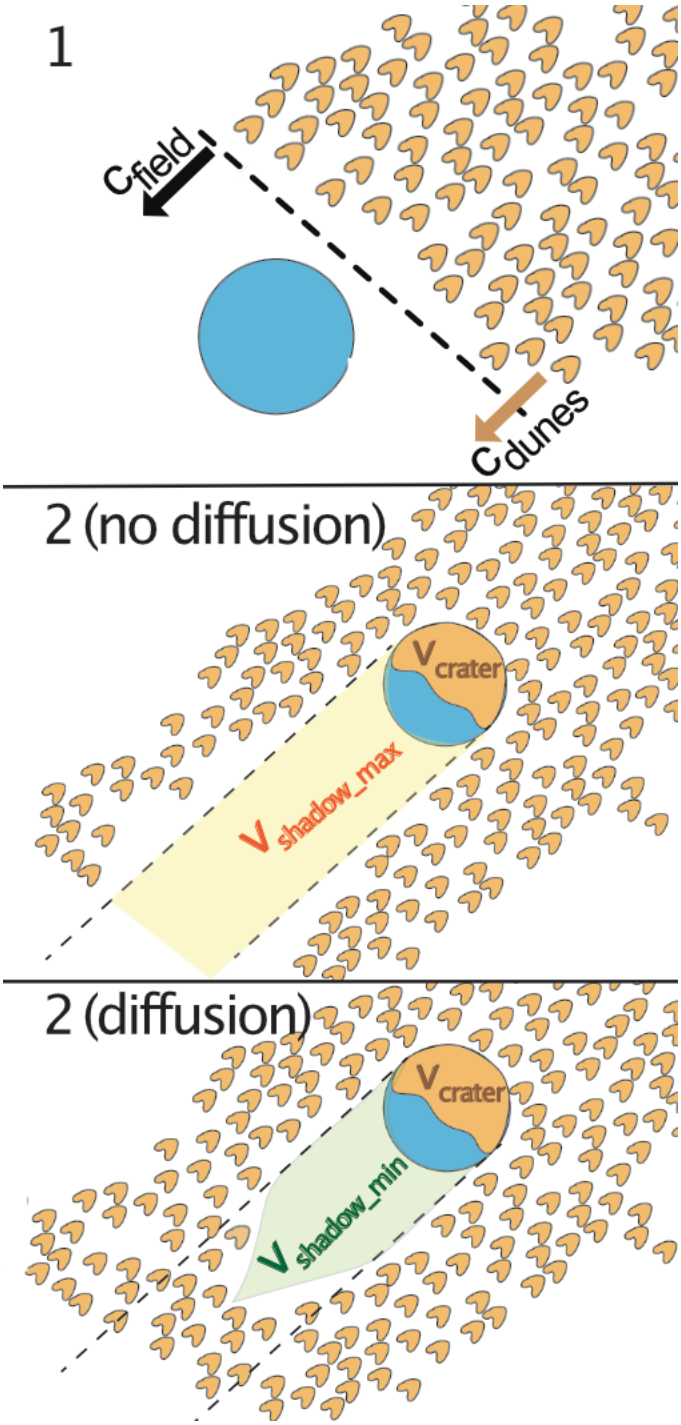


*Fig. 4.5:* Cartoon model for the history of crater-dune field interaction at Meroe Patera.

The dune field advances in the direction indicated by the black arrows (panel 1) and

reaches the crater (2). We illustrate scenarios for the dune field's morphologic evolution in which lateral spreading of sand does/does not occur.

We estimate the volume of sand $v_{crater}$ trapped within this crater, and compare it to the volume $v_{shadow\_min}$ of sand that we would expect to be present if the crater and its dune-free shadow did not exist (Fig. 4.5), and were instead covered with dunes of the same spatial density and morphology as those that exist elsewhere in the dune field. Comparing these volumes reveals the crater's effectiveness as a sand trap to integrate past sand fluxes and possibly records the presence of earlier dune fields. If the volume of trapped sand $v_{crater}$ is significantly greater than the volume of missing sand $v_{shadow\_min}$, this could imply trapping of a population of sand grains which avoid being trapped in dune slipfaces, but cannot avoid trapping by Nathan's Crater. These grains would need to move in long hops to avoid trapping in dune slipfaces, and might particularly include any grains traveling in suspension. Alternatively, this could indicate the presence of a "leftover" volume of sand from earlier generations of dune fields which passed by the crater.

If $v_{crater} < v_{shadow\_min}$, this would imply that the crater has not been a completely effective sand trap over long timescales, and that a significant fraction of the sand that passed the crater escaped downwind or never entered it. The volume of sand in the crater can also be compared to the total volume of sand ($v_{shadow\_max}$) that should have accumulated from the dunes falling into the crater since the leading edge of the dune field first reached it. This total volume of sand can be estimated by projecting the crater diameter to the far downwind edge of the dune field, and estimating the volume of sand

($v_{shadow\_max}$) that would be expected to cover this area if its sand supply had not been disrupted by the crater's presence. $v_{shadow\_max}$ can alternatively be calculated by using modern dune migration rates and morphology to estimate a long-term bulk sand flux into Nathan's Crater; this can be multiplied by the length of time the dune field has been present at the crater assuming steady *en masse* migration of the dune field to derive an estimate of the total input volume $v_{shadow\_max}$. This input volume neglects the possibility that the dune field's migration rate $c_{field}$ is different from the migration rate of individual dunes, $c_{dunes}$.

If $c_{field} < c_{dunes}$, this would imply that dunes should form at the dune field's upwind edge, and that at the downwind margin of the dune field, dunes should decay out of existence as they migrate. In this scenario, the timescale of crater-dune field interaction could be much longer than assumed, causing the longterm input sand flux to Nathan's Crater to be much higher. Alternatively, if $c_{field} > c_{dunes}$, we would expect dunes at the upwind margin to be steadily decaying through time, losing sand through barchan horns to be organized into dunes further downwind.

Our current timeseries of HiRISE images at Meroe Patera is insufficient to provide a strong argument in favor of any of these particular dynamical scenarios, although the lack of visible protodunes on the Meroe dunefield's upwind edge does suggest that the $c_{field} < c_{dunes}$ scenario is unlikely. The smaller, less well developed dunes on the dune field's downwind edge might be interpreted as either decaying dunes or developing protodunes. Longer timeseries of imagery at Meroe would likely reveal

upwind dune formation or shrinkage, enabling this distinction to be better resolved in later studies.

## 4.3 Measurements

### 4.3.1 Dune Motion Measurement

We measured the migration rate $\mathbf{c_{dunes}}$ of the dunes by tracking the changing positions of dune slipfaces relative to bedrock in timeseries of co-registered and orthorectified high resolution (0.25-0.5 m/pixel) orbital High Resolution Imaging Science Experiment [HiRISE*; McEwen et al*., 2007] images. We processed the images in the ENVI plug-in Co-registration of Optically Sensed Images and Correlation [COSI-Corr; *Leprince et al.,* 2007]. We multiplied the migration rate of each individual dune with its average height, equivalent to the moving sand thickness, to estimate sand flux associated with whole-dune migration (Fig. 4.6). This flux estimate is an estimate of the translation flux associated to moving bedforms, and neglects sand exchanges between dunes which may contribute to an additional flux, often referred to as the deformation flux [*McElroy & Mohrig*, 2009]. Depending on the setting, the deformation flux may be small relative to the translation flux, or be similar in magnitude to the translation flux, but it cannot be constrained from current satellite measurements. This flux could be estimated if measurements of dune volume taken at two different times can be made, as changes in dune shape would reveal a deformation flux. However, transfers of sand between bedforms that result in no net shape or volume change might still be neglected.

We used a 1-m post-spacing three-dimensional HiRISE digital elevation model (DEM) generated from images ESP_050939_1875 and ESP_051084_1875. Using HiRISE images, we mapped out sand-covered and sand-free parts of the Meroe Patera dune field, and extracted elevations from the DEM over sand-free areas. We projected the bedrock surface under the dunes to generate an interpolated continuous bedrock surface, which we subtracted from the DEM. This subtraction of bedrock topography from total topography allowed an accurate estimate of dune volume in order to represent it as an equivalent sand thickness everywhere in the dune field (Fig. 4.6).

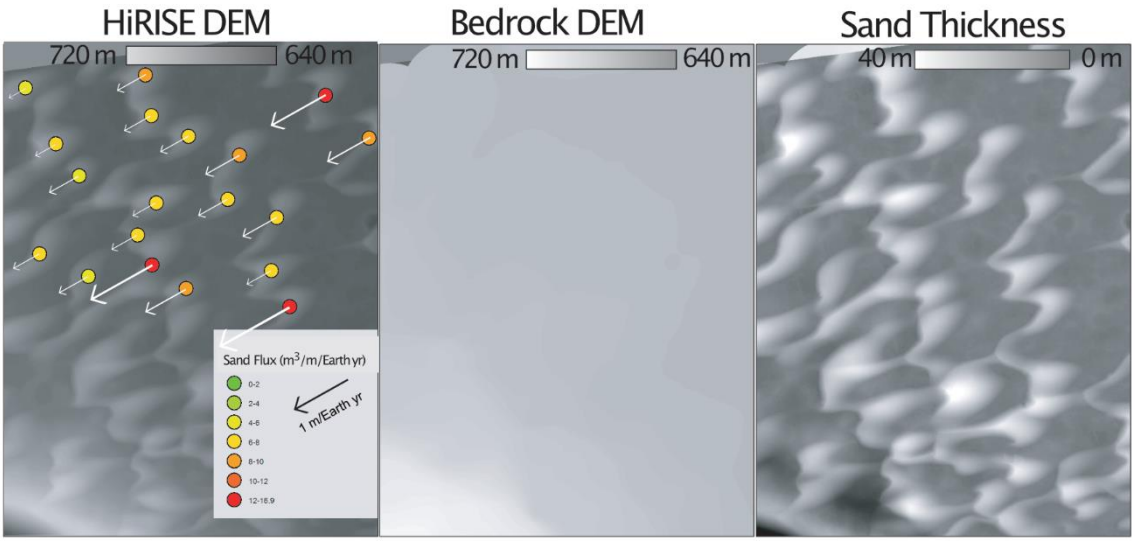


*Fig. 4.6:* Left panel – HiRISE DEM generated of the Meroe Patera dune field from HiRISE images ESP_050939_1875 and ESP_051084_1875. Dunes on which sand fluxes were measured are indicated by colored points, with attached vector arrows to indicate magnitudes of sand flux. Middle panel – DEM generated from applying a focal-statistics function to calculate the average bedrock surface height across the dune field. Right panel – DEM indicating sand thickness, generating by subtracting the dataset in the

middle panel from the dataset in the left panel. HiRISE image credit: NASA/JPL/University of Arizona.

### 4.3.2 Trapped Sand Volume Measurements

To estimate the volume of sand ($\mathbf{v_{crater}}$) trapped within Nathan's Crater, we use the same 1-m resolution HiRISE DEM described previously. We extract radial wall profiles extending outwards in all directions from the center of the crater, covering the sand-covered and sand-limited parts of the crater's walls. We then average wall profiles extracted over sand-covered and sand-free areas to derive an average representative profile for each part of the crater (sand-covered and sand-limited) (Fig. 8). We compare these profiles to derive an estimate of average sand thickness in the sand-covered portion of the crater, assuming an axisymmetric bedrock geometry under the sand.

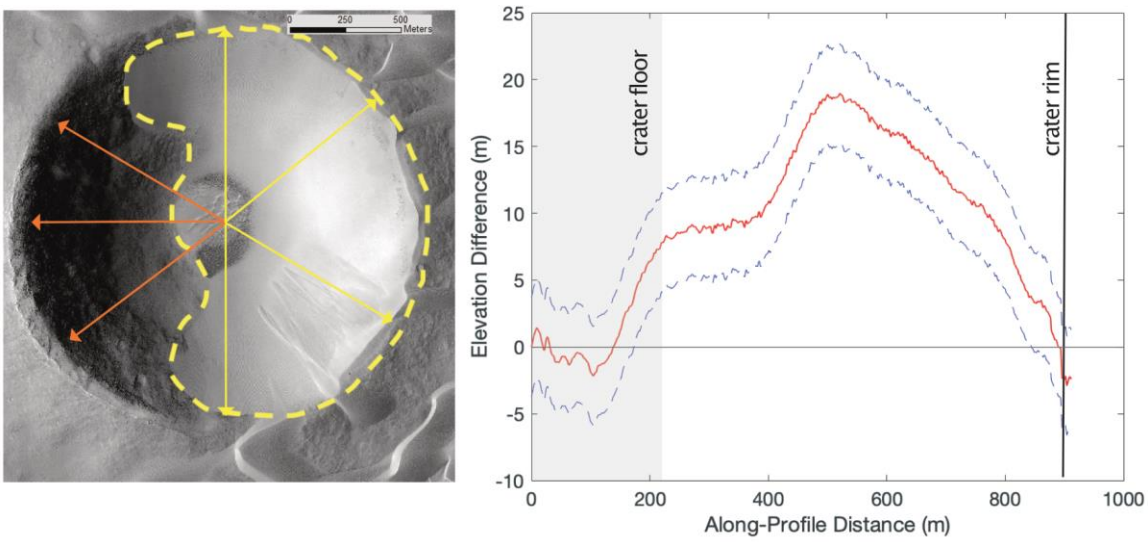


*Fig. 4.7:* Imagery of the Meroe Patera crater, with sand-covered areas outlined by a dashed line. Lighter (yellow) arrows indicate sample radial profile lines used in sand-covered areas to derive an average elevation profile for the sand-covered part of the

crater; darker (orange) arrows indicate the same for the largely sand-free part. Right: The difference in mean elevation between sand-covered and sand-free parts of the crater, as a function of along-profile distance. 1-sigma uncertainty on the measurement is indicated by the dashed lines. HiRISE base image credit: NASA/JPL/University of Arizona.

| HiRISE Stereo Pair – Image 1 | HiRISE Stereo Pair – Image 2 | Notes |
|---|---|---|
| ESP_012873_2045 | PSP_004052_2045 | Largest (>1 km diameter) crater in image |
| ESP_014011_1315 | ESP_014288_1315 | Raga Crater (only crater in image) |
| ESP_025901_2460 | ESP_026455_2460 | Only crater in image |
| ESP_027027_2325 | ESP_027370_2325 | Largest crater in image |
| ESP_035785_1840 | ESP_036062_1840 | Largest crater fully contained in image (~800 m diameter) |

*Table 4.1:* HiRISE stereo pairs, from which DEMs were made of sand-free craters used in our evaluation of uncertainty on our assumption of axisymmetric crater geometry. Notes on which craters were used are included. HiRISE image credit: NASA/JPL/University of Arizona.

We estimate the uncertainty on this measurement of sand depth and test our assumption of axisymmetric geometry by repeating this analysis for sand-free craters for which we have HiRISE DEM data available (Table 4.1). The apparent volume of trapped sand in these craters derived from our method should be zero within the measurement uncertainty. We extract radial wall profiles from these craters, and cut the craters in two halves. We then derive representative wall profiles for these sections and compare them, calculating the standard deviation of the along-profile elevation differences for each pair of representative profiles. For each crater, we rotate the choice of the two sections, and compare representative profiles for each, to account for possible variability in the profiles depending on which part of the crater is considered. While the sand-free craters we measure are not the same size as Nathan's Crater, their proportions are similar and all were simple craters with diameters on the scale of 1 km (Table 4.1).

Additionally, the floor of Nathan's crater, a flat area ~440 m in diameter, is covered with sand of an unknown thickness. This thickness is likely to be minimal (<10 m), given the observed shallowing of slopes near the bottom of the crater's mostly sand-free western wall. Nathan's Crater has a depth to diameter (d/D) ratio of 0.19, which is typical for unfilled simple craters [e. g., *Melosh*, 1989] and implies a degree of sand infill that is minimal in comparison to the crater's overall depth. We assume 1 m as a low bound, and 10 m as a high-end bound for the thickness of sand mantling the crater's flat floor.

By subtracting the measured crater topography from the expected bedrock topography, we find that the thickness of sand mantling the crater's walls is 11.2 m. We constrain a 2-sigma (95% confidence) uncertainty on this measurement, from our investigation of wall profiles of sand-free craters, of 6.5 m. The 2-sigma confidence interval is defined as the along-profile-averaged difference in elevation greater than or equal to that observed in 95 percent of tested pairs of halves of sand-free craters. By adding this sand volume to our maximum and minimum estimates of sand volume on the crater floor, we derive a volume of trapped sand ($\mathbf{v_{crater}}$) within Nathan's Crater of $7.52 \times 10^6 – 2.95 \times 10^7$ $m^3$.

### 4.4 Comparison with the 'missing' volume of sand in the crater shadow

Next, we estimate the volume of sand that we would expect to see covering the area of Nathan's Crater and its dune-free shadow if the crater were not present ($\boldsymbol{v_{shadow\_min}}$). This volume is a minimum estimate of $\boldsymbol{v_{shadow\_max}}$, the total volume of sand input to Nathan's Crater, given the likelihood that some sand has spread into the shadow from its sides. To derive this volume, we multiply the area of the crater and its shadow by a representative averaged sand thickness for the Meroe Patera dune field. We calculate this thickness using the previously described method from HiRISE DEM data. To assess possible variability in sand thickness on the kilometer-width scale of the crater and its dune-free shadow, we calculated averaged sand thicknesses in test windows of the same size and geometry as the crater and its shadow, placed on either side of the sand shadow.

The corresponding "missing" volume $v_{shadow\_min}$ from the crater's dune-free shadow is 6.22 – 7.92 x $10^7$ $m^3$. The volume of sand in the crater is about 47-91% lower than the missing volume. This relation implies that the crater is unlikely to be trapping any additional flux of sand that is not being captured by the sand dunes themselves, and thus may not record the passage of previous generations of dune fields. By contrast, a fraction of the sand that was trapped in the crater likely escaped downwind or never entered the crater in the first place due to deflection by the topography of the raised rim.

### 4.5 Long-term Sand Input into Nathan's Crater

Dunes at Meroe Patera migrate an average of 0.5 ± 0.22m (2-sigma) per Earth year, with a range from ~0.1 to 1 m per Earth year. The average whole-dune sand flux observed at Meroe Patera is ~7 $m^3$/m/Earth yr, with maximum fluxes (migration rate multiplied by maximum dune height) of 11.5 $m^3$/m/Earth yr. We can estimate the sand flux these dunes deposit into the crater by multiplying the whole-dune flux by the fraction of the dune field area covered by dunes (0.6), and the diameter of the crater; the bulk sand flux associated with dunes alone is estimated to be 4.2 $m^3$/m/Earth year, with an associated flux into the crater of 7600 $m^3$/Earth year. We assume that the inter-dune sand flux is 1/3 of the maximum flux [*Ould Ahmedou et al.,* 2007]. This interdune flux is accordingly multiplied by the fraction of the dune field area not covered by dunes (0.4), to derive a total interdune flux of 1.5 $m^3$/m/Earth year. We add this interdune flux to the whole-dune flux to estimate a bulk flux for the Meroe Patera dune field of 5.7

$m^3$/m/Earth year. Given the crater's diameter of 1.8 km, we estimate a sand flux into the crater of 10300 $m^3$/Earth year.

The current migration rates of dunes $c_{dunes}$ at Meroe Patera can be combined with measurements of the dune field's size to estimate the likely timescale of dune activity at Nathan's Crater, under the assumptions of consistent wind conditions over the timescale of dune activity at Nathan's Crater, and *en masse* migration of the dune field at a rate $c_{field} = c_{dunes}$ as the migration rate of individual dunes. The downwind edge of the Meroe Patera dune field is about 7 km downwind of Nathan's Crater, and a sand sheet extends to about 13 km downwind. Given the dunes' observed migration rate of ~0.5 m per Earth year, and these measured distances, the upwind arrival of the dune field would have happened about 14,000-26,000 Earth years ago.

By multiplying the sand flux into the crater by the estimated timescale for dune activity at Nathan's Crater of ~14,000-26,000 Earth years, we can estimate the total sand volume $v_{shadow\_max}$ that has entered the crater, assuming constant climate over the history of the dune field at this site and that all passing sand has been trapped in the crater. This volume is 1.35 - 2.5 x $10^8$ $m^3$, much larger than our estimate of the volume of sand $v_{crater}$ trapped within the crater.

Alternatively, we can estimate $v_{shadow\_max}$ by multiplying our observed averaged sand thicknesses by the entire area of the "shadow" downwind of the crater, indicated schematically by the area between the dashed lines in Fig. 6. This includes those areas which are now covered by dunes due to lateral spreading of sand into the shadow. From

this, we estimate a total input volume of sand of 1.06 – 2.5 * $10^8$ $m^3$, similar to our time-based estimate of total input flux into the crater.

Thus, we estimate that the trapped sand volume $\boldsymbol{v_{crater}}$ in Nathan's Crater is only 15 ± 12% of the likely input volume $\boldsymbol{v_{shadow\_max}}$. Furthermore, these estimates of total input volume assume *en masse* migration of the whole dune field through time; if the dune field is not migrating in this matter, it could have persisted at Nathan's Crater for a much longer period of time, meaning that the actual long-term input sand volume could be much higher than we estimate.

The paucity of sand trapped within Nathan's Crater, relative to our estimates of the likely input volume it has received through time, could arise from two broad mechanisms. Firstly, it is possible that sand that has entered the crater has has been blown out over time. Alternatively, it is possible that passing sand may never enter the crater. We favor the first explanation over the second, due to a lack of morphological evidence for deflection of sand around the crater's raised rim. Mapping of dune brink lines around Nathan's Crater shows no evidence of deflection of the motion of oncoming dunes by the crater's rim (Fig. 4.8), and several dunes are observed to be actively climbing up over and falling into the crater in HiRISE images. This result should not be taken as a surprise, given that the slopes surrounding the exterior of Nathan's Crater's rim are low (~10 degrees), and active climbing dunes are observed on 15-degree slopes in Valles Marineris [*Chojnacki et al.,* 2010]. While the deflection of small portions of the input sand volume entering the crater rim near its northern and southern extremities cannot be ruled out, it is highly unlikely that the required majority

of the input sand volume has been lost in this way given the modern dune morphologies observed near Nathan's Crater.

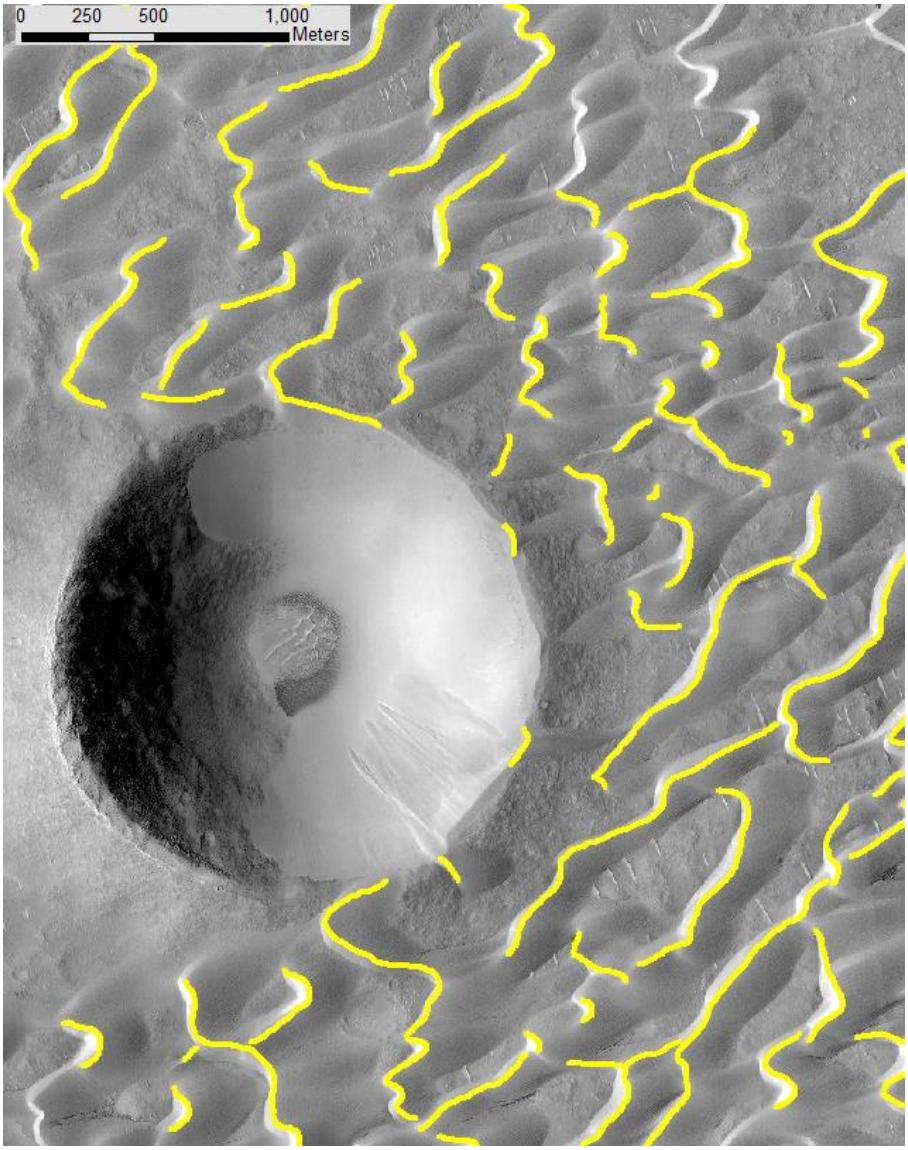


*Fig. 4.8:* Mapping of dune brink lines around Nathan's Crater. The orientation of dune brink lines does not change systematically near the crater.

We thus believe that Nathan's Crater, despite its appearance as a crater with rapid input and little visible output of sand in HiRISE images, is not an effective trap of

sand over long timescales. This discrepancy might imply past change in the wind regime at the crater, or the occurrence of past extreme sand transport events. Alternatively, strong winds impacting the upwind-facing crater wall could rapidly transport sand over and away from the wall, preventing accumulation of sand and bedform formation despite possibly significant fluxes.

Notably, the dunes downwind of the crater, even in the zone where dunes have reappeared, are smaller and more widely spaced than those found in other nearby parts of the dune field (Fig. 4.1), implying that a more limited sediment supply persists to the downwind edge of the dune field, likely due to sand trapped by the crater. The persistence of this altered morphology implies a consistent direction of the dominant sand transport since the dune field reached the crater and began depositing sand there. Our observation of effective long-term escape of sand at Nathan's Crater supports past studies of central mounds in much larger craters, such as Gale [e. g., *Kite et al.,* 2013; *Day & Kocurek,* 2016], which have invoked aeolian infill and exhumation as their formation mechanisms. However, the question of how extensive aeolian infilling of craters might occur at all, given the apparent difficulty of maintaining infill at this site, remains unresolved. Our results suggest that sand can be effectively removed from Martian craters over long timescales.

## 4.6 Conclusions

We investigate the effectiveness of sand trapping by an intra-dune field Martian crater by measuring its volume of trapped sand, and compare it to the amount

"expected" to be in the crater, based on observed sand thicknesses at the dune field and the size of the crater and a dune-free shadow extending downwind. The morphology of the shadow, the dunes downwind of it, and the dune migration rate, imply a consistent direction of sand transport at Meroe Patera for ~10,000 Earth years or longer. We find that the trapped volume is 85 ± 12% less than the expected volume, suggesting that the crater "leaks" sand downwind and is only partially successful at trapping it. While at first the crater appears to be an effective trap with minimal escape of sand in the present day, this appearance may simply be a result of strong winds leading to a lack of sand accumulation and possible rapid transport on the crater's downwind wall. Thus, the sand in Nathan's Crater sets a lower bound on the volume of passing sand. Our work sets the stage for the use of craters as sand traps elsewhere on Mars, Venus, and Titan in order to better understand the mechanics and histories of sand transport reflected in planetary aeolian environments.

**Acknowledgements**

This work was supported by funding from the King Abdulaziz City for Science and Technology, and from NASA Grant NNX16AJ43G/123117. We honor the memory of our prematurely late colleague, Nathan Bridges, who inspired the present work by occasionally mentioning, "there might be something to those crater sand shadows, but I'm not sure what." We also thank Dr. Mackenzie Day and an anonymous reviewer for their helpful reviews and comments.

# 5. Controls on the Global Distribution of Martian Landslides

Kevin P. Roback[1], Bethany L. Ehlmann[1,2]

[1] – Division of Geological and Planetary Sciences, California Institute of Technology, Pasadena, CA, USA

[2] – Jet Propulsion Laboratory, California Institute of Technology, Pasadena, California 91125, USA

**Abstract**

Recent acquisition of high-resolution satellite imagery of the Martian surface has permitted landslides to be studied on a global scale on Mars for the first time. We apply the Scoops3D software package to compute slope stability for select regions of the Martian surface, combining calculations of slope stability with number of observed landslides [*Crosta et al.*, 2018a, b], as reported in a recently published inventory of Martian landslides, to understand controls on the global distribution of landslides on Mars. We find that the distribution of landslides does not simply follow the distribution of unstable slopes. In particular, there is an abundance of landslides around Tharsis, and especially in Valles Marineris and Noctis Labyrinthus, that is not explained by an abundance of unstable topography alone. We analyzed for but did not find a clear large-scale lithologic or stratigraphic control on landslide occurrence from subsurface heterogeneities. Other possibilities to explain the increased occurrence of landslides in Tharsis include, (1) thin weak unit(s) that are regionally widespread and at multiple

stratigraphic levels, such as from interbedded ashes; (2) seismic activity related to the Tharsis's geological activity, and (3) possible groundwater near Valles Marineris into the Amazonian. Given the apparently young ages of many landslide deposits in Valles Marineris [*Quantin et al.,* 2004a], continued modern day analysis of lithologies in Valles Marineris and observations of Martian seismicity may act to strengthen or rebut the first two hypotheses.

## 5.1 Introduction

Since the arrival of the Mariner 9 spacecraft, large-scale landslides have been observed on Mars in the Valles Marineris canyon system [e.g., *Lucchitta*, 1978]. Many of these landslides are very large, with volumes in excess of 1000 $km^3$. Such landslides often include large slump blocks near the head of the landslide, separated from a larger apron comprising the furthest-traveling landslide debris by areas of hummocky or transversely ridged terrain [*Lucchitta et al.,* 1979]. Crater counting of landslide deposits in the Valles Marineris system has found that landslide ages vary widely from >3.5 Ga to 50 Ma [*Quantin et al.,* 2004a]. Additionally, landslides show similar morphology regardless of their age [*Quantin et al*., 2004a]; this implies that the factors causing landslides to occur in Valles Marineris have been at least episodically present through Mars's history into the Amazonian.

The factors causing landslides remain controversial, and have been studied through analysis of landslide morphology, comparisons to terrestrial analogs, and modeling of landslide geometries and movement. Some studies have promoted the importance of fluidization of the landslide mass with [*Lucchitta*, 1987; *Legros*, 2002;

*Harrison & Grimm*, 2003; *Quantin et al*., 2004b; *Roche et al.,* 2011] or without water and volatiles [*Hsü*, 1975; *McEwen*, 1989; *Lajeunesse et al*., 2006; *Soukhovitskaya & Manga*, 2006; *Johnson & Campbell*, 2017], and some landslides may have had lubricating, low-friction materials in their bases, such as ice, or hydrated/wet minerals [*Erismann*, 1979; *Shaller*, 1991; *De Blasio*, 2011; *Watkins et al*., 2015; 2020]. Fluidization via acoustic waves [*Melosh*, 1979] has also been explored. The involvement of ice and water, if present, would require Martian climate conditions to support, at a minimum, episodic availability of shallow ice deposits [e. g., *Lucchitta*, 1987; *Peulvast & Masson*, 1993; *Gourronc et al*., 2014], glaciers [*Fastook et al*., 2008; *Mège & Bourgeois*, 2010], or groundwater [*Nedell et al*., 1987; *Lucchitta et al*., 1994; *Harrison & Grimm*, 2005; *Harrison & Chapman*, 2008]. Seismicity has also been advanced as a potentially important factor [*Schultz*, 2002; *Quantin et al.,* 2004a; *Senthil Kumar et al*., 2019].

More recently, the proliferation of high-resolution imagery of the Martian surface generated by the CTX camera [*Malin et al*., 2007] has enabled landslides to be studied on a global scale. In particular, *Crosta et al.* (2018a,b) have characterized Martian landslides at a global scale for the first time with a published inventory of mapped Martian landslides (Fig. 5.1). They map 3,118 landslides with deposit areas greater than 0.1 $km^2$ between 60° N and 60°S. We apply this full inventory of landslides, excluding only those features mapped as rock glaciers, in this study. The highest density of landslides is found near Mars's equator, and particularly in the Valles Marineris region. Morphologically, rock avalanche landslides dominate across most of Mars's

surface, with slump landslides more prevalent in the outflow channels in the eastern part of the Valles Marineris system.

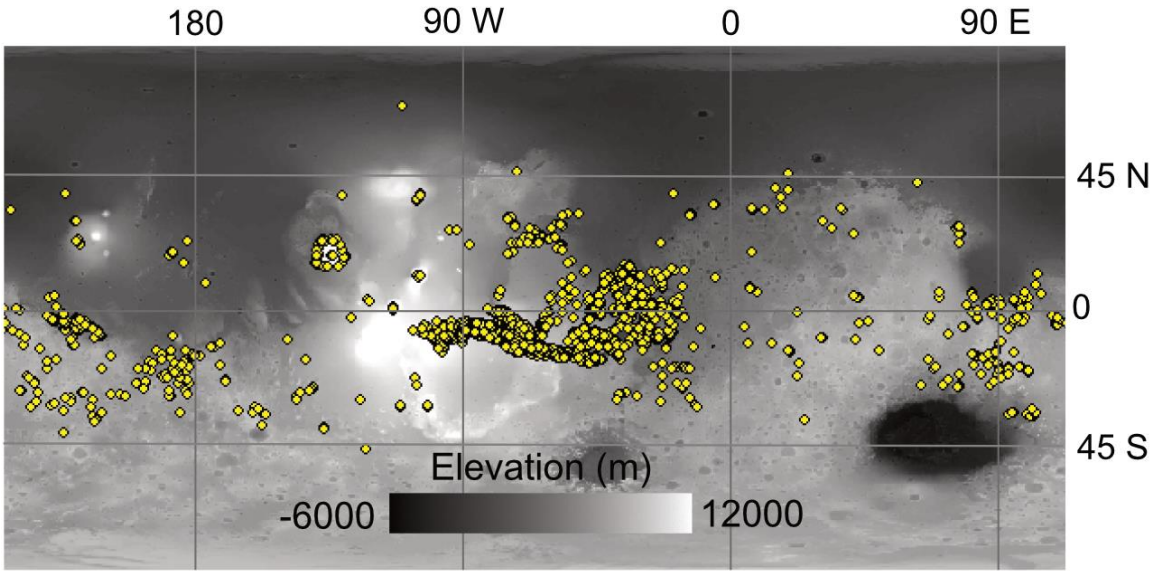


*Fig. 5.1:* The global landslide inventory, in point form and derived from CTX imagery, used as the basis of this analysis, by Crosta et al. (2018a) atop a grayscale Mars Orbiter Laser Altimeter (MOLA) global topographic map. All features aside from those mapped as rock glaciers are shown and were considered.

An area's landslide susceptibility is influenced by numerous factors. Some of these, such as hillslope angle and length, are observable from orbit. Others, such as rock strength, the presence of groundwater, and the history of seismicity in an area, are difficult or impossible to observe or infer from orbit. The study of spatial distributions of landslides can thus provide insight into these factors, if the different mechanisms which can trigger landslides can be distinguished uniquely.

We use the new (*Crosta et al*., 2018a) global landslide inventory in concert with global Martian datasets, including topography and faulting patterns, to undertake a comparative regional-scale analysis of factors driving the spatial distribution of landslides on the Martian surface. We first investigate the hypothesis that the distribution of landslides simply follows the distribution of unstable slopes on the Martian surface, i.e., that it is controlled by topographic characteristics alone. We then consider the possible influence of spatially varying tectonic seismicity on Mars, the possible influence of variable rock strength, and the possible influence of groundwater on interpretation of our modeling results.

## 5.2 Methods

### 5.2.1 Digital elevation model dataset

For input to slope stability models, we used elevation data from High Resolution Stereo Camera (HRSC) DEMs, downsampled via bilinear interpolation to a common resolution of 200m/pixel to remove any potential influence of DEM resolution on the stability analysis. The average height error of 11.6 m associated with HRSC data has little impact on our factor of safety calculations, as we are considering the susceptibility to large-scale landslides, big enough to be mapped from orbit by *Crosta et al.* (2018) on slopes hundreds of meters to kilometers in height. We chose this HRSC DEM dataset because of its availability, its large regional coverage, and its demonstrated greater accuracy in the steepest topography in comparison to CTX DEMs created by us. We attempted to rapidly produce CTX DEMs for some of our study areas via Ames Stereo Pipeline terrain-processing tools [*Beyer et al*., 2018], but experienced sporadic large

errors (on the order of 50-100m) in excess of those associated with HRSC data in high topography portions of Valles Marineris. Due to our need to acquire topographic data across large portions of Mars's surface quickly, we chose the already-available HRSC dataset rather than working to further improve the CTX DEM quality of each stereo pair.

### 5.2.2 Calculating susceptibility to landsliding with Scoops3D

To quantify the relative susceptibility to landsliding of various topographies on Mars, we apply the Scoops3D software package developed by the USGS [*Reid et al.,* 2015]. Scoops3D calculates the forces driving and resisting motion on a large number of possible spherical trial landslide surfaces generated underneath an input digital elevation model. These trial surfaces are spheres drawn around nodes placed at intervals set by the user above an input digital elevation model (DEM); we set this interval to be 200 m. The number of trial surfaces generated per DEM was typically on the order of $10^6$, varying with the spatial extent of each DEM.

Since the trial landslide surfaces are spherical, the landslides are simulated as rotational failures. Though we cannot know definitively that past landslides on Mars happened as rotational failures, arcuate planes of failure are commonplace in materials without large contrasts or discontinuities in strength [*Hoek & Bray*, 1981], and anticipated by numerical modeling [*Katz et al*., 2014]. Additionally, many of the largest landslides on Mars [e. g., *Lucchitta et al*., 1979] show curved source scars. However, in materials with strong discontinuities or planes of weakness, such as weak rock layers, this assumption may lead to a relative underestimation of the actual landslide

susceptibility. The possible implications of such heterogeneity in subsurface material properties are discussed more fully in section 4.2.2.

The model splits a trial failure mass into columns, whose position and size are set by the horizontal resolution of the DEM. Over each of these, driving and resisting forces are calculated and summed to derive an estimate of the ratio between the total forces resisting motion divided by the total forces driving motion of the trial landslide, known as the factor of safety (FOS) (Fig. 5.2). Higher values of the FOS, output pixel by pixel for each DEM cell, indicate greater stability. Simpler slope stability modeling techniques commonly involve application of 2D infinite-slope modeling techniques [e. g., *Cernica*, 1995; *Sharma*, 1994] to individual cells of a DEM on a pixel-by-pixel basis; these approaches assume slopes are infinite in extent, and neglect effects such as added resistance at the toe of a slope, and the differing depths of failure planes by slopes of different lengths. Scoops3D simulates trial landslide failure surfaces in 3D, integrating the effects of topographic wavelength (the length of slopes) on the calculation of the stability of trial landslide surfaces, and the determination of the most-probable landslide size and depth associated with the least-stable trial failure surface. Commonly, slopes with averaged large-scale angles of ~25 degrees receive are assigned FOS values <2, while slopes with ~20 degree average gradients get FOS = 2-3.

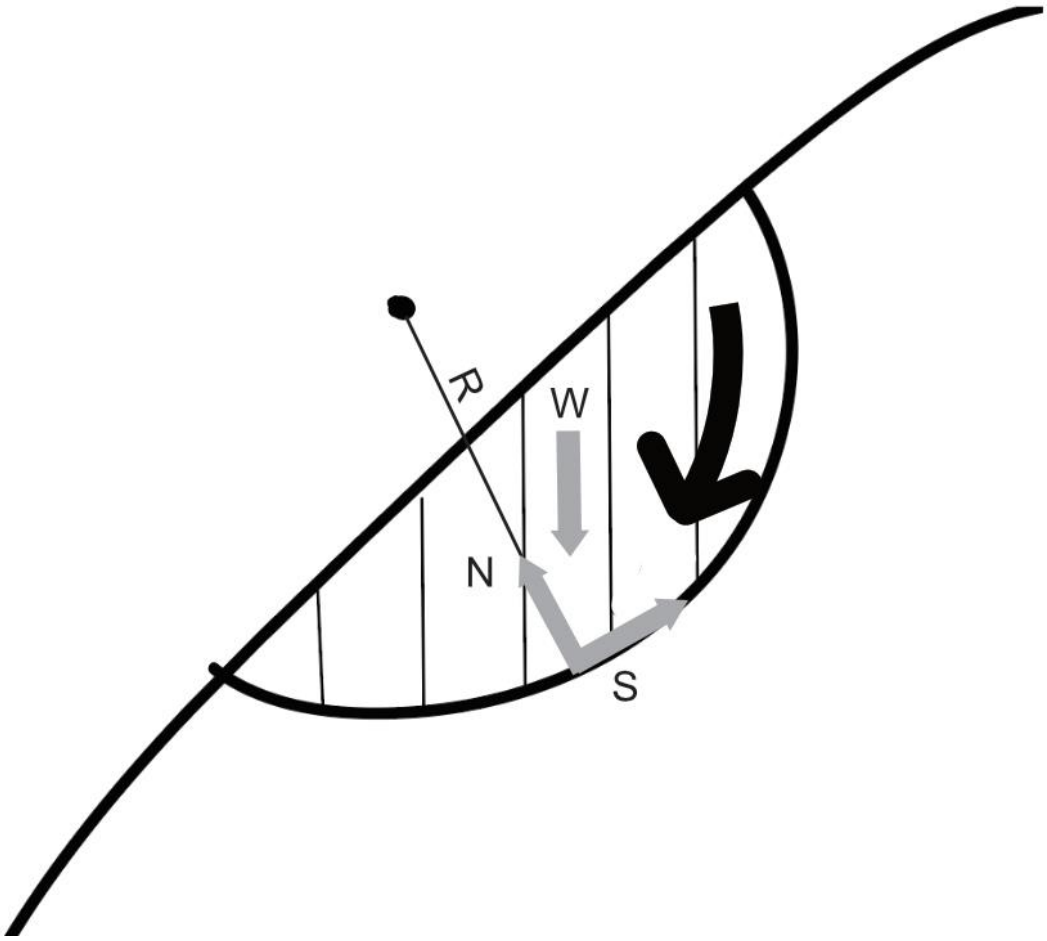


*Fig. 5.2:* Simplified schematic of the rotational failure geometry and relevant forces as set up by the Scoops3D slope-stability model. W = column weight; N = normal force; S = shear force; R = distance from axis of rotation to base of a particular column in the trial failure mass.

To calculate the FOS, we input into Scoops3D a constant set of material parameters, including cohesion, angle of internal friction, and weight, for all study areas to best isolate the impact of topography alone on the relative stability of different Martian landscapes. Parameters were set to values corresponding to a low-end intact rock strength, such as that which might correspond to a terrestrial shale. In particular,

the cohesion was set to 1 MPa, the angle of internal friction to 30 degrees, and the weight of material to 10 kN/m$^3$. Typical cohesions for terrestrial rocks range from ~1-100 MPa; angles of internal friction can vary from ~15 to 50 degrees [*Goodman*, 1980]. For Martian rocks, strengths have been estimated both at the local scale from rover-based measurements [*Okubo*, 2007; *Thomson et al*., 2013] and at the large scale from strength modeling of Valles Marineris hillslopes [*Schultz*, 2002]. At the rover scale, local rock outcrops analyzed at Eagle and Erebus craters by the Mars Exploration Rover (MER) Opportunity had unconfined compressive strengths of ~10 MPa, corresponding to cohesions of ~5 MPa [*Okubo*, 2007]. Outcrops analyzed in Gusev Crater by MER Spirit had higher strength (cohesions of 35-70 MPa), but those in the Columbia Hills included some weaker material (cohesions of 0.5-25 MPa). At the large scale, other slope stability analyses [*Clow et al.*, 1988; *Schultz*, 2002] have estimated bulk strength of wallrock of 0.1-0.4 MPa, suggesting that the large-scale strength of rock may be set by fracture patterns.

Note that the weight of material is set lower than typical weights of terrestrial rocks and soils (20-30 kN/m$^3$) due to Mars's lower gravity (~38% of Earth's). The permissible volume range of trial landslide failure surfaces was set to $10^8 – 10^{12}$ m$^3$; the high bound on possible landslide volume is set given the scale of landslide deposits observed in Valles Marineris [*Lucchitta*, 1979]. A Bishop's simplified limit-equilibrium method was used [*Hungr*, 1987]. This method assumes horizontal side forces, computed on the basis of the column's weight and the angle of the sliding surface below the center of each column, between the vertical columns comprising the modeled landslide failure mass.

Earthquake loading and the presence of groundwater were not incorporated into the model setup; the point of this analysis is to consider the impact of topography alone (see 'A role for groundwater?' in the Discussion section). However, as stated previously the FOS in this modeling scheme is a function of more than the local slope angle.

### 5.2.3 Statistical analyses of landslide occurrence

The distribution of landslides was then compared to the distribution of unstable slopes, i.e., slopes below a given factor of safety, via means of a window-based analysis. Analyzed parts of the Martian surface [see Fig. 5.4, and link to our publicly archived slope stability data at the end of the paper] were divided into 20-km square windows in equal-area projections; the 20-km length-scale was chosen to balance minimizing the occurrences of large landslides spanning multiple terrain windows, along with generating a large population of windows to differentiate between terrains of different stability levels. Within each window, the number of landslides was tallied, along with the fraction of the topography with a calculated factor of safety below a certain threshold deemed "unstable." For windows covered incompletely with slope stability data (i. e., on the edge of our HRSC DEM coverage), we calculated the percentage of unstable slopes with the available DEM data. We varied the threshold FOS to evaluate sensitivity to the choice, using values ranging from 3 to 6. In all plots presented here, we use 4 as the "unstable" threshold factor of safety value, unless otherwise noted, as the results were not very sensitive to the choice. The range of values we explored for the FOS threshold is informed partially by the range of FOS values computed for areas of observed, recent landslides on Mars; a histogram of FOS values acquired in the vicinity

of mapped Martian landslides is provided in Fig. 5.3. Landslides go from being extremely abundant in topographies at FOS < 3 to extremely rare at FOS = 6. Of the ~2000 landslides that lie within areas covered by our FOS modeling, >95% of the landslides occur in areas with a modeled FOS < 4, hence the choice of 4 as the threshold value for instability value focused on in these analyses of % unstable topography. This pattern of FOS values holds whether we consider the FOS values computed at the centroid of the landslide's source area (Fig. 5.3., left panel), or the FOS values computed in a 5-km circular neighborhood around the centroid of the source area (Fig. 5.3, right panel).

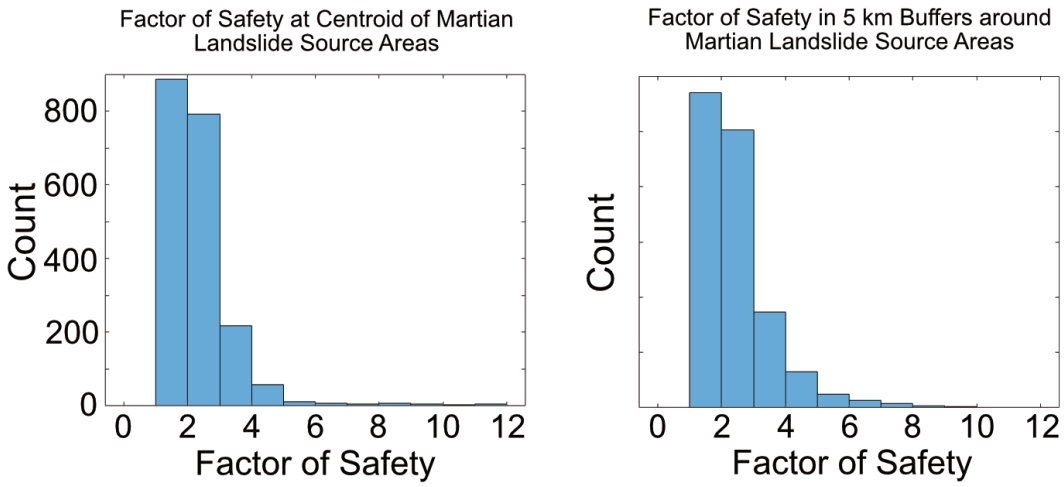


*Fig. 5.3:* Left panel - FOS modeling results extracted at the centroids of source areas of landslides as mapped by Crosta et al. (2018). Right panel - FOS modeling results extracted across 5 km circular windows around the centroids of mapped Martian landslides.

Windows were then binned by their fractional percentage of unstable slopes, and landslide populations of bins with the same percentage of unstable slopes were

compared across different geographic regions of the Martian surface. Studied and compared regions include Valles Marineris, Elysium Mons, Olympus Mons, Kasei Valles, Nili Fossae, Libya Montes, Noctis Labyrinthus, and a general region for all other studied terrain, which is mostly mapped as Noachian Highlands [*Tanaka et al.*, 2014] (Fig. 5.4). Across our studied areas, we delineated more than 50,000 terrain windows, covering an area of Mars's surface in excess of 20 million km$^2$.

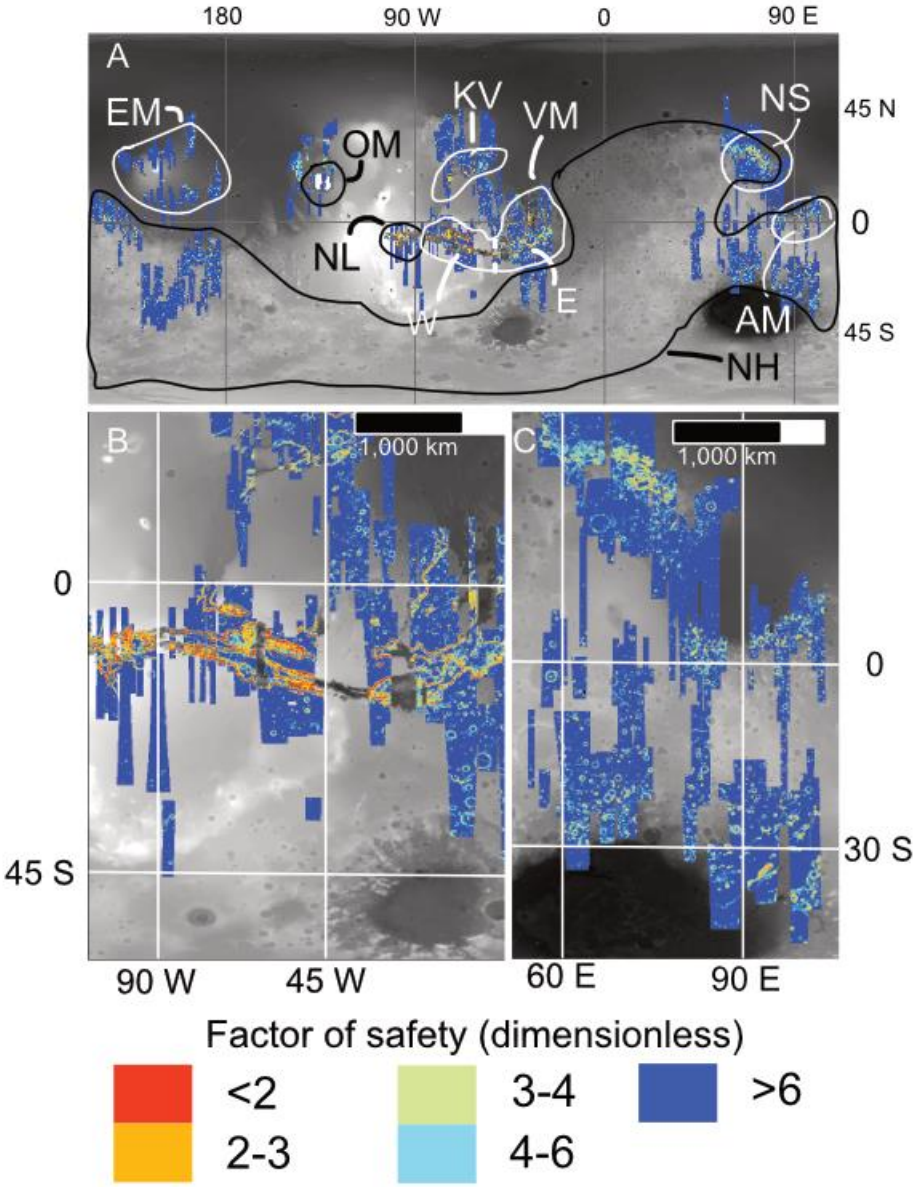

*Fig. 5.4:* (A) – HRSC DEM coverage of the Scoops3D slope-stability modeling performed in this study atop MOLA topography. Regions of interest: EM = Elysium Mons; OM = Olympus Mons; NL = Noctis Labyrinthus; KV = Kasei Valles; VM = Valles Marineris; NH = Noachian Highlands; AM = Aeolis Mensae; NS = Nilosyrtis Mensae. (B) Scoops3D coverage for the Valles Marineris area. E and W delineate the eastern and western parts of the Valles Marineris system as defined in this study. (C) Scoops3D coverage in areas near Syrtis Major.

The statistical significance of differences in landslide occurrence between bins from different regions was evaluated via the use of a Wilcoxon rank-sum test on the population of windows within each bin. All windows were included in the Wilcoxon rank-sum comparison, whether they did or did not have landslides. The Wilcoxon rank-sum test was chosen because the populations of landslides in each bin were generally distributed in a non-Gaussian way, with most windows hosting 0-1 landslides and a typically small number of windows hosting multiple landslides. If the output p-value from the rank-sum test was <0.05, indicating a >95% confidence that the difference in landslide abundance between the two bins, was not a result of random sampling from the same distribution of landslides, we consider the difference in landslide abundance between the bins to be statistically significant. Further, we only consider differences in landslide abundance to be significant if $p < 0.05$ is satisfied for different choices of the "unstable" threshold factor of safety value.

The Wilcoxon rank-sum test often, but not always, supports statistically significant differences between pairs of bins in which the average number of landslides

per window is greatly different. Factors which can lead to $p > 0.05$ (meaning that the bins are not deemed significantly different) for pairs of bins with different overall abundances of landslides include small populations of windows in one or both bins as well as the presence of outlier windows, e.g., when the number of windows in one of the pairwise compared bins is very small (generally <5) while there exists one or a small number of windows with many (generally >5) landslides. These outlier windows can significantly increase the average landslide abundance in a particular bin, but have less of an impact on the Wilcoxon rank-sum test, which is more sensitive to the overall distribution and abundance of landslides across many windows.

In the analyses presented here, we group Martian terrain into 10 stability bins, corresponding to 10% increments of unstable slope abundance. In general, decreasing the number of bins acts to increase the number of windows in each bin, increasing the odds of differences being found statistically significant. However, larger bins group a greater range of terrains together, leaving more possibility for a difference in landslide abundance between regions to be explainable as a difference in topography. Sensitivity tests performed with different numbers of bins found that our results were not generally sensitive to the number of bins used, for ranges of ~5-20 bins.

### 5.2.4 Examination of a role for faulting

To investigate the possible impact of tectonic seismicity on Martian landslides, we applied an inventory of surface faulting as mapped by *Knapmeyer et al*. (2006). They map faults ranging from 4 to 1445 km in length. The previously described method of

window-based analysis was repeated, except that for the faulting case, we compared populations of windows that were within 50 km of a mapped Martian fault to populations of windows that were more than 50 km from a mapped fault. Extremely large (M8-9) earthquakes on Earth can trigger landslides more than 200 km from the epicenter, but for M6-8 earthquakes, 50-100 km is a more typical distance to the furthest landslides [*Keefer*, 1984]. The distance of 50 km was also chosen in part because increasing the buffer around faults beyond this distance greatly decreases the amount of available terrain that is classified as far from a fault, hindering the ability of our statistical test to identify significant differences. Additionally, we do not consider the ages of either landslide scars or fault lines in our method; the ages of landslide scars are not reported by *Crosta et al.* (2018a), as many landslide scars are too small to be crater-counted, and the process would be prohibitively labor intensive for an inventory of >3,000 landslides.

## 5.3 Results

We observe that, in general, topography is a primary control on the distribution of Martian landslides. As expected, windows with abundant unstable terrain are much more likely to host a landslide, but even terrains that are >90% unstable have landslides in only ~20-40% of the terrain area windows (Fig. 5.5). However, significant differences in landslide abundance not related to topography are observed between some regions of the Martian surface. In particular, regions around Tharsis show more landslides than regions elsewhere on Mars, even when controlling for percentage unstable topography and utilizing different factors of safety (Fig. 5.6).

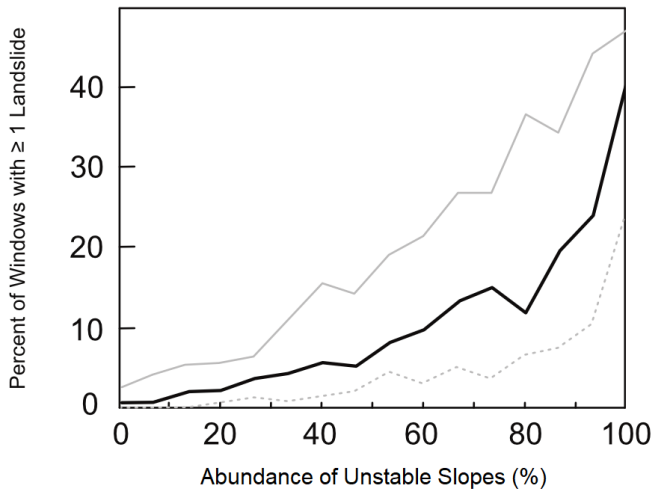


*Fig. 5.5:* Abundance of landslides as a function of percent abundance of unstable slopes, for all data averaged globally across the Martian surface. Gray line computed using unstable FOS threshold = 3; black line using FOS threshold = 4 and gray dashed line using FOS threshold = 6.

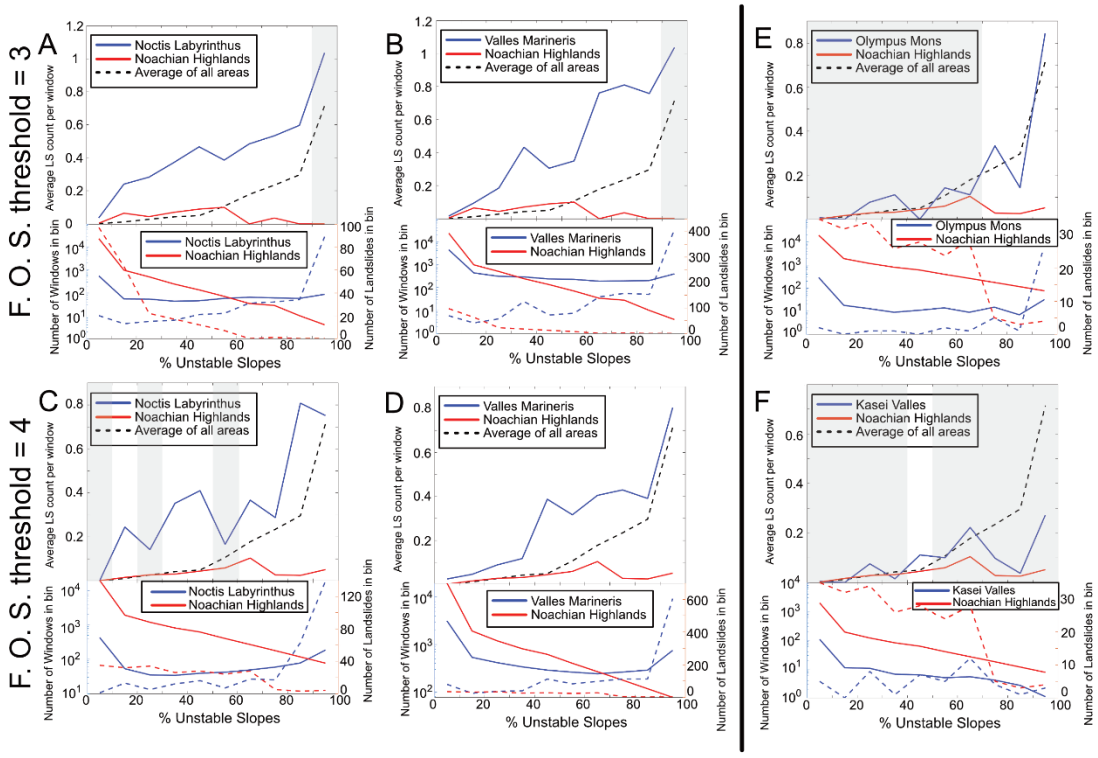

*Fig. 5.6:* Comparisons of unstable slope vs landslide occurrence involving regions in the Tharsis area, Noctis Labyrinthus (A, C) and Valles Marineris (B, D) as compared to Noachian Highlands terrain for different factors of safety. First row (A, B) indicates curves calculated using an unstable FOS threshold = 3; second row (C, D) indicates curves calculated using an unstable FOS threshold = 4. Areas in white are statistically significant while shaded areas mark parts of the curve in which the differences in landslide abundance between the compared regions are not significant at a 95% confidence level. In the lower panels, the solid lines correspond to the left y-axis and the dashed lines to the right y-axis.

These differences are most pronounced in comparing Noctis Labyrinthus (Fig. 5.6A, 5.6C) and Valles Marineris (Fig. 5.6B, 5.6D) to Noachian terrains. Landslides are more common in these two regions in the heart of Tharsis than other Martian regions, and comparison of most bins of similar topographies show differences in landslide abundance that are significant at >95% confidence level. These differences persist across different choices of the threshold factor of safety value used to define “stable” and “unstable” terrain. In other regions around Tharsis, such as Olympus Mons (Fig. 5.6E) and Kasei Valles (Fig. 5.6F) areas, landslides are more common relative to Noachian terrain, but the differences in landslides do not meet our criteria for statistical significance for most bins, in part due to the small sizes of these regions and correspondingly small populations of topographic “windows” with few landslides each. We also attempted to compare Olympus Mons to Elysium Mons, in an effort to compare large volcanic edifices near and far from Tharsis. However, there is a general lack of

steep topography in the Elysium Mons area comparable to the aureoles surrounding the Olympus Mons edifice, which are the origins of most of Olympus's landslides. Thus, the only comparable bins between the two regions are low-instability bins with very few landslides; these bins do not host statistically different landslide abundances.

Comparisons between different parts of Tharsis (Fig. 5.7) generally do not reveal statistically significant differences in landslide abundance, although landslides are more common in Valles Marineris and Noctis Labyrinthus relative to other Tharsis areas. Additionally, we compare the eastern and western parts of the Valles Marineris region to see if a contrast in the composition of subsurface materials exhumed by impact craters, which was reported by *Quantin et al.* (2012), has any apparent impact on landslides. There is no statistically significant variation in landslide frequency across this lithologic contrast (Fig. 5.7C).

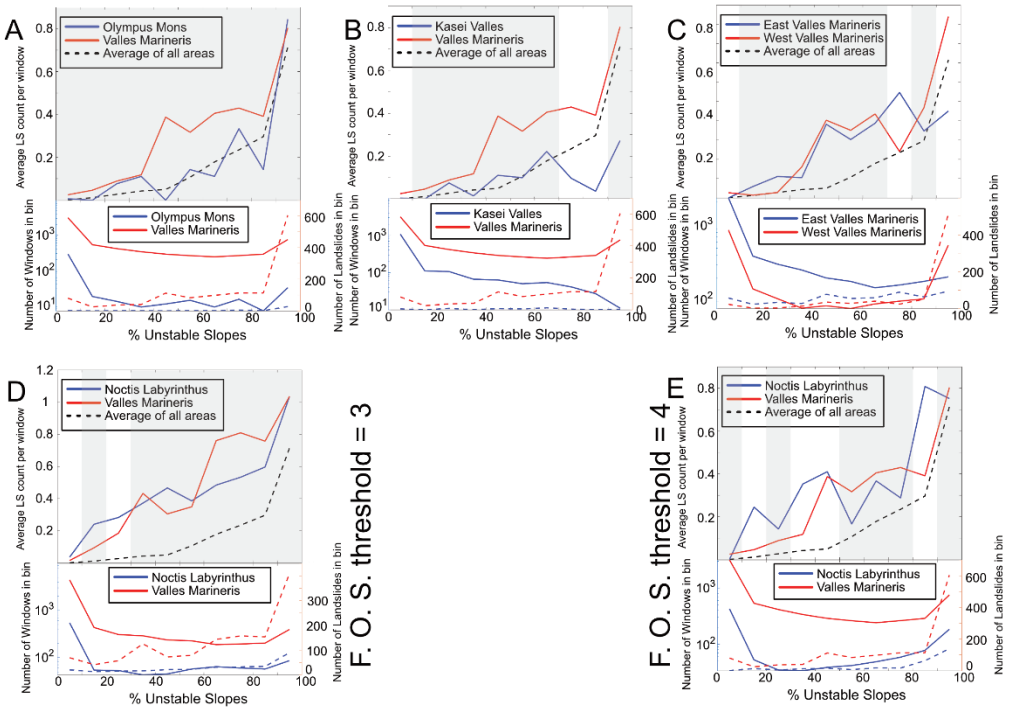


*Fig. 5.7:* Comparisons of unstable slope vs landslide density between different regions in the vicinity of Tharsis; Olympus Mons & Valles Marineris (A), Kasei Valles & Valles Marineris (B), eastern and western Valles Marineris (C), and Noctis Labyrinthus and Valles Marineris (D & E). In panel C, the east/west division (see Fig. 4B) follows the contrast in subsurface material properties observed by *Quantin et al.* (2012). In panel D, an unstable FOS threshold of 3 is used to compute slope stability; in all other panels the unstable FOS threshold is assumed to be 4. Shading and axes correspondence to lines are as in Fig. 5.6.

Mapped faulting also does not appear to be a major control on mapped landslides (Fig. 5.8). A global comparison of mapped landslides for areas within 50 km of a mapped surface-exposed fault versus areas further away shows variation only in the

most unstable terrain (Fig. 5.8A). However, the terrain driving this variation turns out to be concentrated almost exclusively in the Valles Marineris and Noctis Labyrinthus areas (Fig. 5.8B & 5.8C). When these areas are excluded, no significant differences associated with windows close to or far from faulting are observed elsewhere across the planet. In Valles Marineris, areas with >90% unstable terrain have statistically higher landslide occurrences if <50 km from a mapped fault (Fig. 5.8C).

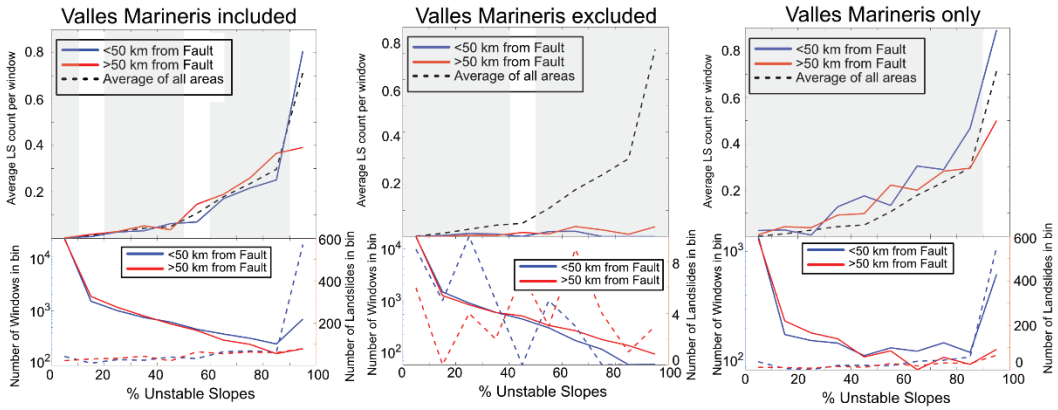


*Fig. 5.8:* Comparison of landslide abundance as a function of slope stability for areas close to and far from a mapped fault, for all global data, for all global data excluding Valles Marineris, and for Valles Marineris only. Shading and axes correspondence to lines are as in Fig. 5.6.

## 5.4 Discussion

### 5.4.1 Global Landslide Prevalence

Our results comparing landslide occurrence in terrains of equivalent instability suggest that the abundance of landslides in regions around Tharsis, and particularly near Valles Marineris, is not solely related to the presence of abundant steep topography in

this area. Landslide abundance correlates with topographic stability in Tharsis, but not in Noachian Highlands terrain, for the values of the "unstable" factor of safety threshold presented here. The cause of this lack of correlation may be the fact that most Noachian Highlands landslides are hosted in the walls of impact craters. The slopes of these impact craters are rather short in length, meaning that they occupy rather limited portions of the 20-km windows considered in our analysis; this provides a population of landscape windows that can host landslides despite having comparatively small areal extents of unstable slopes. Larger craters with longer hillslopes filling larger portions of our 20-km windows do not exist in heavily cratered Noachian terrain, because craters above 3-8 km in diameter take on complex-crater morphologies [*Pike*, 1980] with wall slope angles set by the spontaneous gravitational collapse of the bowl-shaped "transient crater" during an impact event.

Large areas of unstable slopes in Noachian terrain are uncommon; the largest of these is found in the fretted terrain in Nilosyrtis Mensae, which contains few visible landslides. This region shows extensive exposures of hydrated minerals [*Bandfield & Amador*, 2016], implying possible past groundwater. It also may have experienced extensive glacial modification [*Levy et al*., 2007], which may have erased traces of landslides which may have occurred in the region's early history.

Interestingly, the Aeolis Mensae region, a geomorphologically similar region with fretted terrain along the boundary of the Noachian highlands, contains far more landslides that Nilosyrtis Mensae, though unstable slopes are actually less abundant (Fig. 5.9). The Elysium Mons volcanic edifice, located ~500 km from landslide-affected

regions in Aeolis Mensae, is farther away than the distances over which landslides are observed to be seismically triggered on Earth, even by extremely large earthquakes [*Keefer*, 1984]. A possible factor is lithology, as portions of Aeolis Mensae are interpreted to be volcanic ash [*Kerber et al*., 2011], and interbedded ash layers might provide planes of weakness for sliding.

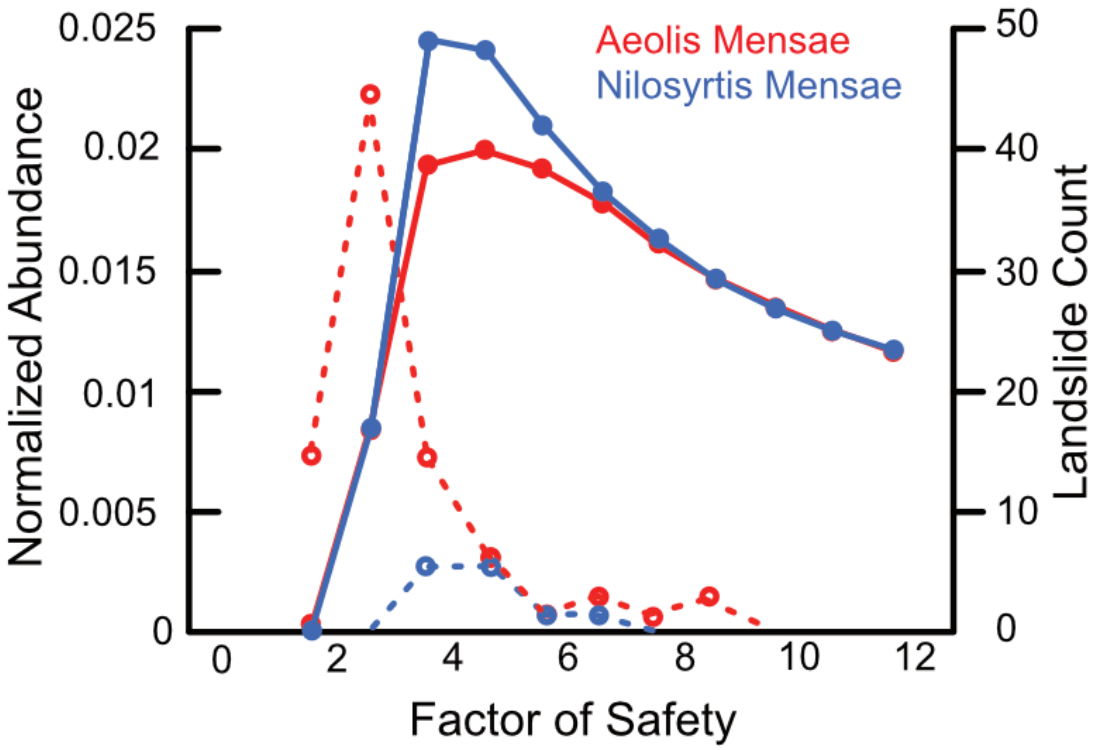


*Fig. 5.9:* Comparison of abundance of unstable slopes for Nilosytis Mensae and Aeolis Mensae. Landslide abundances are given by the dotted lines. Unstable slope abundance is normalized by the total area of analyzed terrain in each respective area.

The main question arising from our work is the cause of the elevated landslide abundance in Valles Marineris, and the Tharsis rise region more broadly. Additional

factors we have considered include possibly enhanced Tharsis seismicity, the possible presence of a "weak layer" or layers low in the stratigraphy in the Valles Marineris area, and a possible atypical abundance of groundwater in the vicinity of the Valles Marineris area.

### 5.4.2 Why does the Tharsis area have more landslides?

#### *5.4.2.1 A possible role for seismicity?*

Seismicity associated with the extensive tectonic and volcanic activity surrounding Tharsis may be a key contributor to landslide abundance, as suggested previously in the literature [*Quantin et al*., 2004a]. There are far more faults around Tharsis than elsewhere on Mars [*Golombek et al*., 1992], implying more seismicity near Tharsis [*Anderson et al*., 2001; 2008]. Although, as previously discussed, landslides do not follow patterns of mapped faulting in general across Mars, faults may have also been much more active in the vicinity of Tharsis, as would be expected given the larger scale of the chasmae and volcanic edifices present there. Indeed, there is a statistically significant increase in landslides in windows with the most unstable topography (>90%) when those windows are <50 km from a fault (Fig. 5.8) in the Valles Marineris region. Additionally, Tharsis may harbor other deep faults obscured by comparatively recent volcanic activity. If seismicity is indeed the cause of most landslides in Valles Marineris, it may persist and be observable into the present day given the apparently youthful age of many landslide deposits [*Quantin et al*., 2004a]. Seismic data from InSight or future network missions may yet fully map Martian global seismicity.

#### 5.4.2.2 A role for heterogeneous subsurface lithologies?

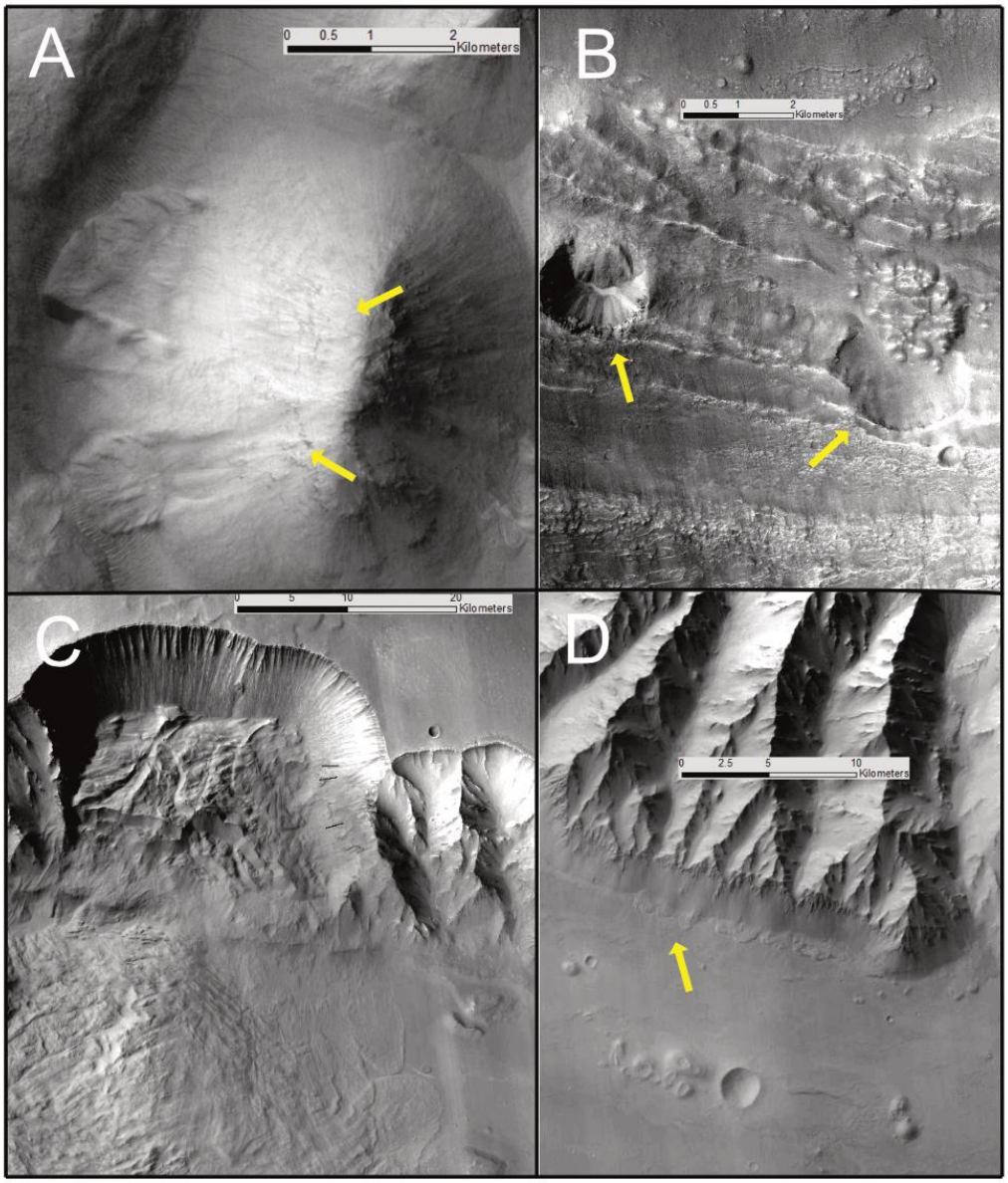


*Fig. 5.10:*Panels A and B: Examples of landslides with an identifiable basal scarp in eastern Valles Marineris. Panel C: Example of a large rotational slump whose scar is not clear of landslide debris in Valles Marineris. Panel D: Area with several overlapping rock avalanche deposits, but no clear corresponding source area on the cliffs above. Arrows

point to basal scarps of landslides in panels A and B, and areas of landslide deposits in panel D.

Another idea that has been suggested in the literature [*Montgomery et al*., 2009] is a rheological "weak layer" at depth as a possible facilitator of large-scale gravity spreading in the Tharsis area. Such a layer could be dictated by mineralogy, e.g., clay minerals [e.g., *Watkins et al*., 2015; 2020] or by the physical properties of the rock, e.g., loosely consolidated sediments or pyroclastics (e.g., *Bandfield et al.,* 2013). We mapped source areas of landslides throughout the Valles Marineris and Noctis Labyrinthus regions, searching for debris-free landslide scarps from which the elevation of the bottom of the landslide failure plane could be estimated (e.g., Fig. 5.10, panel A). We mapped an area including 1,766 landslides mapped by *Crosta et al.* (2018a), but could only find clear basal scarps for 109 (~6%) of these landslides. This in large part reflects modes of failure in Valles Marineris; most landslides in the canyon are rock avalanches found below steep cliffs which lack a clear source area (e. g., Fig. 5.10, panel D); slump-type landslides, those with clear mappable scarps, are less common. Additionally, for many slumps, especially larger ones, much of the landslide mass has not evacuated the scarp area; this leaves the basal shear surface obscured (Fig. 5.10, panel C).

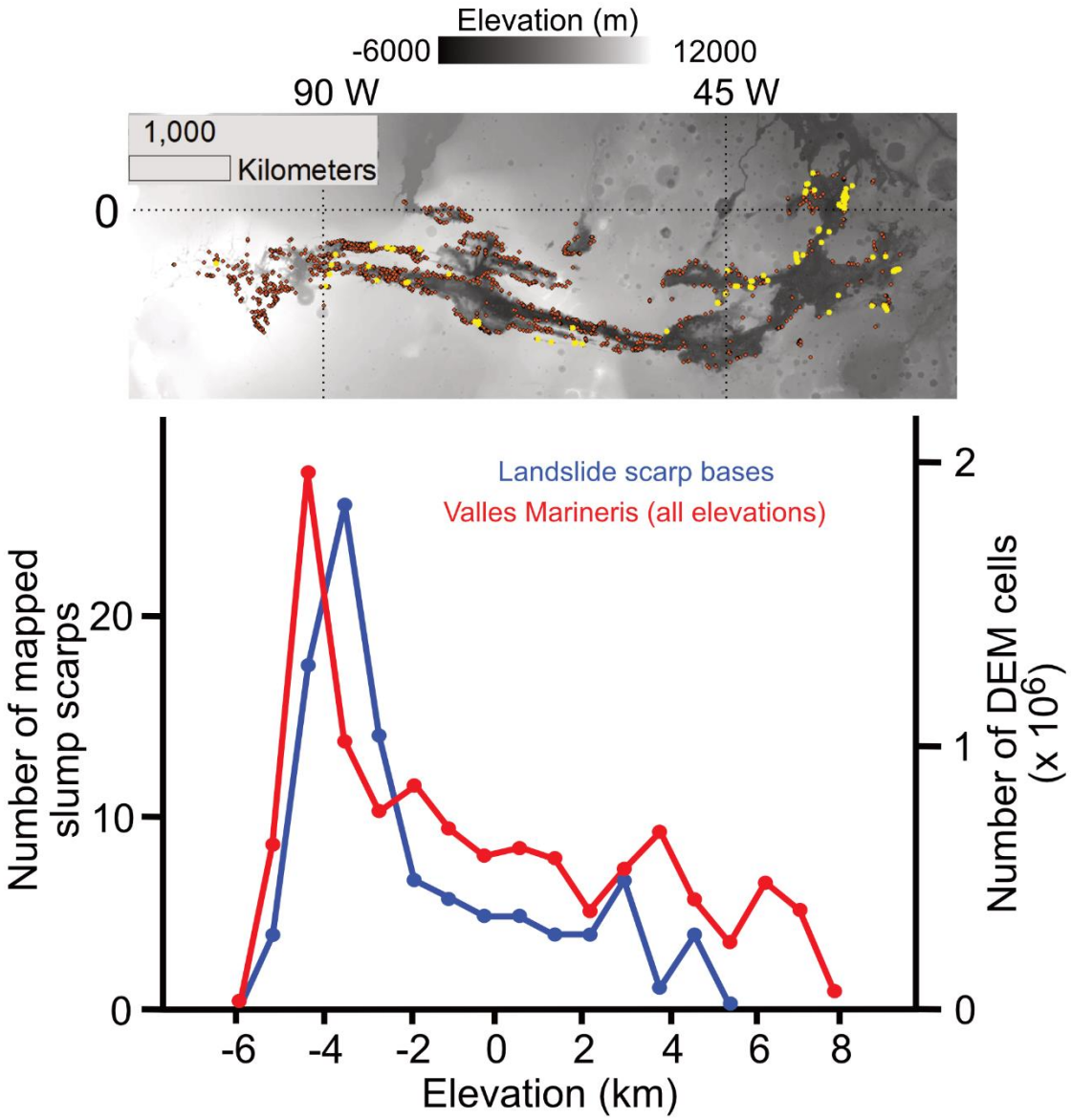


*Fig. 5.11:* Plot of elevations of mapped landslide scarps, and of all elevations in Valles Marineris slopes & canyon floor. Bins are in 1000 m increments, with the lowest bin starting at -5800 m. Inset – View of all mapped landslides in Valles Marineris (orange dots), and all landslides for which a scarp was successfully identified (yellow dots). Elevation data predicted here is from MOLA (Mars Orbiter Laser Altimeter).

The 109 identified basal scarps are clustered at low elevations in Valles Marineris (Fig. 5.11) and are found preferentially in the eastern part of the canyon system. The preference for the eastern part of the canyon for this form of scarp is interesting as *Quantin et al.* (2012) previously reported a change in subsurface lithology from west to east. Most of the successfully identified basal scarps are relatively small (~1 $km^2$ or less) and are located at or below the elevation (about -2000 m) at which low-calcium pyroxene (LCP)-rich, massive light-toned rocks are reported to typically occur [*Quantin et al*., 2012; *Flahaut et al*., 2012] in eastern Valles Marineris. Relative to the distribution of topography in Valles Marineris, landslides are moderately more abundant than expected between -2000 and -4000 m elevation. It may be that these LCP lithologies or their boundaries with adjacent units are more conducive to the formation of rotational slumps of this scale; these rock units are described as "massive" [*Quantin et al*., 2012; *Flahaut et al*., 2012], implying a lack of strong jointing or layering observable from orbit. Terrestrial studies have found that landslides in strongly jointed or layered rocks are much more likely to take other forms including rockfalls, topples, and rock avalanches [*Guzzetti et al*., 1996; *Hermanns & Strecker*, 1999]. However, slumping, especially translational slumping along a plane of weakness, is still possible. Smooth rotational slumps can also still form if the scale of failure is much larger than the scale of layering or jointing, as intact rock is fractured between moving planes of weakness.

Despite this clustering of slumps at low elevations, the overall abundance of landslides remains similar from the lower-elevation slopes of Valles Marineris to Noctis Labyrinthus, where chasma walls host landslides at elevations of 3000 – 7000 m, above

the levels at which many landslides are observed in Valles Marineris, and above the levels of previously suggested weak layers in the stratigraphy. If stratigraphy in the Tharsis area is assumed to be generally horizontal, this variation in elevations of landslides implies that landslides are hosted in a variety of rock units of different ages. Lower elevation outcrops in the Valles Marineris system have been interpreted as outcrops of primitive Noachian crust [*Quantin et al.,* 2012; *Flahaut et al.,* 2012], while lava flows associated with Tharsis are thought to comprise the stratigraphy at higher elevations [*Murchie et al.,* 2009], though lavas may also be present in the lower elevations of Tharsis [*Golombek & Phillips*, 2010]. Additionally, landslides are similarly present across the differences in subsurface materials exhumed by impacts, observed by *Quantin et al.* (2012). This prevalence of landslides is an argument against characteristics of any particular lithologic unit controlling landslide distribution, although the morphological expression of landslides may vary depending on strength and homogeneity of the particular rock unit and lithologic heterogeneities at smaller scale than observable from orbit could still play a role in dictating the planes of failure.

The layer with abundant slump scarps may invoke comparisons to the weak layer suggested to exist by *Montgomery et al.* (2009) in the lower portions of Valles Marineris's stratigraphy, and to the low thermal inertia, putative volcaniclastic material inferred to exist by *Bandfield et al.* (2013). It is possible that material in the higher elevations of the Valles Marineris stratigraphy is indeed more well lithified than the lower-elevation massive layers, but the effective material strength at large scales may be set by systems of joints and fractures formed naturally from post-eruption cooling of

the lava flows often assumed to comprise the higher parts of Valles Marineris stratigraphy. In summary, though slumps with clear basal scarps appear to be concentrated in a relatively low-elevation unit in the Valles Marineris system, these slumps represent only a minority of all landslides present near Valles Marineris; most are rock avalanches which lack a clear basal scarp. This makes it difficult to tie most landslides to particular stratigraphic units. However, given our coarse knowledge of lithologic units on Mars, lithologic controls could nonetheless be important.

#### *5.4.2.3 A role for groundwater?*

Groundwater presence, perhaps episodically related to periodic glacier formation on Tharsis, predicted by climate models [*Fastook et al.,* 2008], and volcanic activity, is another possible contributor to enhanced landslide activity. Groundwater fills pore spaces in rock; this both makes a bulk volume of rock heavier and induces a pore pressure which reduces resisting stress normal to the failure plane, but does not reduce the driving shear stress parallel to the failure plane, leading to easier failure of slopes. Numerous outcrops of aqueous minerals are found in the Valles Marineris region [e.g., *Murchie et al.,* 2009; *Ehlmann & Edwards*, 2014], and many of these outcrops are interpreted to be relatively young [*Milliken et al.,* 2008; *Weitz et al.,* 2013], implying that groundwater and surface water may have persisted in this area longer than in other regions of the Martian surface. Given the inferred young age of many Valles Marineris landslides [*Quantin et al.,* 2004a] these relatively young mineral deposits could advance a case for groundwater as a potentially important factor. Precise age dates for aqueous

deposits on Valles Marineris, acquired from in situ or sample return missions, could confirm the hypothesis of persistent groundwater in Valles Marineris.

## 5.5 Conclusions

By applying a new global inventory of landslides and slope-stability modeling techniques, we analyzed spatial patterns of Martian landslides while controlling for the stability of topographies across different Martian terrains. The results indicate an abundance of landslides around Tharsis, and particularly around the Valles Marineris area. The effect is not solely due to the abundant steep topography in these areas. We analyzed for, but did not find a clear local lithologic or stratigraphic control on landslide occurrence from heterogeneities in the crust. Other possibilities to explain the increased occurrence of landslides in Tharsis include (1) regionally widespread Tharsis weak unit(s), such as from interbedded ashes and lavas; (2) seismic activity related to the Tharsis's geological activity, and (3) possible groundwater near Valles Marineris into the Amazonian. Given the apparently young ages of many landslide deposits in Valles Marineris [*Quantin et al.,* 2004a], continued modern day analysis of lithologies in Valles Marineris and observations of Martian seismicity may act to strengthen or rebut the first two hypotheses.

**Acknowledgements**

Thanks to Susan Conway and Matt Golombek for thorough reviews that improved this manuscript. We thank Giovanni Crosta and Paolo Frattini for both providing early access to their Martian landslide inventory prior to its publication, and

providing early feedback and critique of this work. We also thank Martin Knapmeyer for providing us with access to his mapped inventory of Martian faults. We also thank Jay Dickson for help in compiling and processing the Mars datasets. Our dataset of slope-stability calculations generated for this work, as well as a list of all HRSC DEMs used and all window-by-window calculations of landslide count and unstable slope abundance, for different choices of the "unstable" slope threshold for all studied regions of Mars is publicly archived:

Roback, K. P., and Ehlmann B. L., 2020, *Martian Slope Stability Data*, version 1.0. CaltechDATA. doi:10.22002/D1.1617.

# 6. Thesis Conclusions

## 6.1 On the use of image correlations to measure sand transport on planetary surfaces

This thesis has demonstrated the utility of automated image correlation in measuring short-timescale variations in sand transport from HiRISE satellite images taken of Mars's surface. Sand transport is also, however, an important and widespread process on Earth; active sand dunes are widespread in some arid areas, and their motion can present major challenges for nearby communities [*Amin & Seif*, 2019]. Additionally, many non-desert areas contain stabilized sand dunes which have been activated at times during the Holocene [e. g., *Forman et al.*, 2001], and may be reactivated by future climate change [*Thomas et al.*, 2005; *Yizhaq et al*., 2009a]. Thus, there is interest in applying our techniques that were successfully used on Mars to monitor the motion of sand on Earth.

On Earth, a great variety of satellite images are freely available for public analysis. Landsat and ASTER images offer resolutions in the panchromatic band as high as 15 m/pixel; Sentinel images offer resolution up to 10 m/pixel. Other proprietary datasets commonly used include Worldview images (up to 31cm/pixel), SPOT images (up to 1.5 m/pixel in SPOT 6 & 7), and Planet Labs images (up to 50cm/pixel in SkySat data). The size range of bedforms produced in sand on Earth is decidedly bimodal; on the small scale, ripples referred to as *impact ripples* form at typical wavelengths of ~10 cm; these ripples are much too small to be tracked in any satellite image. However, dunes, which

range in wavelength from several m to several km on Earth [*Breed & Grow*, 1979], can be resolved and therefore theoretically tracked in many datasets.

Some studies have had success in using automated image correlation routines implemented in COSI-Corr to measure sand dune migration over long timescales in satellite images. *Vermeesch & Drake* (2008) use ASTER images to measure the migration rates of the world's fastest moving sand dunes in the Bodele Depression of Africa. Most further studies of dune motion [*Hermas et al.,* 2012; *Necsoiu et al.*, 2009; *Vermeesch et al.*, 2012; *Scheidt & Lancaster*, 2013; *Al-Ghamdi & Hermas*, 2015; *Sam et al.*, 2015; *Al-Mutiry et al*., 2016] have used SPOT or ASTER datasets, with some usage of Landsat. We have tried to improve upon this work by measuring sand dune motion over shorter timescales with rapid-repeat imagery available from Planet Labs [*Houborg & McCabe*, 2018].

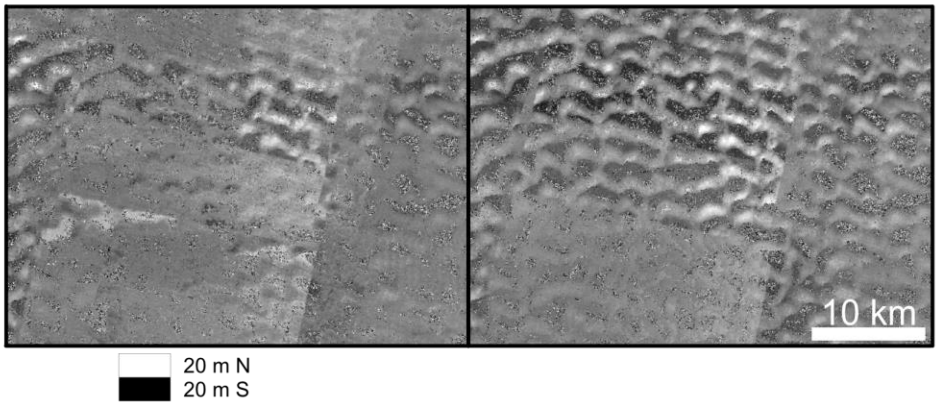


*Fig. 6.1:* View of results of correlations acquired from Planet Labs L3H images of dunes near Shaybah, Saudi Arabia, acquired 7 days apart in April 2019.

This work has produced poor-quality results, however (Fig. 6.1). This sample correlation map, depicting apparent surface displacements between a pair of Planet Labs images, shows large artifacts, greater in magnitude than the signal of dune displacement to be measured; these are the slanted box patterns most visible near the bottom left part of the correlation map. Though we can try to apply the advanced analytical techniques described in Ch. 3, such as independent component analysis (ICA), to separate the signal from artifacts as was done for Mars, we have not had success in the Earth cases we have studied. This is partially due to the fact that at <1 yr timescales, typical artifacts from misregistration of satellite images, on the order of a few meters, overwhelm the signal associated with dune motion. Our machine learning techniques to separate artifacts from signal are generally less reliable in the case where the signal of interest is not the primary "signal" in an image correlation. Additionally, machine learning techniques suffer from the limitation that they are "black boxes" in the sense that an algorithm's design often does not obviously relate to the nature of outputs it produces.

In particular, the ICA algorithms operate by separating out different sources of variance in a difficult-to-visualize higher dimensional data space. For example, in our correlation maps generated at the Nili Patera dune field on Mars (Ch. 3), we use 40 correlation maps, which generate a 40-dimensional data space. The exact structure of these signals in this abstract space is challenging to visualize, and they may be separated out in different ways by different "contrast functions" in different ICA algorithms. It is rarely obvious how one might adjust an ICA's parameters to extract a particular signal of

interest. It is also challenging to determine whether a signal might be extractable with ICA at all; the present best bet is to try large numbers of ICA analyses via "brute force" with varying parameters. We have tried this "brute force" approach with PlanetScope images, but found that some kinds of artifacts cannot be successfully separated from the signal using any choice of parameters in an ICA scheme (Fig. 6.2). Thus, though the success of the technique at Nili Patera demonstrates the potential power of ICA in resolving signals in complex datasets, the technique does not seem to be universally applicable. Improvements to camera models and image processing that minimize the sizes of artifacts in satellite images would help avoid the need to rely on ICA-type techniques to measure dune motion over short timescales in Earthly dune fields.

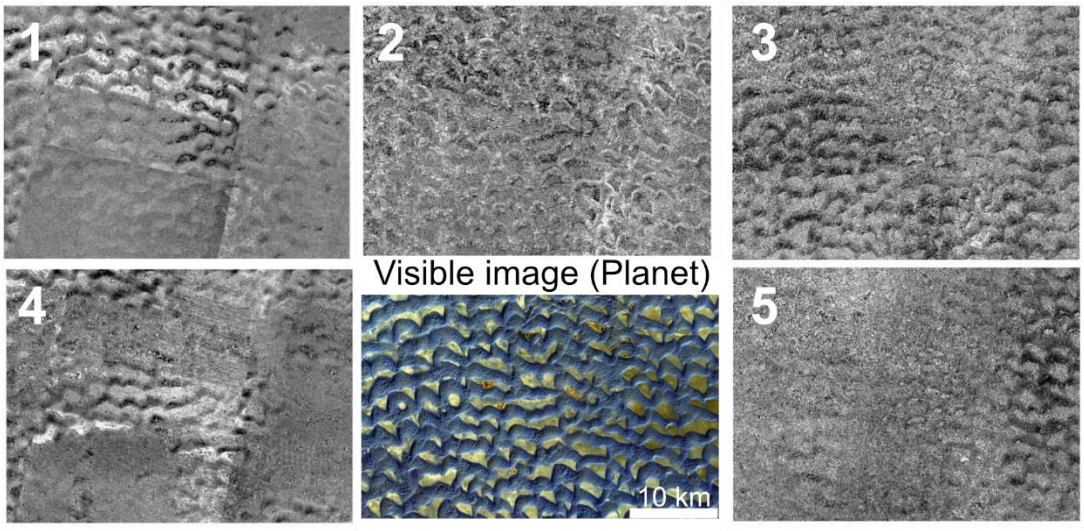


*Fig. 6.2:* Sample of components extracted from applying ICA to the correlation maps generated from Planet Labs images over the dunes near Shaybah, Saudi Arabia; these are numbered by their relative contribution to the total variance of the correlation map. Compare to Fig. 3.6; unlike in the HiRISE datasets, ICA does not succeed in separating

different sources of variance in Planet Labs images at Shaybah. Additionally, in the bottom center panel, an image of the dune field from Planet Labs is provided.

Another challenge for terrestrial environments is the different size ranges of bedforms on Earth and Mars [*Lapotre et al.*, 2016]. On Mars, the presence of ripples with wavelengths of several meters on sand dunes provides bedforms of a nearly-optimal size range for satellite-image-based tracking. These ripples are big enough to be resolved from space in HiRISE images, but small enough to migrate rapidly, at speeds sometimes exceeding 10 m/Earth year, in contrast with Martian dunes which rarely exceed 1 m/Earth year. Bedforms of this scale are uncommon on Earth, however; mega-ripples [*Bagnold*, 1941; *Yizhaq*, 2009b] of this wavelength are present occasionally, but are thought to require a particular grain size population including a large number of grains which are too large to move via saltation, and a consistent supply of smaller grains which slowly move the larger grains via successive impacts as they saltate. Where present, these mega-ripples have been documented to migrate quickly at times under high winds [*Sakamoto-Arnold*, 1988], so they might be tracked over short timescales as ripples on Mars are.

However, this could not be done in many areas. The ubiquitous aeolian bedforms on Earth are dunes and ~10 cm scale impact ripples. The impact ripples are too small to be tracked in satellite images; meanwhile, dunes are so large that their motion can rarely be resolved confidently on weekly or monthly timescales on Earth. The fastest dunes measured on Earth, found in the Bodélé Depression in Chad, in Africa, have been measured to move at speeds of a few m per month [*Vermeesch & Drake*, 2008], but

most dunes move much slower than this, at speeds of a few m per year. The highest resolution images available of Earth's surface are ~30 cm per pixel, so typically a minimum dune motion on the order of 1 m is needed to be resolvable in the best satellite images, and this motion only happens over several months or longer at most sites. This limitation will challenge efforts to relate sand transport and weather observations, or climate model predictions, on Earth. However, significant value can still be gained from long-timescale studies of dune migration, as these can assist in planning for communities in arid areas.

## 6.2 On the use of landslide inventories to understand material properties and processes on exotic planetary surfaces

Aside from Earth and Mars, landslides have been mapped on the surfaces of Venus [*Malin*, 1992], the Moon [*Pike*, 1971], Mercury [*Brunetti et al.*, 2015], and even Jupiter's moon Io [*Schenk and Bulmer*, 1998] Pluto's moon Charon [*Beddingfield et al.*, 2020], and many of Saturn's moons [*Beddingfield et al.*, 2015]. The spatial distribution of landslides on these objects' surfaces might reveal the influence of factors such as variations in subsurface material strength, fluid presence, or seismic activity as was investigated for Mars in chapter 5. In order to replicate our method of comparing landslide density to unstable slope abundance across regions of a planetary surface, landslide inventories and topographic data must be available across the regions of interest.

Getting this data is generally challenging, however. Landslide mapping is best done in imagery of the highest resolution possible; this enables smaller landslides to be identified and makes the inventory more complete. On Earth, imagery with a resolution of ~30 cm/pixel is commercially available, and the inventory we analyze for Mars in Ch. 5 [from *Crosta et al.* 2018a] was produced primarily via mapping in 7m/pixel Context Camera (CTX) images. However, in missions to exotic planetary surfaces, images with resolutions of hundreds of m to km per pixel are more commonly acquired, due to the constraints associated with mission design and the transfer of large datasets from faraway spacecraft back to Earth.

These low-resolution viewpoints limit our knowledge of landslides on most planetary surfaces to only km-scale features. This may provide a very limited view of a surface's actual landsliding; landslides of this scale make up only a tiny fraction of all landslides that happen on Earth [*Stark & Hovius*, 2001]. The actual size-frequency distributions of landslide populations on other planetary surfaces may differ significantly from that of Earth; in particular, landslides occurring on planets with lower surface gravities may trend towards larger sizes, as greater volumes of material are needed to provide enough shear stress to overcome cohesion on surfaces with lower gravity. This effect may impact landslides on Mars as suggested by *Crosta et al.*, 2018a; they note that landslides with affected areas below $10^7$ $m^2$ are relatively less abundant in Martian landslide populations relative to those on Earth.

This is unlikely to reflect limitations associated with image resolution, as landslides of this scale can be confidently identified in the CTX images used to create the *Crosta et al.* 2018a landslide inventory. Aside from gravity, differences in the weathering processes that make unconsolidated material on different surfaces, differences in landslide-triggering processes like seismicity, and differences in slope angle and relief [e. g., *Korup et al.*, 2007; *Jeandet et al.*, 2019] might also impact landslide size distributions.

Going forward, an interesting opportunity to reapply our landslide-analysis method may be provided by the VERITAS mission proposed to explore Venus [*Freeman et al.*, 2016]. Though Venus's atmosphere makes it opaque to visible light, the VISAR instrument proposed for VERITAS would map the surface at 15-30 m/pixel resolution; the images provided would be close in resolution to the 7m/pixel images from the Context Camera that have been used to map landslides on Mars. Topography would also be provided at a resolution of 250 m, close to the 200 m resolution data we analyzed in combined and resampled HRSC datasets for Mars.

Given Venus's absence of surface water and lack of daily temperature cycling caused by its thick atmosphere, any detectable variations in landslide abundance not tied to topography would likely be driven by spatial variations in seismicity, or rock strength. Venus's surface hosts an abundance of forms and terrain types that appear to be formed by tectonic activity, including tessera, mountain belts, and groove belts [*Ivanov & Head*, 2011]. The zones of these features would be particularly interesting targets for landslide mapping and cross-region comparison, as many of them have relief

sufficient to host actual landslides; previous work scrutinizing 75 m/pixel Magellan cycle-1 photographs [*Malin*, 1991] over limited parts of Venus's surface found abundances of landslides in some areas, with particularly good assemblages of landslides found in Aphrodite Terra. Studying these landslides might hint at spatial variations in Venus's recent seismic activity, and inform discussion of the planet's evolution.

# References


Al-Ghamdi, K., & Hermas, E., 2015, Assessment of dune migration hazards against qlanduse northwest Al-lith City, Saudi Arabia, using multi-temporal satellite imagery: *Arabian Journal of Geosciences*, *8*, 11007-11018, doi:10.1007/s12517-015-1947-8.

Al-Mutiry, M., Hermas, E., Al-Ghamdi, K., & Al-Awaji, H., 2016, Estimation of dune migration rates north Riyadh City, KSA, using SPOT 4 panchromatic images: *Journal of African Earth Science*, *124*, 258-269, doi:10.1016/j.afrearsci.2016.09.034.

Almeida, M. P., Parteli, E. J. R., Andrade Jr., J. S., & Herrman, H. J., 2008. Giant saltation on Mars: *Proceedings of the National Academy of Sciences of the United States of America*, *105*(17), 6222-6226, doi:10.1073/pnas.0800202105.

Amin, A., & Seif, E. S. S. A., 2019, Environmental Hazards of Sand Dunes, South Jeddah, Saudi Arabia: An Assessment and Mitigation Geotechnical Study: *Earth Systems and Environment*, doi:10.1007/s41748-019-00100-5.

Anderson, R. C., Dohm, J. M., Golombek, M. P., Haldemann, A. F. C., Franklin, B. J., Tanaka, K. L., Lias, J., & Peer, B., 2001. Primary centers and secondary concentrations of tectonic activity through time in the western hemisphere of Mars*: Journal of Geophysical Research*, *106*, 20,563-20,585.

Anderson, R. C., Dohm, J. M., Haldemann, A. F. C., Pounders, E., Golombek, M., & Castano, A., 2008. Centers of tectonic activity in the eastern hemisphere of Mars: *Icarus*, *195*, 537-546, doi:10.1016/j.icarus.2007.12.027.

Anderson, R. S., 1987. A theoretical model for aeolian impact ripples. *Sedimentology*, *34*, 943-956.

Andreotti, B., 2004. A two-species model of aeolian sand transport: *Journal of Fluid Mechanics*, *510*, 47-70, doi:10.1017/S0022112004009073.

Andreotti, B., Claudin, P., & Pouliquen, 2010. Measurements of the aeolian sand transport saturation length: *Geomorphology*, *123*, doi:10.1016/j.geomorph.2010.08.002.

Andreotti, B., Claudin, P., Jacob Iversen, J., Merrison, J. P., & Rasmussen, K. R., 2021. A lower-than-expected saltation at Martian pressure and below: *Proceedings of the National Academy of Sciences*, *118*(5), doi:10.1073/pnas.2012386118.

Ashkenazy, Y., Yizhaq, H., & Tsoar, H., 2012. Sand dune mobility under climate change in the Kalahari and Australian deserts: *Climatic Change*, *112*, 901-923, doi:10.1007/s10584-011-0264-9.

Atwood-Stone, C., and McEwen, A. S., 2013. Avalanche slope angles in low-gravity environments from active Martian sand dunes. *Geophysical Research Letters*, *40*, 2929-2934.

Ayoub, F., Avouac, J. P., Newman, C. E., Richardson, M. I., Lucas, A., Leprince, S., & Bridges, N. T., 2014. Threshold for sand mobility on Mars calculated from seasonal variations of sand flux. *Nature Geoscience*, *5*(5096), doi:10.1038/ncomms6096.

Bagnold, R. A., 1937. The transport of sand by wind: *The Geographical Journal*, *89*, 409-

438.
Bagnold, R. A., 1941. The Physics of Blown Sand and Desert Dunes: *Chapman and Hall,* London, 265.
Baird, T., Bristow, C. S., & Vermeesch, P., 2019. Measuring Sand Dune Migration Rates with COSI-Corr and Landsat: Opportunities and Challenges: *Remote Sensing*, *11*(20), doi:10.3390/rs11202423.
Baker, M. M., Newman, C. E., Lapôtre, M. G. A., Sullivan, R., Bridges, N. T., & Lewis, K. W., 2018. Coarse sediment transport in the modern Martian environment. *Journal of Geophysical Research: Planets*, *123*(6), 1380-1394.
Bandfield, J. L., Edwards, C. S., Montgomery, D. R., & Brand, B. D., 2013. The dual nature of the martian crust: Young lavas and old clastic materials: *Icarus*, *222*, 188-199.
Bandfield, J. L. & Amador, E. S., 2016. Extensive aqueous deposits at the base of the dichotomy boundary in Nilosyrtis Mensae, Mars: *Icarus*, *275*, 29-44.
Banfield, D. B., et al., 2019. InSight Auxiliary Payload Sensor Suite (APSS). *Space Science Reviews*, *215*(4), doi:10.1007/s11214-018-0570-x.
Banfield, D., et al., 2020. The atmosphere on Mars as observed by InSight: *Nature Geoscience*, doi:10.1038/s41561-020-0534-0.
Banks, M. E., et al., 2018. Patterns in mobility and modification of middle-and high-latitude southern hemisphere dunes on Mars. *Journal of Geophysical Research: Planets*, *123*(12), 3205-3219.
Beddingfield, C. B., Burr, D. M., & Dunne, W. M., 2015. Shallow normal fault slopes on Saturnian icy satellites: *Journal of Geophysical Research-Planets*, *120*(12), 2053-2083.
Beddingfield, C. B., et al., 2020. Landslides on Charon: *Icarus*, *335*, doi:10.1016/j.icarus.2019.07.017.
Bennett, S. J., & Best, J. L., 1996. Mean flow and turbulence structure over fixed ripples and the ripple-dune transition, *in* Ashworth, P. J., et al., eds., Coherent flow structures in open channels: Hoboken, New Jersey, John Wiley, p. 67-125.
Beyer, R. A., Alexandrov, O., & McMicheal, S., 2018. The Ames Stereo Pipeline: NASA's Open Source Software for Deriving and Processing Terrain Data: *Earth and Space Science*, *5*, 537-548.
Bourke, M. C., Ewing, R. C., Finnegan, D., and McGowan, H. A., 2009. Sand dune movement in Victoria Valley, Antarctica: *Geomorphology*, *109*(3-4), 148-160, doi:10.1016/j.geomorph.2009.02.028.
Boynton, W. V., et al., 2002. Distribution of Hydrogen in the Near Surface of Mars: Evidence for Subsurface Ice Deposits: *Science*, *297*(5578), 81-85, doi:10.1126/science.1073722.
Breed, C. S., & Grow, T., 1979, Morphology and distribution of sand seas observed by remote sensing: *in* A Study of Global Sand Seas, ed. McKee E. D., USGS Professional Paper 1052.
Bridges, N. T., Ayoub, F., Avouac, J. P., Leprince, S., Lucas, A., & Mattson, S., 2012. Earth-like sand fluxes on Mars. *Nature*, *485*(7398), 339-342.
Brunetti, M. T., Xiao, Z., Komatsu, G., Peruccacci, S., Guzzetti, F., 2015. Large rock slides

in impact craters on the Moon and Mercury: *Icarus*, *260*, 289-300, doi:10.1016/j.icarus.2015.07.014.

Carta, J. A., Ramírez, Velázquez, S., 2009. A review of wind probability distributions used in wind energy analysis: Case studies in the Canary Islands: *Renewable and Sustainable Energy Reviews*, *13*, 933-955, doi:10.1016/j.rser.2008.05.005.

Cernica, J. N., 1995. Geotechnical Engineering: Soil Mechanics: *Wiley,* New York, 488 p.

Chojnacki, M., Moersch, J. E., & Burr, D. M., 2010. Climbing and falling dunes in Valles Marineris, Mars: *Geophysical Research Letters*, *37*, doi:10.1029/2009GL042263

Chojnacki, M., Banks, M. E., Fenton, L. K., & Urso, A. C., 2019. Boundary condition controls on the high-sand-flux regions of Mars. *Geology*, https:doi.org/10.1130/G45793.1.

Claudin, P., & Andreotti, B., 2006. A scaling law for aeolian dunes on Mars, Venus, Earth, and for subaqueous ripples: *Earth and Planetary Science Letters*, *252*, 30-44, doi:10.1016/j.epsl.2006.09.004.

Clow, G. D., Moore, H. J., Davis, P. A., & Strichartz, L. R., 1988. Stability of chasma walls in the Valles Marineris, Mars (abstract): *Lunar and Planetary Science Conference XIX*, 201-202.

Courrech du Pont, S., Narteau, C., & Gao, X., 2014. Two modes for dune orientation: *Geology, 42*(9), 743-746, doi:10.1130/G35657.1.

Crosta, G. B., Frattini, P., Valbuzzi, E., & De Blasio, F. V., 2018a. Introducing a new inventory of large Martian landslides: *Earth and Space Science*, *5*(4), 89-119.

Crosta, G. B., De Blasio, F. V., & Frattini, P., 2018b. Global scale analysis of Martian landslide mobility and paleoenvironmental clues: *Journal of Geophysical Research: Planets*, *123*(4), 872-891.

Cutts, J. A., & Smith, R. S. U., 1973. Eolian Deposits and Dunes on Mars: *Journal of Geophysical Research*, *78*(20), 4139-4154.

Davila, A. F., Fairén, A. G., Stokes, C. R., Platz, T., Rodriguez, A. P., Lacelle, D., Dohm, J., & Pollard, W., 2013. Evidence for Hesperian glaciation along the Martian dichotomy boundary: *Geology*, *41*(7), 755-758.

Day, M. & Kocurek, G., 2016. Observations of an aeolian landscape: From surface to orbit in Gale Crater: *Icarus*, *280*, 37-71, doi:10.1016/j.icarus.2015.09.042.

De Blasio, F. V., 2011. Landslides in Valles Marineris (Mars): a possible role of basal lubrication by sub-surface ice: *Planetary and Space Science*, *59*, 1384-1392.

DiBiase, R. A., Limaye, A. B., Scheingross, J. S., Fischer, W. W., & Lamb, M. P., 2013. Deltaic deposits at Aeolis Dorsa: Sedimentary evidence for a standing body of water on the northern plains of Mars: *Journal of Geophysical Research: Planets*, *118*(6), 1285-1302.

Durán, O., Parteli, E. J. R., & Herrmann, H. J., 2010. A continuous model for sand dunes: review, new developments and application to barchan dunes and barchan dune fields: *Earth Surface Processes and Landforms*, *35*, 1591-1600, doi:10.1002/esp.2070.

Duran, O., Claudin, P., & Andreotti, B., 2014. Direct numerical simulations of aeolian sand ripples. *Proceedings of the National Academy of Sciences of the United States of America*, *111*(44), 15665-15668, doi:10.1073/pnas.1413058111.

Duran Vinent, O., Andreotti, B., Claudin, P., & Winter, C., 2019. A unified model of ripples and dunes in water and planetary environments: *Nature Geoscience*, *12*, 345-350, doi:10.1038/s41561-019-0336-4.

Edgell, H. S., 2006. Arabian Deserts: *Springer Netherlands,* Dordrecht.

Ehlmann, B. L. & Edwards, C. S., 2014. Mineralogy of the Martian surface: *Annual Review of Earth & Planetary Sciences*, *42*, 291-315.

Erismann, T. H., 1979, Mechanisms of large landslides: *Rock Mechanics,* v. 12, p. 15-46.

Fastook, J. L., Head, J. W., Marchant, D. R., & Forget, F., 2008. Tropical mountain glaciers on Mars: Altitude-dependence of ice accumulation, accumulation conditions, formation times, glacier dynamics, and implications for planetary spin-axis/orbital history: *Icarus*, *198*, 305-317.

Fenton, L. K., Michaels, T. I., & Beyer, R. A., 2014. Inverse maximum gross bedform-normal transport 1: How to determine a dune-constructing wind using only imagery: *Icarus*, *230*, 5-14, doi:10.1016/j.icarus.2013.04.001.

Fenton, L. K., Michaels, T. I., Chojnacki, M., & Beyer, R. A., 2014. Inverse maximum gross bedform-normal transport 2: Application to a dune field in Ganges Chasma, Mars and comparison with HiRISE repeat imagery and MRAMS: *Icarus*, *230*, 47-63, doi:10.1016/j.icarus.2013.04.001.

Fernandez, R., Best, J., & López, F., 2006. Mean flow , turbulence structure, and bed form superimposition across the ripple-dune transition: *Water Resources Research*, *42*(5), doi:10.1029/2005WR004330.

Flahaut, J., Quantin, C., Clenet, H., Allemand, P., Mustard, J. F., & Thomas, P., 2012. Pristine Noachian crust and key geologic transitions in the lower walls of Valles Marineris: Insights into early igneous processes on Mars: *Icarus*, *221*, 420-435.

Forman, S. L., Oglesby, R., & Webb, R. S., 2001. Temporal and spatial patterns of Holocene dune activity on the Great Plains of North America: megadroughts and climate links: *Global and Planetary Change*, *29,* 1-29, doi:10.1016/S0921-8181(00)00092-8.

Freeman, A., Smrekar, S. E., Hensley, S., Wallace, M., Sotin, C., Darrach, M., Xaypraseuth, P., Helbert, J., & Mazarico, E., 2016. VERITAS: a Discovery-class Venus surface geology and geophysics mission (abstract): *2016 IEEE Aerospace Conference*.

Golombek, M. P., Banerdt, W. B., Tanaka, K. L., & Tralli, D. M., 1992. A prediction of Mars seismicity from surface faulting: *Science*, *258*, 979-981.

Golombek, M. P., & Phillips, R. J., 2010. Mars Tectonics: Chapter 5 in Planetary Tectonics, T. R. Watters and R. A. Schultz, eds., *Cambridge University Press*, 183-232.

Gómez-Elvira, J., et al., 2012. REMS: The Environmental Sensor Suite for the Mars Science Laboratory Rover: *Space Science Reviews*, *170*, 583-640, doi:10.1007/s11214-012-9921-1.

Goodman, R. E., 1980. Introduction to Rock Mechanics: *Wiley,* New York, 478 pp., 2nd ed.

Gourronc, M., et al., 2014. One million cubic kilometers of fossil ice in Valles Marineris: relicts of a 3.5 Gy old glacial landsystem along the Martian equator: *Geomorphology*, *204*, 235-255.

Greeley, R., White, B., Leach, R., Iversen, J., & Pollack, J., 1976. Mars: Wind Friction Speeds for Particle Movement. *Geophysical Research Letters*, *8*(3), 417-420.

Greeley, R., Leach, R., White, B., Iversen, J., & Pollack, J., 1980. Threshold Windspeed for Sand on Mars: Wind Tunnel Simulations. *Geophysical Research Letters*, *7*(2), 121-124.

Greeley, R., & Iversen, J. D., 1985. Wind as a Geological Process on Earth, Mars, Venus and Titan: *Cambridge University Press*, New York.

Grotzinger, J. P., et al., 2012. Mars Science Laboratory Mission and Science Investigation. *Space Science Reviews*, *170*(5), doi:10.1007/s11214-012-9892-2.

Grotzinger, J. P., et al., 2014. A Habitable Fluvio-Lacustrine Environment at Yellowknife Bay, Gale Crater, Mars: *Science*, *343*(616), 1242777.

Guzzetti, F., Cardinali, M., & Reichenbach, P., 1996. The Influence of Structural Setting and Lithology on Landslide Type and Pattern: *Environmental and Engineering Geoscience*, *2*(4), 531-555.

Harrison, K. P., & Grimm, R. E., 2003. Rheological constraints on Martian landslides: *Icarus*, *163*, 347-362.

Harrison, K. P., & Grimm, R. E., 2005. Groundwater-controlled valley networks and the decline of surface runoff on early Mars: *Journal of Geophysical Research Planets*, *110*, E12S16.

Harrison, K. P., & Chapman, M. G., 2008. Evidence for ponding and catastrophic floods in central Valles Marineris, Mars: *Icarus*, *198*, 351-364.

Hartmann, W. K., & Daubar, I. J., 2017. Martian cratering 11. Utilizing decameter scale crater populations to study Martian history: *Meteoritics & Planetary Science*, *52*(3), 493-510, doi:10.1111/maps.12807.

Hayward, R. K., Titus, T. N., Michaels, T. I., Fenton, L. K., Colaprete, A., & Christensen, P. R., 2009. Aeolian dunes as a ground truth for atmospheric modeling on Mars: *Journal of Geophysical Research-Planets*, *114*, doi:10.1029/2009JE003428.

Hayward, R. K., Fenton, L. K., & Titus, T. N., 2013. Mars Global Digital Dune Database ($MGD^3$): Global dune distribution and wind pattern observations. *Icarus*, *230*, 38-46.

Hayward, R. K., Fenton, L. K., & Titus, T. N., 2014. Mars Global Digital Dune Database ($MGD^3$): Global dune distribution and wind pattern observations: *Icarus*, *230*, 38-46, doi:10.1016/j.icarus.2013.04.011.

Hermanns, R. L., & Strecker, M. R., 1999. Structural and lithological controls on large Quaternary rock avalanches (sturzstroms) in arid northwestern Argentina: *GSA Bulletin*, *111*(6), 934-948.

Hersen, P., Andersen, K.H., Elbelrhiti, H., Andreotti, B., Claudin, P., Douady, S., 2004. Corridors of barchan dunes: stability and size selection: *Physical Review E*, *69*, 11304, doi:/10.1103 /PhysRevE.69.011304.

Hoek, E., & Bray, J. W., 1981. Rock slope engineering: *Institute of Mining and Metallurgy*, London, 358 pp., 3rd ed.

Houborg, R., & McCabe, M. F., 2018. A Cubesat enabled Spatio-Temporal Enhancement Method (CESTEM) utilizing Planet, Landsat and MODIS data: *Remote Sensing of Environment*, *209*, 211-226.

Hsü, K. J., 1975. Catastrophic debris streams (sturzstroms) generated by rockfalls: *GSA Bulletin*, *86*, 129-140.

Hsu, S-A., 1971. Wind stress criteria in eolian sand transport: *Journal of Geophysical Research*, *76*, 8684-8686.

Hsu, S-A., 1973, Computing eolian sand transport from shear velocity measurements: *Journal of Geology*, *81*, 739-743.

Hungr, O., 1987. An extension of Bishop's simplified method of slope stability analysis to three dimensions: *Géotechnique*, *37*(1), p. 113-117.

Hyvärinen, A. & Oja, E., 1997. A fast fixed-point algorithm for independent component analysis: *Neural Computation*, (7), 1483–1492.

Hyvärinen, A., 1999. Fast and robust fixed-point algorithms for independent component analysis. *IEEE Transactions on Neural Networks*, *10*(3), 626-634.

Ivanov, M. A., & Head, J. W., 2011. Global geological map of Venus: *Planetary and Space Science*, *59*(13), 1559-1600.

Iversen, J. D., & White, B. R., 1982. Saltation threshold on Earth, Mars and Venus. *Sedimentology*, *29*, 111-119.

Jackson, D. W. T., Bourke, M. C., Smyth, T. A. G., 2015. The dune effect on sand-transporting winds on Mars: *Nature Communications*, doi:10.0138/ncomms9796.

Jeandet, L., Steer, P., Lague, D., & Davy, P., 2019. Coulomb Mechanics and Relief Constraints Explain Landslide Size Distribution: *Geophysical Research Letters*, doi:10.1029/2019GL082351.

Johnson, B. C., & Campbell, C. S., 2017. Drop height and volume control the mobility of long-runout landslides on the Earth and Mars: *Geophysical Research Letters*, *44*(24).

Justus, C. G., Hargraves, W. R., Mikhail, A., Graber, D., 1978. Methods for Estimating Wind Speed Frequency Distributions: *Journal of Applied Meteorology and Climatology*, *17*(3), 350-353.

Katz, O., Morgan, J. K., Aharonov, E., & Dugan, B., 2014. Controls on the size and geometry of landslides: Insights from discrete element numerical simulations: *Geomorphology*, *220*, 104-113.

Kawamura, R., 1951. Study on Sand Movement by the Wind: *Reports of Physical Science Research Institute of Tokyo University*, *5*(3-4), 95-112, translated from Japanese by National Aeronautic and Space Administration (NASA), Washington, DC.

Keefer, D. K., 1984. Landslides caused by earthquakes: *GSA Bulletin*, *95*, 406-421.

Kerber, L., Head, J. W., Madeleine, J. B., Forget, F., & Wilson, L., 2011. The dispersal of pyroclasts from Apollinaris Patera, Mars: Implications for the origin of the Medusae Fossae Formation: *Icarus*, *216*(1), 212-220.

Kite, E. S., Lewis, K. W., Lamb, M. P., Newman, C. E., & Richardson, M. I., 2013. Growth and form of the mound in Gale Crater, Mars: Slope-wind enhanced erosion and transport: *Geology, 41*(5), 543-546, doi:10.1130/G33909.1.

Knapmeyer, M. E., Oberst, J., Hauber, E., Wählisch, M., Deuchler, C., & Wagner, R., 2006. Working models for spatial distribution and level of Mars' seismicity: *Journal of Geophysical Research: Planets*, *111*, doi:10.1029/2006JE002708.

Kok, J. F., 2010a. Difference in the wind speeds required for initiation versus continuation of sand transport on Mars: Implications for dunes and dust storms. *Physical Review Letters*, *104*(7), 074502.

Kok, J. F., 2010b. An improved parameterization of wind-blown sand flux on Mars that includes the effect of hysteresis. *Geophysical Research Letters*, *37*(L12202), doi:10.1029/2010GL043646.

Korup, O. Clague, J. J., Hermanns, R. L., Hewitt, K., Strom, A. L., & Weidinger, J. T., 2007. Giant landslides, topography, and erosion: *Earth and Planetary Science Letters*, *261*(3), 578-589.

Kositsky, A. P., and Avouac, J. P., 2010. Inverting geodetic time series with a principal component analysis-based inversion method: *Journal of Geophysical Research: Solid Earth*, *115*(B3), doi:10.1029/2009JB006535.

Lajeunesse, E., Quantin, C., Allemand, P., & Delacourt, C., 2006. New insights on the runout of large landslides in the Valles-Marineris canyons, Mars: *Geophysical Research Letters*, *33*(4), L04403.

Lapôtre , M. G. A., et al., 2016. Large wind ripples on Mars: A record of atmospheric evolution. *Science*, *353*(6294), 55-58.

Lapôtre , M. G. A., Lamb, M. P., & McElroy, B., 2017. What sets the size of current ripples? *Geology*, *45*(3), 243-246, doi:10.1130/G38598.1.

Lapôtre, M. G. A., Ewing, R. C., Weitz, C. M., Lewis, K. W., Lamb, M. P., Ehlmann, B. L., & Rubin, D. M., 2018. Morphologic Diversity of Martian Ripples: Implications for Large-Ripple Formation. *Geophysical Research Letters*, *45*, 10229-10239.

Lapôtre , M. G. A., Ewing, R. C., and Lamb, M. P., 2021. An Evolving Understanding of Enigmatic Large Ripples on Mars: *Journal of Geophysical Research: Planets*, doi:10.1029/2020JE006729.

Legros, F., 2002. The mobility of long-runout landslides: *Engineering Geology*, *63*, 301-331.

Leprince, S., Barbot, S., Ayoub, F.,& Avouac, J. P., 2007. *IEEE Transactions on Geoscience and Remote Sensing*, *45*(6), 1529-1558.

Leprince, S., Muse, P., & Avouac, J. P., 2008, In-flight CCD distortion calibration for pushbroom satellites based on subpixel correlation, *IEEE Transactions on Geoscience and Remote Sensing*, *46*(9), 2675-2683.

Lettau, K., & Lettau, H. H., 1978. Experimental and micrometeorological studies of dune migration: In *Exploring the World's Driest Climates*, Lettau, H. H., Lettau, K. (eds), *University of Wisconsin-Madison,* Madison, WI; 110-147.

Levy, J. S., Head, J. W., & Marchant, D. R., 2007. Lineated valley fill and lobate debris apron stratigraphy in Nilosyrtis Mensae, Mars: Evidence for phases of glacial modification of the dichotomy boundary: *Journal of Geophysical Research: Planets*, *112*, doi:10.1029/2006JE002852.

Liu, Z. Y., & Zimbelman, J. R., 2015. Recent near-surface wind directions inferred from mapping sand ripples on Martian dunes. *Icarus*, *261*, 169-181.

Lucchitta, B. K., 1978. A large landslide on Mars: *GSA Bulletin*, *89*, 1601-1609.

Lucchitta, B. K., 1979. Landslides in Valles Marineris, Mars: *Journal of Geophysical Research: Solid Earth*, *84*(B14), 8097-8113.

Lucchitta, B. K., 1987. Valles Marineris, Mars: Wet debris flows and ground ice. *Icarus*, *72*, 411-429.

Lucchitta, B. K., Isbell, N. K., & Howington-Kraus, A., 1994. Topography of Valles Marineris: Implications for erosional and structural history: *Journal of Geophysical Research: Planets*, *89*(E2), 3783-3798.

Malin, M. C., 1991. Mass Movements on Venus: Preliminary Results from Magellan Cycle 1 Observations: *Journal of Geophysical Research*, *97*(E10), 16337-16352.

Malin, M. C., et al., 2007. Context Camera Investigation on board the Mars Reconnaissance Orbiter: *Journal of Geophysical Research: Planets*, *112*, doi:10.1029/2006JE002808.

McCauley, J. F., et al., 1972. Preliminary Mariner 9 Report on the Geology of Mars. *Icarus*, *17*, 289-327.

McElroy, B., & Mohrig, D., 2009. Nature of deformation of sandy bed forms: *Journal of Geophysical Research: Earth Surface*, *114*(F3), doi:10.1029/2008JF001220.

McEwen, A. S., 1989. Mobility of large rock avalanches: Evidence from Valles Marineris, Mars: *Geology*, *17*, 1111-1114.

McEwen, A. S., et al., 2007. Mars Reconnaissance Orbiter's High Resolution Imaging Science Experiment (HiRISE). *Journal of Geophysical Research: Planets*, *112*(E05S02), doi:10.1029/2005JE002605.

Mège, D., & Bourgeois, O., 2010. Equatorial glaciations on Mars revealed by gravitational collapse of Valles Marineris wallslopes: *Earth and Planetary Science Letters*, *310*, 182-191.

Melosh, H. J., 1979. Acoustic fluidization: a new geologic process?: *Journal of Geophysical Research: Solid Earth*, *84*, 7513-7520.

Melosh, H. J., 1989. Impact cratering: A geologic process, *in* Research supported by NASA: New York, Oxford University Press, Oxford Monographs on Geology and Geophysics, No. 11, 253 p.

Merriam, R., 1960. Portuguese Bend Landslide, Palos Verdes Hills, California: *The Journal of Geology*, *68*(2).

Merrison, J. P., Gunnlaugsson, H. P., Nørnberg, P., Jensen, A. E., & Rasmussen, K. R., 2007. Determination of the wind induced detachment threshold for granular material on Mars using wind tunnel simulations. *Icarus*, *191*, 568-580.

Michel, S., Avouac, J. P., Ayoub, F., Ewing, R. C., Vriend, N., & Heggy, E., 2018. Comparing dune migration data measured from remote sensing with sand flux prediction based on weather data and model, a test case in Qatar: *Earth and Planetary Science Letters*, *497*, 12-21, doi:10.1016/j.epsl.2018.05.037.

Milliken, R. E., et al., 2008. Opaline silica in young deposits on Mars: *Geology*, *36*(11), 847-850.

Montgomery, D. R., Som, S. M., Jackson, M. P. A., Charlotte Schreiber, B., Gillespie, A. R., & Adams, J. B., 2009. Continental-scale salt tectonics on Mars and the origin of Valles Marineris and associated outflow channels: *GSA Bulletin*, *121*(1-2), 117-133.

Murchie, S. L., et al., 2009. A synthesis of Martian aqueous mineralogy after 1 Mars year

of observations from the Mars Reconnaissance Orbiter: *Journal of Geophysical Research: Planets*, *114*, doi:10.1029/2009JE003342.

Musiolik, G., Kruss, M., Demirci, T., Schrinski, B., Teiser, J., Daerden, F., Smith, M. D., Neary, L., & Wurm, G., 2018. Saltation under Martian Gravity and its Influence on the Global Dust Distribution: *Icarus*, *306*, 25-31, doi:10.1016/j.icarus.2018.01.007.

Necsoiu, M., Leprince, S., Hooper, D. M., Dinwiddie, C. L., McGinnis, R. N., & Walter, G. R., 2009, Monitoring migration rates of an active subarctic dune field using optical imagery: *Remote Sensing of Environment*, *113*, 2441-2447, doi:10.1016/j.rse.2009.07.004.

Nedell, S. S., Squyres, J. W., & Andersen, D. W., 1987. Origin and evolution of the layered deposits in the Valles Marineris, Mars: *Icarus*, *70*, 409-441.

Newman, C. E., et al., 2017. Winds measured by the Rover Environmental Monitoring Station (REMS) during the Mars Science Laboratory (MSL) rover's Bagnold Dunes Campaign and comparison with numerical modeling using MarsWRF: *Icarus*, *291*, 203-231, doi:10.1016/j.icarus.2016.12.016.

Newman, C. E., Kahanpää, Richardson, M. I., Martínez, G. M., Vicente-Retortillo, A., & Lemmon, M. T., 2019. MarsWRF Convective Vortex and Dust Devil Predictions for Gale Crater Over 3 Mars Years and Comparison With MSL-REMS Observations: *Journal of Geophusical Research: Planets*, doi:10.1029/2019JE006082.

Newman, C. E., et al., 2021. Multi-model Meteorological and Aeolian Predictions for Mars 2020 and the Jezero Crater Region: *Space Science Reviews*, *217*(20), doi:10.1007/s11214-020-00788-2.

Okubo, C. H., 2007. Strength and deformability of light-toned layered deposits observed by MER Opportunity: Eagle and Erebus craters, Mars: *Geophysical Research Letters*, *34*, L20205.

Ould Ahmedou, D., Ould Mahfoudh, A., Dupont, P., Ould El Moctar, A., Valance, A., & Rasmussen, K. R., 2007. Barchan dune mobility in Mauritania related to dune and interdune sand fluxes: *Journal of Geophysical Research*, *112*, doi:10.1029/2006JF000500

Owen, P. R., 1964. Saltation of uniform grains in air: *Journal of Fluid Mechanics*, *20*, 225-242.

Parteli, P. J. R., & Herrmann, H. J., 2007. Dune formation on the present Mars. *Physical Review E*, *76*(4), 041307.

Peulvast, J. P., & Masson, P. L., 1993. Erosion and tectonics in central Valles Marineris (Mars): a new morpho-structural model: *Earth, Moon, and Planets*: *61*, 91-217.

Phillips, M., 1980. A force balance model for particle entrainment into a fluid stream: *Journal of Physics D: Applied Physics*, *13*, 221-233.

Pike, R. J., 1971. Some preliminary interpretations of lunar mass-wasting process from Apollo 10 photography: *In* Analysis of Apollo 10 Photography and Visual Observations: NASA SP-232, Washington, DC, 14-20.

Pike, R. J., 1980. Control of crater morphology by gravity and target type: Mars, Earth, Moon: *Proceedings of the 11$^{th}$ Lunar and Planetary Science Conference*, 2159-2189.

Pla-García, J., et al., 2020. Meteorological Predictions for *Mars 2020 Perseverance Rover* Landing Site at Jezero Crater: *Space Science Reviews*, *216*, no. 148, doi:10.1007/s11214-020-00763-x.

Quantin, C., Allemand, P., Mangold, N., & Delacourt, C., 2004a. Ages of Valles Marineris (Mars) landslides and implications for canyon history: *Icarus*, *172*, 555-572.

Quantin, C., Allemand, P., & Delacourt, C., 2004b. Morphology and geometry of Valles Marineris landslides: *Planetary and Space Science*, *52*, 1011-1022.

Quantin, C., Flahaut, J., Clenet, H., Allemand, P., & Thomas, P., 2012. Composition and structures of the subsurface in the vicinity of Valles Marineris as revealed by central uplifts of impact craters: *Icarus*, *221*, 436-452.

Reid, M. E., Christian, S. B., Brien, D. L., & Henderson, S. T., 2015. Scoops3D – Software to Analyze Three-Dimensional Slope Stability Throughout a Digital Landscape: U. S. Geological Survey Techniques and Methods, book 14, ch. A1, 218 p., doi:10.3133/tm14A1.

Richardson, M. I., & Wilson, R. J., 2002. A topographically forced asymmetry in the martian circulation and climate: *Nature*, 416, 298-301, doi:10.1038/416298a.

Richardson, M. I., Toigo, A. D., & Newman, C. E., 2007. PlanetWRF: A general purpose, local to global numerical model for planetary atmospheric and climate dynamics: *Journal of Geophysical Research: Planets*, *112*(E09001), doi:10.1029/2006JE002825.

Roback, K. P., & Ehlmann B. L., 2020. *Martian Slope Stability Data*, version 1.0. CaltechDATA. doi:10.22002/D1.1617.

Roche, O., Attali, M., Mangeney, A., & Lucas, A., 2011. On the run-out distance of geophysical gravitational flows: Insight from fluidized granular collapse experiments: *Earth and Planetary Science Letters*, *311*(3-4), 375-385.

Runyon, K. D., Bridges, N. T., Ayoub, F., Newman, C. E., Quade, J. J., 2017a. An integrated model for dune morphology and sand fluxes on Mars. *Earth and Planetary Science Letters*. 457, 204-212, doi:10.1016/j.epsl.2016.09.054.

Runyon, K. D., Bridges, N. T., & Newman, C. E., 2017b. Martian sand sheet characterization and implications for formation: A case study. *Aeolian Research*, *29*, 1-11, doi:10.1016/j.aeolia.2017.09.001.

Sagan, C., et al., 1972. Variable features on Mars: Preliminary Mariner 9 television results. *Icarus*, *17*(2), 346-372.

Sakamoto-Arnold, C. M., 1988. Eolian features produced by the December 1977 windstorm Southern San Joaquin Valley, California: *Journal of Geology*, *89*, 129-137.

Sam, L., Gahlot, N., Prusty, B. G., 2015. Estimation of dune celerity and sand flux in part of West Rajasthan, Gadra area of the Thar Desert using temporal remote sensing data: *Arabian Journal of Geosciences*, *8*, 295-306, doi:10.1007/s12517-013-1219-4.

Scheidt, S. P., & Lancaster, N., 2013. The application of COSI-Corr to determine dune system dynamics in the southern Namib Desert using ASTER data: *Earth Surface Processes and Landforms*, *38*, 1004-1019, doi:10.1002/esp.3383.

Schenk, P. M., & Bulmer, M. H., 1998. Origin of Mountains on Io by Thrust Faulting and

Large-Scale Mass Movements: *Science*, *279*, 1514-1517.
Schultz, R. A., 2002. Stability of rock slopes in Valles Marineris, Mars: *Geophysical Research Letters*, *29*(19), 38-1 – 38-4.
Senthil Kumar, P., Krishna, N., Prasanna Lakshmi, K. J., Raghukanth, S. T. G., Dhabu, A., & Platz, T., 2019. Recent seismicity in Valles Marineris, Mars: Insights from young faults, landslides, boulder falls and possible mud volcanoes: *Earth and Planetary Science Letters*, *505*, 51-64.
Shaller, P. J., 1991. Analysis and Implications of Large Martian and Terrestrial Landslides: *PhD Thesis*, California Institute of Technology, Pasadena, CA, 586 p.
Sharma, S., 1994. XSTABL: An Integrated Slope Stability Analysis Program for Personal Computers, v. 5: *Interactive Software Designs, Inc.*, Moscow, Idaho.
Sherman, D. J., Li, B., Eliis, J. T., Farrell, E. J., Maia, L. P., Granja, H., 2013. Recalibrating aeolian sand transport models: *Earth Surface Processes and Landforms*, *38*, 169-178, doi:10.1002/esp.3310.
Silvestro, S., Fenton, L. K., Vaz, D. A., Bridges, N. T., & Ori, G. G., 2010. Ripple migration and dune activity on Mars: Evidence for dynamic wind processes. *Geophysical Research Letters*, *37*(L20203), doi:10.1029/2010GL044743.
Siminovich, A., Elperin, T., Katra, I., Kok, J. F., Sullivan, R., Silvestro, S., & Yizhaq, H., 2019. Numerical Study of Shear Stress Distribution Over Sand Ripples Under Terrestrial and Martian Conditions: *Journal of Geophysical Research: Planets*, doi:10.1029/2018JE005701.
Smith, A. B., Jackson, D. W. T., Cooper, J. A. G., 2017. Three-dimensional airflow and sediment transport patterns over barchan dunes: *Geomorphology*, *278*, 28-42, doi:10.1016/j.geomorph.2016.10.025.
Smith, J. D., 1970. Stability of a Sand Bed Subjected to a Shear Flow of Low Froude Number: *Journal of Geophysical Research*, *75*(30), 5928-5940, doi:10.1029/JC075i030p05928.
Smith, M. D., Pearl, J. C., Conrath, B. J., & Christensen, P. R., 2000. Mars Global Surveyor Thermal Emission Spectrometer (TES) observations of dust opacity. *Journal of Geophysical Research-Planets*, *105*(E4), 9539-9552.
Soukhovitskaya, V., & Manga, M., 2006. Martian landslides in Valles Marineris: wet or dry?: *Icarus*, *180*, 348-352.
Stark, C. P., & Hovius, N., 2001. The characterization of landslide size distributions: *Geophysical Research Letters*, *28*(6), 1091-1094.
Sullivan, R., et al., 2000. Results of the Imager for Mars Pathfinder windsock experiment: *Journal of Geophysical Research, 105*(E10).
Sullivan, R., et al., 2008. Wind-driven particle mobility on Mars: Insights from Mars Exploration Rover observations at “El Dorado” and surroundings at Gusev Crater: *Journal of Geophysical Research: Planets*, *113*(E06S07), doi:10.1029/2008JE003101.
Sullivan, R., & Kok, J. F., 2017. Aeolian saltation on Mars at low wind speeds: *Journal of Geophysical Research: Planets*, *122*(10), 2111-2143, doi:10.1002/2017JE005275.
Sullivan, R., Kok, J. F., Katra, I., and Yizhaq, H., 2020. A Broad Continuum of Impact

Ripple Morphologies on Mars is Enabled by Low Dynamic Wind Pressures: *Journal of Geophysical Research: Planets*, doi:10.1029/2020JE006485.

Swann, C., Sherman, D. J., & Ewing, R. C., 2020. Experimentally Derived Thresholds for Windblown Sand on Mars: *Geophysical Research Letters*, *47*, doi:10.1029/2019GL084484.

Tanaka, K. L., Robbins, S. J., Fortezzo, C. M., Skinner Jr, J. A., & Hare, T. M., 2014. The digital global geologic map of Mars: Chronostratigraphic ages, topographic and crater morphologic characteristics, and updated resurfacing history: *Planetary and Space Science*, *95*, 11-24.

Thomas, D. S. G., Knight, M., & Wiggs, G. F. S., 2005. Remobilization of southern African desert dune systems by twenty-first century global warming: *Nature*, *435*, doi:10.1038/nature03717.

Thomson, B. J., Bridges, N. T., Cohen, J., Hurowitz, J. A., Lennon, A., Paulsen, G., & Zacny, K., 2013. Estimating rock compressive strength from Rock Abrasion Tool (RAT) grinds: *Journal of Geophysical Research Planets*, *118*, 1233-1244.

Toigo, A., Lee, C., Newman, C. E., and Richardson, M. I., 2012. The impact of resolution on the dynamics of the martian global atmosphere: Varying resolution studies with the MarsWRF GCM: *Icarus*, *221*(1), 276-288, doi:10.1016/j.icarus.2012.07.020.

Türk, M., & Emeis, S., 2010. The dependence of offshore turbulence intensity on wind speed: *Journal of Wind Engineering and Industrial Aerodynamics*, *98,* 466-471.

Van der Hoven, I., 1957. Power Spectrum of Horizontal Wind Speed In the Frequency Range from 0.0007 to 900 Cycles per hour: *Journal of Meteorology*, *14*, 160-164.

Walker, I. J., 2002. Advances in research on dune-airflow-sand transport dynamics: incorporating secondary flow and sand transport processes: *in* Proceedings of ICAR5/GCTE-SEN Joint Conference, Lubbock, TX, USA, Publication 02-2, p. 458.

Watkins, J. A., Ehlmann, B. L., & Yin, A., 2015. Long-runout landslides and the lasting effects of early water activity on Mars: *Geology*, *43*(2), 107-110.

Watkins, J.A., Ehlmann, B.L., & Yin, A., 2020. Spatiotemporal evolution, mineralogical composition, and transport mechanisms of long-runout landslides in Valles Marineris, Mars: *Icarus*, *350*, 113836.

Weitz, C. M., Bishop, J. L., & Grant, J. A., 2013. Gypsum, opal, and fluvial channels within a trough of Noctis Labyrinthus, Mars: Implications for aqueous activity during the Late Hesperian to Amazonian: *Planetary and Space Science*, *87*, 130-145.

White, B. R., 1979. Soil transport by winds on Mars: *Journal of Geophysical Research: Solid Earth*, *84*(B9), 4643-4651.

Wilson, R. J. & Hamilton, K., 1996. Comprehensive Model Simulation of Thermal Tides in the Martian Atmosphere: *Journal of the Atmospheric Sciences*, *53*(9), 1290-1326, doi:10.1175/1520-0469(1996)053<1290:CMSOTT>2.0.CO;2.

Worman, S. L., Murray, A. B., Littlewood, R., Andreotti, B., & Claudin, P., 2013, Modeling emergent large-scale structures of barchan dune fields: *Geology*, *41*(10), 1059-1062, doi:10.1130/G34482.1.

Vermeesch, P., & Drake, N., 2008. Remotely sensed dune celerity and sand flux

measurements of the world's fastest barchans: *Geophysical Research Letters*, *35*(24), doi:10.1029/2008GL035921.

Vermeesch, P., Leprince, S., 2012, A 45-year time series of dune mobility indicating constant windiness over the central Sahara: *Geophysical Research Letters*, *39*, doi:10.1029/2012GL052592.

Viúdez-Moreiras, D., Gómez-Elvira, J., Newman, C. E., Navarro, S., Marin, M., Torres, J., de la Torre-Juárez, M., & the MSL team., 2019. Gale surface wind characterization based on the Mars Science Laboratory REMS dataset. Part II: Wind probability distributions: *Icarus*, *319*, 645-656, doi:10.1016/j.icarus.2018.10.010.

Yizhaq, H., Ashkenazy, Y., & Tsoar, H., 2009a, Sand dune dynamics and climate change: A modeling approach: *Journal of Geophysical Research*, *114*(F01023), doi:10.1029/2008JF001138.

Yizhaq, H., Isenberg, O., Wenkart, R., Tsoar, H., Karnieli, A., 2009b. Morphology and dynamics of aeolian mega-ripples in Nahal Kasuy, southern Israel: *Israel Journal of Earth Sciences*, *57*, 149-165, doi:10.1560/IJES.57.3-4.14